WIDEFIELD FLUORESCENCE CORRELATION SPECTROSCOPY

A Thesis
Presented to
The Academic Faculty

by

Philip R. Nicovich

In Partial Fulfillment
of the Requirements for the Degree
Doctor of Philosophy in the
School of Chemistry and Biochemistry

Georgia Institute of Technology
May 2010

WIDEFIELD FLUORESCENCE CORRELATION SPECTROSCOPY

Approved by:

Robert M. Dickson, Advisor
School of Chemistry and Biochemistry
Georgia Institute of Technology

L. Andrew Lyon
School of Chemistry and Biochemistry
Georgia Institute of Technology

Mostafa A. El-Sayed
School of Chemistry and Biochemistry
Georgia Institute of Technology

Mohan Srinivasarao
School of Polymer, Textile, and Fiber Engineering
Georgia Institute of Technology

Christoph Fahrni
School of Chemistry and Biochemistry
Georgia Institute of Technology

Date Approved: 4 March 2010

Dedicated to Mike Nicovich

ACKNOWLEDGEMENTS

The largest thanks for the work completed in this thesis belongs to my advisor, Prof. Robert Dickson. Finding a lab that has allowed my sometimes wandering research interests to lead my academic career has been an invaluable asset in my development as a scientist. Many thanks as well to the other members of the Dickson Lab past and present for their overly helpful assistance and shared expertise from the beginning.

I have received a great amount of help from other members of the Georgia Tech Chemistry community, especially Profs. Christoph Fahrni, Andrew Lyon, and Marcus Weck. To Ashley Ringer I am grateful for many hours of interesting discussions, scientific and otherwise.

I would like to thank my lovely wife, Sonya, for her continued support throughout my time in graduate school. My parents, Mike and Becky Nicovich, grandparents, Felix and Nettie Cirlot, and sister, Angie Pihera, have provided unending support without which my time at graduate school would have come to a premature end.

TABLE OF CONTENTS

LIST OF TABLES

LIST OF FIGURES

SUMMARY

The focus of this thesis the use of image series data as spatially-separated time series data. The utilization of correlation techniques to analyze this time series data yields important results regarding the systems in question. A large portion of this work relies on microfluidic devices as model systems for microscopic motion to develop the analysis methods presented.

Through the use of pixel-pair cross correlation mapping the flow in a three-dimensional volume in a microfluidic device was measured. When used in conjuction with a Nipkow disk confocal scanner this method allows for the rapid acquisition and analysis of flow speeds in an entire volume of interest within a microfluidic device. Simulations indicate that the correlation analysis technique is more tolerant to a high-noise environment than comparable particle tracking procedures, allowing data from images with S/N values as low as 1.4 to yield accurate flow maps with sufficient data length. This result indicates a compatability with smaller, dimmer fluorescent probes for flow mapping and to that effect fluorescently-labelled single antibodies have been used to map flow in a microfluidic channel. For results presented here flow speeds of hundreds of micrometers per second are presented but with appropriate experimental conditions flow speeds of tens of millimeters per second are compatable with this method.

Extending this technique to operate on multiple pixels surrounding a central origin allows for the fitting of a full flow vector from image series data. The correlation amplitude between a pair of pixels follows a $\sin^2$ dependence on the angle between the flow vector and spacing vector connecting the two pixels. By fitting an experimentally-determined correlation amplitude map for a subregion of the area of interest the

flow vector in that local area can be accurately determined. This method has been successfully applied to mapping flow around a partial obstruction and in the entrance of a microfluidic channel. Experimental and simulated data demonstrate that the full flow vector can be accurately computed for an arbitrary direction with speeds up to a few hundred micrometers per second.

The correlation amplitude maps have been utilized to determine the axial, out-of-plane flow angle as well. This axial-angle fitting method relies on the same Nipkow spinning disk confocal scanner and additional a piezo nosepiece capable of rapidly switching between multiple focal planes. As a result synchronous time-series data from multiple focal planes can be used to produce correlation amplitude maps that express both the planar and axial motion of flow. Single-plane techniques are able to only fit the in-plane projection of the three-dimensional flow vector while the method presented here allows for the axial contribution to be quantified as well. This method has been shown to accurately measure axial flow angles in simulated data as well as map the flow vectors in microfluidic devices showing large amounts of axial motion.

Spatially-separated time series data central to the flow mapping techniques can also be used to generate images in other experimental modalities. For optically-modulatable fluorophores, mapping the power of the modulation frequency yields a demodulated image with selective enhancement of the modulatable fluorophore over an obscuring constant background. A synthetic route to generate polystyrene beads labelled with Rose Bengal, a modulatable organic dye, for use as a modulatable probe is presented here. In additon, the use of higher-order statistics on time-series data of stochastic fluorophore blinking can be used to generate super-resolution images. This technique has been extended to demostrate its capacity for super-resolution images beyond relying on quantum dots and allowing imaging with emitters that blink on timescales faster than can be obtained with CCD-based acquisitions. As such, the use of higher-order statistical analysis on confocal image data utilizing the microsecond

blinking timescales of DNA:Ag nanoclusters to generate super-resolution images has been experimentally demonstrated.

In order to improve the quality of imaging there have been several novel noble-metal based fluorophores synthesized and characterized. Light-activated emissive silver nanoparticles templated with synthetic tyrosine-containing peptides have been presented. These particles are extremely bright and show enhanced Raman signals at the level of single diffusing particles. The use of tyrosine derivatives as reducing agents for silver clusters has been further investigated, resulting in several new fluorophores of sizes comparable to organic dyes. Finally, orange-emitting gold-glutathione particles of sizes less than 5 nm have been synthesized.

As microscopy techniques become more advanced, the subsequent techniques in data analysis and fluorescent probes must also continue to improve. Here has been presented novel methods for analyzing image stacks as a collection of spatially-distrubuted time series data in conjuction with correlations to yield a wide variety of results. These methods can be easily adapted to operate on a wide range of experimental systems, including live cells or whole organisms. With the increased used of such advanced image analysis techniques it is hoped that long-held secrets in microscopic phenomena can be revealed.

CHAPTER I

INTRODUCTION

1.1 Motivation

From the invention of the optical microscope, scientists have continued to steadily decrease the size of the objects they wish to observe [2, 3, 4]. Starting with multicellular organisms seen in pond water down through eukaryotic cells and bacteria towards the current interest in nanotechnology and even individual molecules, the frontier of the small has been pushed to the conceivable limits of what many can imagine. And as the observations focus on smaller and smaller things the necessary techniques to study such minute features become more and more difficult.

As a research tool, the optical microscope is both powerful and widely applicable for studying features smaller than the naked eye can detect. Optical microscopy is largely non-invasive and non-destructive, in comparison to electron microscopy or atomic force microscopy, and so is particularly suited for living or biological systems [5, 6, 7]. A multitude of techniques - staining, polarimetry, *etc.* - have been devised to deal with the many challenges assosicated with observing those things that naturally do not differentiate themselves from the background, but one of the most powerful of these is fluorescence microscopy.

Fluorescence microscopy relies on labelling the objects of interest with a substance, known as a dye, that fluoresces - that is, it will absorb and then subsequently re-emit a photon [8]. There are a large range of fluorescent dyes with different chemical and photophysical characteristics, allowing for specific and differentiable labelling of targets such as subcellular structures or microscopic devices. Very sensitive detectors in different architectures exist to measure down to single fluorescing molecules [9, 10,

11, 12, 13]. At the same time, the vast majority of the substances in nature do not fluoresce, allowing for an experiment with low background relative to the signal from the flourescent dye.

Historically the largest effort has been on using microscopy, fluorescence and otherwise, to study static objects. With advances in imaging and processing technology the focus has shifted towards using microscopy to measure dynamic processes [14, 15, 16, 17, 18]. Many interesting applications exist for determining dynamics on a microscopic scale such as vesicle trafficing in live cells [19, 20], or fluid motion in microfluidic devices [21, 22, 23, 24, 25, 26, 27]. In order to address the shortcomings in current methods new techniques must be developed.

This work focuses on the use of cross-correlation spectroscopy in a widefield configuration to rapidly measure various dynamic microscopic processes in a manner that is robust towards low signal strengths and is generally applicable to a wide range of systems. Here fluid motion in microfluidic devices is used as a model system to develop a method of determing flow profiles in both two and three dimensions. It is also shown that this method is easily adaptable to utilize dual laser fluorescence modulation for widefield signal extraction as well as exploiting the native fluorescence intermittancy of single molecules for imaging below the diffraction limit of light.

1.2 Fluorescence Spectroscopy

Fluorescence spectroscopy utilizes the ability of certain molecules and materials to absorb (excitation) and later emit (emission) a photon of light. Many materials of different types, including conjugated organic molecules [28, 29], metal clusters [30, 31], semiconductor quantum dots [7, 32], and fluorescent proteins [10, 33], collectively known as, 'fluorescent dyes,' or simply, 'dyes,' will undergo this process when exposed to near-UV through near-IR light, depending on the specific material.

Aside from the color of the light associated with the transition, the most important

parameter for experimental consideration is the brightness (B) of the dye, defined as the number of photons emitted per second under a given amount of excitation, and is a combination of three other parameters - excitation cross-section (ϵ), fluorescence quantum yield (Φ), and natural radiative lifetime (τ).

$$B = \frac{\epsilon * \Phi}{\tau} \tag{1}$$

Excitation cross-section describes the probability of a molecule absorbing an incident photon, in units of $M^{-1}cm^{-1}$. Once a photon is absorbed and a molecule is in the excited state, the fluorescence quantum yield describes the probability that an excited-state molecule will emit a photon, versus all other decay processes, while fluorescence lifetime describes the timescale of this process. Typical organic dyes have excitation cross-sections on the order of 50,000 to 200,000 $M^{-1}cm^{-1}$, fluorescence quantum yields of 0.1-0.9, and lifetimes on the order of 1-10 ns [29, 8, 28].

For a single-photon process the number of photons emitted depends linearly on the excitation intensity. The actual number of photons detected versus emitted in a given experimental configuration further depends on the collection efficiency of the experimental geometry, the transmission of any optics, including spectral filters, in the light path, as well as the quantum efficiency of the detector [34, 35].

While experiments on bulk materials do elucidate a large number of the photophysical properties of a material, on the microscopic scale the properties of single molecules become more and more important. While a bulk sample may give a constant emission intensity under constant excitation, a single molecule can experience fluorescence intermittancy, commonly referred to as 'blinking.' In this a molecule will typically give a constant emission intensity for a given amount of time, then no emission, only for the emission to return at some later time [10, 36, 30, 37]. In organic dyes this corresponds to an electron which typically radiatively decays from the singlet excited state to the singlet ground state, resulting in fluorescence, instead

goes through an intersystem crossing to a triplet state. The triplet state will decay nonradiatively back to the singlet excited state on a timescale much longer than the fluorescence lifetime [38, 39, 40]. Quantum dots experience a similar phenomenon, but is attributed to a charge separation in the electron-hole pair [41, 42, 43]. For organic molecules this process happens on the microsecond timescale while other materials such as semiconductor quantum dots have blinking dynamics on all experimental timescales. Generally the blinking is seen as a disadvantage as it decreases the overall emission intensity and the blinking dynamics can obscure other dynamic processes on similar timescales. However, there are techniques that rely on the native or experimentally-influenced blinking dynamics to extract or enhance the signal from intermittently-emitting fluorophores [44, 45].

In addition to blinking, fluorescent molecules under exciting illumination will experience photobleaching [46, 47, 48, 49]. For bulk signals this can be seen as an exponental decay in the emission over time but for single molecules this bleaching occurs in a single irreversable event. For organic dyes this bleaching event is often attributed to a highly-reactive triplet excited state which readily reacts with oxygen (which is in a triplet ground state), resulting in a non-fluorescent product [50]. Care can be taken to eliminate oxygen from solution to reduce photobleaching but typical organic dyes still only can remain emissive for tens of seconds or less before bleaching [51, 52, 39]. This largely limits the number of photons, and therefore information, that can be acquired from a single molecule.

Efforts to improve upon the photophysical characteristics of available fluorophores continue. A straight-forward way of improving the number of photons from a single particle is simply to tie a large number of particles together, often by prolifically labelling the surface of a functionalized polystyrene bead [53, 54]. This methodology does require that the experiment can tolerate fluorescent particles of much larger size - 100 nm or more in diameter versus 1 nm diameter of a single molecule. However,

for simply improving the brightness of the observed particles this method is widely useful, and in some applications the increased size is an advantage for limiting diffusive motion.

1.3 Correlation Spectroscopy

Initially developed by Magde and Elson in 1974, Fluorescence Correlation Spectroscopy (FCS) has proven to be a remarkably useful and widely applicable spectroscopic method in recent years [55, 56, 57, 58]. Thanks to advances in optics, detectors, and computer timing, processes operating on the microsecond timescale are easily detectable with single molecule sensitivity.

In the modern implementation of this technique, a excitation laser is tightly focused into a diffraction-limited spot with a Gaussian-bounded volume of tens of femtoliters or less. Emission from this spot is passed through a spatial filter (pinhole or small optical fiber) and continues along to a single-photon detector (avalanche photodiode (APD) or photomultiplier tube (PMT)) and then to a computer-controlled single photon counting module or correlator board. The resulting correlation curve generated from the data can then be used to determine physical parameters about the system.

Fluorescence Cross-Correlation Spectroscopy (FCCS) is performed in an analagous manner, but two or more focal spots are used instead of the single focal spot in FCS [59, 21, 22, 60]. This is often accomplished with the use of optics that separate the excitation beam into two spots based on their polarization, with a dual-core optical fiber, or simply using two simultaneous lasers. Detection is accomplished by splitting the emission signal onto two detectors. The two spots can be spatially or spectrally displaced (*i.e.*, two different wavelength lasers), the latter case proving particularly useful in co-localization and association studies. In this thesis, 'cross-correlation' will connotate correlation analysis of signals arising from different points in space.

Fluorescence correlation analysis can be used to investigate any process giving rise to a fluctuation in the detected fluorescence signal. Because of this generality, the technique has proven to be quite powerful and in recent years has been used to investigate a wide range of physical processes, including diffusion, flow, dark state processes, aggregation, and chemical isomerization.

Fluorescence correlation spectroscopy uses the fluctuations of the fluorescence signal at time t about the mean fluorescence intensity, given by

$$\delta F(t) = F(t) - < F > \tag{2}$$

where the brackets indicate an average over time [55, 56, 57, 58]. These fluctuations through time can be used to generate the correlation function

$$G(\tau) = \frac{< \delta I_a(t)\,(\delta I_b(t+\tau)) >}{< I_a >< I_b >} = \frac{< I_a(t)\,(I_b(t+\tau)) >}{< I_a >< I_b >} - 1 \tag{3}$$

in which $I_x(t)$ indicates the fluorescence intensity at time t at position x and $< I_x >$ is the mean intensity over time at position x. In the case that $a = b$, meaning that a single intensity *vs.* time trace is correlated against itself, this is known as the autocorrelation. The converse, $a \neq b$, indicates two distinct intensity *vs.* time traces and is known as the cross-correlation. These correlation curves can be expressed in terms of physical parameters (diffusion coefficient, triplet lifetime, flow time, *etc.*), depending on the exact system under investigation. Such equations will be discussed in relevant later chapters.

For autocorrelation curves, the function is at its highest at zero delay ($\tau = 0$), or where the signal is correlated with its exact copy. At infinite time the correlation is at the minimum asymptotic value, indicating two intensity traces that are uncorrelated at that offset. Between these two extremes the curve decays from the maximum to minimum at some offset, τ. It is this τ that is the timescale indicative of the process giving rise to the fluctuations. In additon, the amplitude of the fluctuation can, in

general, be related to the number of molecules undergoing that process at one time, averaged through the time of the measurement.

Similar parameters can be extracted from a cross-correlation as an autocorrelation, but with the added functionality from the spatial displacement of the two focal volumes. The only fluctuations that will give rise to a cross-correlation are those generated from the same event, meaning that between two intensity *vs.* time traces, only those events that give rise to signal in both channels will be correlated.

Many extensions of the typical FCS or FCCS technique have been reported, each to solve a particular issue with the fundamental method. The largest drawback of the single-point or even dual-point measurements provided by FCS and FCCS, respectively, is the limited spatial volume that is probed in a single experiment. In order to increase the number of locations investigated other groups have used scanning lasers [61, 62, 63], CCD detectors [64, 65], or pinhole arrays [66], or spinning disk confocal units [67]. It is this final method that this work improves upon to measure flow speeds in microfluidic devices.

1.4 Confocal Microscopy

Confocal microscopy has risen to the position of an indespensible tool for microbiology [68, 69]. In traditional widefield fluorescence microscopy the entire field of view is illuminated at one time and the subsequent emission is recorded on a CCD or other photodetector. This results in a large amount of signal coming from out-of-focus planes and a comparatively blurry image. In a confocal setup the excitation and emission light pass through apertures (pinholes) at focal planes conjugate to the sample. These pinholes reject light that comes from other focal planes above and below the area of interest and result in an increase in resolution in both the lateral, and particularly, axial directions. Resulting images are much clearer with greater contrast and less out-of-focus light obscuring fine features [69].

This technique lends itself well to imaging three-dimensional samples because of the natural ability to optically section the sample at different focal depths. This feature, combined with the noninvasive imaging method given by fluorescence microscopy, makes confocal microscopy particularly useful in imaging biological samples including live cells [69]. It follows that a confocal microscope is ubiquitous amongst institutions engaging in microbiological research.

While confocal microscopy is a powerful technique, there are some drawbacks. In addition to the universal limitations of optical and fluorescence microscopy there are other concerns with confocal microscopy. Because only a single point is imaged at any one time the focal point must be repositioned relative to the sample with either a scanning stage, or, more commonly in modern systems, programmable mirrors in the optical path. This serial data acquisition is more time-consuming than the parallel acquistion possible with multi-point detectors which limits the temporal resolution that can be achieved [70, 71, 72]. While the pinhole effectively constrains the amount of extraneous light, the amount of excitation and emission light transmitted through the small apertures constrict the amount of signal generated and results in longer acquisition times relative to widefield fluorescence microscopy [72].

The limitation of acquisition rates is particularly troublesome here where flow rates in microfluidic devices are to be measured. In order to overcome this problem a modification of the single-point confocal system has been developed. An apparatus containing a Nipkow spinning disk is utilized that rapidly acquires images across a wide area laterally but constrained axially [73, 74]. The Nipkow disk is an array of pinholes that when stationary act as parallel confocal volumes across a wide field of view. By rapidly rotating the disk with image acquisition times longer than the rotation period the pinholes trace out a confocal volume across the entire field of view. As a result confocal images for a single focal plane can be collected in a rapid fashon on a CCD detector, allowing for more temporal resolution than is typically

possible with a single-point confocal system [75, 71, 70]. The instrument utilized in this work is covered in more detail in section 2.5.

1.5 Measuring Microscopic Motion

Quantifying motion on a microscopic scale continues to be an important challenge. As devices and systems of interest decrease in size, such as the trend from microfluidics to so-called, 'nanofluidics,' the issues involved with performing measurements at such small length scales will often be compounded. When applied specifically to the measure of velocities in fluids the measurement is known as velocimetry, of which there exist many different techniques [76, 77, 78, 79]. In this thesis the focus will remain on optical techniques for measuring velocities in microscopic systems.

While it is, in fact, the motion of the fluid that is of interest, rarely is the motion of the fluid (often a common solvent, such as water) actually visible. In order to visualize the motion of the fluid, certain impurities are added that are visible. Continuing on the strengths of fluorescence microscopy, these impurities are often a small concentration of fluorescent dye or particles whose fluorescence can be imaged on a camera or other photodector [80]. These visible fluorescent impurities are commonly, interchangeably, and henceforth, known as, 'tracers', 'beads', and, 'particles'.

Of the fluorescence velocimetry methods, the most straightforward to understand is Particle Tracking Velocimetry (PTV) [81, 82]. In this technique, a particle is identified over the background in succesive frames of an image stack. Through one of many mathematical techniques the average displacement of the particles between the succesive frames can be determined and mapped as a function of position or time. Care must be taken to ensure that the same particles are identified in each frame which requires that the frame rates be rapid enough that the particles do not exit the region of interest in less than two frames. In addition the particles must be bright enough to distinguish from the background.

Many variations upon this theme exist, including Particle Image Velocimetry (PIV) [76, 78]. Here, instead of relying on the rapid acquisition of multiple frames, two exposures are taken in rapid succession, either through a fast camera or double-exposing an image with two laser pulses. By measuring the distance the tracers move over the double expsure, through autocorrelation or cross-correlation on the images, flow vectors can be determined. Excitation is typically accomplished through a planar sheet of laser radiation, limiting the flow measurements to a single focal plane. Additional dimensions require multiple cameras or illumination at multiple focal planes. Tracer particles must be very bright as to give sufficient signal in a brief exposure time, typically using large fluorescent beads hundreds of nanometers or larger in diameter.

While the above CCD-based systems can image a wide field of view in parallel, the requirements of the analysis and the low sensitivity of the detector put lower limits on the brightness, and therefore size, of the tracers that can be used. Conventional forms of FCS or FCCS can be used to measure flows, where transit of the tracers through the focal volume leads to the fluctuations that are later correlated [21, 22, 23, 24, 25, 26, 27]. These techniques allow for the use of smaller tracers, down to single fluorescent dye molecules, and are much more tolerant of noise and low signal strength than particle tracking methods. However, measuring the flow for an entire device requires repositioning the focal volume for every pixel in the resulting flow map.

An exstensive array of other methods exist utilizing fluorescence for measuring flow vectors. However, these methods require specialized setups and constraints on the types of systems that they will allow. A method that will work regardless of the sample architecture would be ideal such that any motion that can be captured in an image stack can be quantified.

1.6 Super-resolution Microscopy

While fluorescence microscopy continues to be a widely popular technique for investigating living cells, microscopic structures, and even whole multicellular organisms in three dimensions, the technique is limited by its inability to resolve structures smaller than the natural resolution limit. This limit, first described by Ernst Abbe in 1897, is known as the diffraction limit (d) [8]. The value for the diffraction limit is controlled by the wavelength of the light (λ) and the numerical aperture ($NA = 2n\,sin\,a$, where n and a indicate refractive index and half-angle of the maximum cone of light entering the lens, respectively) of the objective [8].

$$d = \frac{\lambda}{2n\,sin\,a} \tag{4}$$

$$d = \frac{\lambda}{2\,NA} \tag{5}$$

A wavelength of $\lambda \approx 550$ nm (green light) and a numerical aperature of $NA = 1.4$, this corresponds to a limit of $\approx$ 200 nm. Many interesting features exist below this wavelength so in order to study them it is beneficial to employ methods that generate images below the diffraction limit, or so-called super-resolution microscopy. As indicated in equation 4, an increase in the angle of the collection optics will result in a subsequent increase in resolution. This effect is very commonly utilized in fluorescence microscopy with the use of high NA microscope objectives, where the angle is on the order of 65 °.

Many methods have arisen in recent years to go beyond the diffraction limit in a widefield configuration [83, 84, 85, 86, 87]. The first of these optical techniques to be successful was near-field optical microscopy[88]. In this technique a very small aperture is positioned very close to the emitter. This distance is short enough (in the near-field zone) such that light does not diffract substantially, avoiding the need for

lenses and therefore the restrictions of the diffraction limit. This technique has been used to study membrane proteins but cannot be used for investigation beyond the surface of a structure [89, 90]. As such, this technique is severely limited in its use in intracellular investigations and all other techniques require the use of lenses in a far-field regime.

Confocal fluorescence microscopy has proven to be an indispensable technique in life sciences research for many years and offers a small increase in resolution [68]. By constraining the excitation and emission to a very small, point-like source the resulting resolution is increased by a factor of approximately $\sqrt{2}$ [86]. The inclusion of a pinhole also limits the influence of out-of-plane light and results in an increase in axial resolution over conventional widefield microscopy. A small pinhole offers the greatest increase in resolution but at the cost of light throughput. In addition, data at a single point is collected at one time, requiring a scanning apparatus to generate confocal images. Typical confocal systems can achieve lateral resolution of ≈ 150 nm and axial resolution of ≈ 500 nm for visible (green) light.

For samples including a large amount of structure in the axial direction the comparative lack of axial resolution with conventional microscopy techniques is a disadvantage. In 4Pi microscopy or I^5M microscopy, the resolution in the axial direction is increased by a factor of 3 to 5, down to ≈ 100 nm, but the lateral resolution remains unchanged [91, 92, 93]. These techniques both rely on the use of multiple objectives to collect a larger portion of angles surrounding an emitter before interferometrically recombining the signals into a single image. The resulting final image is one of higher axial resolution in either a point-scanning (4Pi) or widefield (I^5M) configuration.

Related to confocal microscopy, standing wave fluorescence microscopy (SWFM) and structured illumination microscopy (SI) utilize spatially-varied excitation to yield a final increase in spatial resolution [91]. To improve resolution in the axial direction SWFM relies on a pair of counter-propagating, non-focused laser beams for excitation.

These laser beams interfere, resulting in a standing wave in the excitation intensity that varies rapidly over the experimental distance in the axial direction. Images containing high-resolution information can be collected and combined to reconstruct a single super-resolution widefield image [94, 95, 96]. This technique is limited to very thin samples ($\leq$ 250 nm), but for this class the resolution is improved by a factor of ≈ 2 [97].

In a lateral adaptation of SWFM, structured illumination utilizes information in the spatial frequencies of fluorescence emission under structured excitation formed by interfering laser beams or by an interference grating. Reconstruction of several images yields a super-resolution with an increase in lateral and axial resolution of a factor of 2 [98]. This technique has been demostrated in 3-D to produce super-resolution reconstructions of biological samples [99, 100, 101]. Finally, with the addition of nonlinear saturated illumination, the theoretical framework for unlimited optical resolution has been demonstrated; the true resolution is limited by the signal-to-noise ratio of the acquisition, but PSF's of $\approx$ 50 nm have been demonstrated [102].

With careful analysis the fluorescence from a single fluorophore can be fit to a Gaussian function (in position *vs.* intensity) with the appropriate width. This fitting to the point-spread function results in a localization of a fluorophore within ten nanometers or less [103, 104, 105]. Such a method was utilized in the classic case of single-molecule spectroscopy in biophysics - determining the nature of motion in myosin [105]. For well-isolated fluorophores this process is straightforward, but fluorophores closer than the diffraction limit cannot be fit to a simple single Gaussian and the need to further resolve the positions of the fluorophores before localization becomes necessary [106]. This separation can be energetic - that is, two spectrally-distinct fluorophores can be imaged independently and later the positions mapped back to the original image space to determine positions within the original

diffraction-limited spot [107]. This separation can also be temporal, where independent stochastic events amongst the different emitters results in separation of their positions [106].

The simplest case of temporal separation is exploiting the single-step photobleaching behavior of single molecules. By fitting the Gaussian-approximated point-spread function (PSF) of a small collection of spatially unresolvable emitters before and after a photobleaching event the position of the bleached molecule can be localized [106]. A similar technique can be used in conjuction with long-lived dark states, such as those in semiconductor quantum dots, in place of photobleaching events [108]. In a widefield configuration a large number of emitters can be imaged and localized. These positions are later used to reconstruct a super-resolution image. However, there exists a trade-off between a well-labeled sample and the upper limit of the number of emitters that can be localized in a small area.

In order to curcumvent this issue, several methods developed simultaneously use a sample well-labelled with naturally dark fluorophores (photo-activated localization microscopy, PALM; stochastic optical reconstruction microscopy, STORM) [109, 110]. A brief flash of short-wavelength light will switch a small subset of the fluorophore population into the on state where they can be imaged until those fluorophores bleach. These fluorophores can then localized with high precision by fitting with a PSF; because only a small number of well-spaced fluorophores are on at a given time there is minimal overlap to complicate the fit. This process is repeated until the entire high-resolution image is constructed from the localalized fluorophore fits. This method does require the use of fluorophores that can be switched on with a flash of short-wavelength light and can take on the order of hours to reconstruct an image.

Most recently a method exploiting the natural blinking statistics of single fluorescent emitters to generate super-resoltion images has been reported from Shimon

Weiss and Jorg Enderlein [45]. This super-resolution optical fluctuation (SOFI) imaging uses the information contained in intensity *vs.* time traces at single pixel locations through an image stack in conjunction with higher-order statistics to reduce the width of the point-spread function by as much as a factor of 5. The individual emitters are separated by their stochastic blinking statistics rather than their distinct spectra or a single on/off event. This method is closely related to the flow imaging methods reported in this thesis and will be discussed in more detail in chapter 4.3, as well as an extension of this method to utilize the microsecond blinking dynamics of common fluorophores in a confocal geometry.

1.7 Noble Metal Fluorophores

The optical properties of noble metal clusters are unique due to the single unpaired valence electron in the neutral atom. Neutral noble metal atoms feature a full-filled d^{10} orbital with an additional s^1 electron. These outermost electrons are very weakly bound and are often considered delocalized and can move independently throughout the crystal lattice [111]. Displacement of these free electrons by an external electromagnetic field results in polarization changes at the surface of a metal with a linear restoring force [112]. Consequently the free electrons move throughout the crystal lattice under a constant potential field of the positively-charged cluster core.

Due to the Pauli exclusion principle the energy levels in these clusters are quantized and the energy of the electrons can be described by the classic particle-in-a-box. This model, which can be expressed as

$$E_n = \frac{n^2\, h^2}{8\, m\, L} \tag{6}$$

where E_n is the energy of quantized level n, m and h are the electron mass and Plank's constant, respectively, and L is the size of the metal. The energy levels increase with increasing number of electrons up to the maximum E_f, known as the

Fermi energy, which is independent of particle size. Spacing between energy levels is on the order of $E_f \backslash N$ for an N-atom cluster [113]. The Fermi energy also yields the Fermi wavelength, or the de Broglie's wavelength of an electron at the Fermi energy, for the metal of interest. For both silver and gold the Fermi energy is 5.5 eV, yielding a Fermi wavelength of around 0.5 nm [113].

Alkali metal clusters have similar electronic structures as the noble metals with a single unpaired valence s electron. When observing the mass spectra of sodium metal clusters, strong peaks at the mass corresponding to cluster sizes of N = 2, 8, 18, 20, 40, and 58 were noticed, indicating the relative stability of those 'magic number' clusters over other sizes [114]. Treating these electrons as free-moving and delocalized particles that form spherical electron shells around a positively-charged core allows these cluster sizes to be rationalized by the jellium model. Combined with the Pauli exclusion principle, the shells are treated as quantized and can be described by the 3D harmonic oscillator [114, 115]. The solutions to the spherical harmonic oscillator are very similar to those for a single atom but with a quadratic dependence on the radius of the potential. As a result the electronic shells and magic numbers represented in metal clusters is somewhat different (1s, 1p, 1d, 2s, ... corresponding to 2, 8, 18, 20 ... electrons) than is observed for single atoms (1s, 2s, 2p, 3s, 3d ... corresponding to 4, 10, 18 ... electrons) [116]. The observed magic numbers of sodium atoms can be explained by the fact that these cluster sizes yield full-filled electronic shells which are stable.

For the spherical harmonic oscillator the energy level spacing, ω, can be given in terms of the Wegner-Seitz radius, r_s, and the number of free electrons, n [117] as seen in equation 7

$$\hbar\,\omega = 3.61 \frac{\hbar^2}{2\,\mu\,r_s^2}\,n^{-1/3} \tag{7}$$

where $\hbar$ and μ are Plank's constant divided by 2π and the electron mass, respectively.

With metal clusters having constant electron density, the Fermi energies of these metals can be expressed as a function of the Wegner-Seitz radius alone as shown in equation 8 [114, 115].

$$E_f = \left(\frac{9\pi}{4}\right)^{2/3} \frac{\hbar^2}{2\mu\, r_s^2} \tag{8}$$

Combining equations 8 and 7 yields a simple relationship between energy level spacing ω, and therefore frequency, and the radius of the cluster, R.

$$\hbar\,\omega \approxeq E_f(N)^{-1/3} = E_f\, r_s\, R^{-1} \tag{9}$$

With this relationship it can be seen that an R^{-1} relationship between the energy level spacing of the particle and the particle size is expected. Studies on several single-valence electron atom clusters have shown this dependence, including ionization energies of Hg clusters [118], binding energies of Li clusters [119], and the photoionization energies of K clusters [120]. Most telling were experiments determining the optical spectra of Na_N^+ clusters, where $3 \leq N \leq 64$, at 105 K [121]. For the smallest clusters, up to $N = 9$, electronic transitions that were well separated could be observed. With increased cluster size these transitions began to overlap before giving way to a collective plasmon.

The observations made in other single-valence electron metal clusters has been observed in noble metals. Early work in this field involved isolating few-atom (2-8) silver clusters in the gas phase or in low-temperature rare-gas matrices [122, 123, 124, 125, 126]. These experiments showed discrete absorption bands through the near-UV and green. Emission in the UV through the red for silver dimer and trimer was observed for clusters isolated in Kr matrices with additional work showing discrete emission for tetrameric and octameric clusters in the same spectral region [127]. Similar work with gold has demonstrated discrete electronic transitions for isolated few atom clusters [125, 128, 129, 130]. Absorption transitions through the near-UV to

green with emission in the near-UV to red were observed.

The much higher stability of gold clusters versus sliver clusters has allowed their study in solution and at ambient temperatures to advance more quickly. Developments by Matthais Brust have allowed for the straightforward two-phase synthesis of organic-soluble small gold nanoparticles protected by alkane thiols [131]. Ligand exchange and etching can be used to change the solubility and sizes of these particles [132, 133, 134, 135, 136, 137, 138]. An enormous field of work exists concerning these larger nanoparticles, but smaller particles showing discrete electronic transitions have been made with other protecting ligands including Au_{55}, Au_{38}, Au_{28}, Au_{11}, and Au_3 [139, 140, 141, 142, 143]. With the use of PAMAM dendrimers (PAMAM = poly(amidoamine)) smaller clusters - Au_5, Au_8, Au_{13}, Au_{23}, and Au_{31} - have also been prepared [31].

The photophysical properties of these small gold clusters show a remarkable agreement the predicted values from the jellium model. The emission energy of the smallest particles (N = 1 to 13) agrees well with the expected dependence of $E_f/N^{1/3}$ [31]. The larger clusters (N = 23 to 38) deviate from this scaling but agree well with a model incorporating a Woods-Saxon potential rather than a spherical harmonic potential [144]. The Woods-Saxon potential is a consequence of the distortion due to the larger particle sizes and is an intermediate between the parabolic potential well of the spherical harmonic model and the square-well potential of larger particles. With the addition of an anharmonicity correction the larger particles can be brought well into agreement with the jellium model.

The photophysical properties agree well with the jellium model predictions but the abundance and stability of cluster sizes fail to conform to expected distributions. This disagreement is attributed to the influence of geometric stability and the close-packing of gold atoms in the clusters. In a particularly impressive work, the crystal structure of a thiol-protected Au_{25} cluster, $[N(C_8H_{17})_4][Au_{25}(SCH_2CH_2Ph)_{18}]$ was

reported. In this cluster a core gold atom is surrounded by 12 more gold atoms forming an icosahedron [145]. This Au_{13} core is protected by a shell of six units of the [-SR-Au-SR-Au-SR-] cyclic polymeric structure (-SR- = SCH_2CH_2Ph) with the gold atoms stellated on the faces of the core icosahedron. The structural stability of this cluster without the need of a magic number of atoms illustrates the importance of geometric arrangement of the metal atoms for cluster stability.

Extending the same success to silver clusters has proven a more difficult challenge. Silver clusters are much less stable in solution than their gold counterparts and require a scaffold to template cluster growth and protect the sliver clusters from aggregation [146, 147, 148, 30, 31, 149, 150]. The use of polyphosphate or polyacrylate allowed for the requisite sequestering of silver ions and reduction upon γ-ray exposure [148, 147, 146, 151, 152]. In these clusters discrete absorption was observed from multiple neutral and charged species that could be assigned to clusters of 2 to 4 atoms.

A great deal of work in the Dickson group at Georgia Tech as well as others has taken the silver fluorescence that has been observed first on surfaces and in mass-selected clusters into solution in order to more fully characterize and utilize the unique photophysical properties of these species [30, 153]. Continuation of these efforts have shown that PAMAM dendrimers are effective in protecting silver nanoclusters, leading to species with emission across the visible and near infrared [154, 153]. Continued work to improve the biocompatability of these probes led to the use of oligonucleotides and peptides as cluster scaffolds [149, 155, 156, 157, 158, 159, 160, 161, 162].

The greatest success of with water-soluble silver cluster fluorophores has come with the use of single-stranded DNA as a templating and support agent for the silver cluster [31, 149, 155, 156, 158, 163, 160]. It has been found that the specific base sequence of the DNA strand has a strong influence on the size, and therefore specific photophysical properties, of the silver cluster. A range of fluorophores have been created with extremely photostable emission across the visible and near infrared.

These fluorophores feature very high quantum yields, large extinction coefficients, and nanosecond lifetimes, yielding very bright emission on the single molecule level. The fluorescence intermittancy due from these sliver clusters, assigned to a charge-transfer process between the silver cluster and the DNA backbone [164], has proven useful in the ability to control the timescale of this intermittancy secondary near-IR irradiation [165]. This control of the dark-state dynamics allows for significant fluorescence enhancement and modulation.

1.8 Fluorescence Modulation

Under increasing excitation intensities the fluorescence output of a fluorophore will increase linearly before reaching a saturation limit. For most fluorophores this limit is due to the depletion of the ground state fluorophore population and is typically not a consequence of saturating the transition into the excited singlet state. Rather, this depletion is due to intersystem crossing (ISC) to a triplet state [44, 166]. Intersystem crossing happens with a constant probability for every excitation, so with increased excitation intensities the fraction of molecules in the triplet state increases, leading to the depletion of the ground state.

This triplet state will naturally decay back to the singlet ground state through reverse intersystem crossing (RISC), but at a timescale of microseconds to milliseconds versus a timescale of nanoseconds for the decay to the singlet ground state from the singlet excited state. While in the triplet state the fluorophore is non-emissive and therefore the triplet state population constrains the maximum amount of fluorescence that can be realized from a fluorophore. In addition the triplet state is more reactive than the ground state and therefore more succeptable to destructive photobleaching reactions [52, 167]. Other possible phenomena give rise to fluorescence dark states in addition to intersystem crossing, including isomerization and electron transfer [168, 40].

While in a transient dark state it is still possible for a molecule to absorb an additional photon [169, 170]. This so-called transient absorption is characteristic of the distinct electronic environments of the excited and ground state [171, 172]. Just as with an excited singlet leading to intersystem crossing, there is a finite probability of an excited state triplet undergoing reverse intersystem crossing and returning to the singlet (emissive) manifold [173, 174, 175]. In systems where the dark state is due to other phenomena, a photon absorbed in the dark state can lead to isomerization or other processes that return the molecule to the emissive state [164, 165, 176, 177, 178, 179].

Of particular utility is when the absorption leading to dark-to-emissive state system crossing is of a different wavelength than the singlet excitation. In such a case secondary illumination can be used to restore emission from a molecule in a long-lived dark state trap. This scheme has been used for sequential single-molecule localization (PALM and STORM, mentioned above) and for optical lock-in detection [180, 181, 182, 183]. However, in both of these cases the secondary illumination is of higher energy than the fluorescence, giving rise to extra background in the fluorescence signal.

With longer-wavelength secondary illumination it is possible to depopulate the triplet dark state of some organic molecules, as well as DNA:Ag silver nanoclusters, leading to an enhancement in overall fluorescence brightness [165, 164, 184, 174, 44]. For most efficient fluorescence emitters this enhancement process is weak in solution due to the low dark-state population to be depopulated with the secondary laser and requires high laser powers ($\approx$ MW/cm^2) [44]. However, for organic molecules showing significant triplet quantum yields, enhancements of up to 5-fold with appropriate dual-laser excitation can be achieved in solution [184]. Particularly well-suited for this process are DNA:Ag clusters, which can show several-fold enhancement with secondary laser powers on the order of kW/cm^2 [165].

This fluorescence enhancement through dark state depletion operates on a rapid (sub-microsecond) timescale and is proportional to the intensity of the secondary laser. In concert these two features mean that the secondary illumination can be used to encode the resulting fluorescence signal with an input waveform. The waveform will be reflected only in the fluorescence of those molecules that are modulatable at the wavelengths used and not in those that only emit under the same primary excitation. By demodulating the fluorescence signal at the frequency used for modulation of the secondary illumination those fluorophores of interest can be extracted from a signal of high background [165, 184].

1.9 Organization of thesis

This thesis is organized in 6 chapters, including this introduction and final conclusions. The intervening chapters will introduce the experimental methods used in this work, cross-correlation flow imaging, the adaptation of this method for modulation extraction and super-resolution imaging, and details of the synthesis and properties of novel noble metal fluorophores.

Work appearing in this thesis has been published elsewhere in the following articles:

- P. R. Nicovich, P. Sood, J.-C. Hsiang and R. M. Dickson. "Confocal SOFI for Super-Resolution Imaging with Fluorophores Showing Biocompatable Blinking Dynamics." 2010, in preparation.

- P. R. Nicovich, R. M. Dickson. "Out-of-plane Flow Mapping with Widefield Cross-correlation Microscopy." 2010, in preparation.

- P. R. Nicovich, R. M. Dickson. "Three-dimensional Flow Mapping in Microfluidic Channels with Widefield Cross-correlation Microscopy." *Israel Journal of Chemistry*, 2010, accepted.

- J. Zheng, P. R. Nicovich, and R. M. Dickson. "Highly Fluorescent Noble-Metal Quantum Dots." *Annual Reviews of Physical Chemistry.* 2007, 58, 409-431.

CHAPTER II

EXPERIMENTAL OVERVIEW

2.1 Bulk Photophysical Methods

Measurements of ensemble photophysics were utilized to quantify fluorescence and absorbance spectra as well as fluorescence lifetimes. Bulk fluorescence measurements were performed on a Photon Technology International (PTI) Quanta Master 40 fluorimeter which was equipped with a photomultiplier tube (PMT) detector and xenon arc lamp light source. Excitation and emission spectra were collected using FeliX32 software (PTI) which controlled the two monochromators. Absorbance spectra were collected on a Shimadzu UV-2410 PC spectrophotometer. In all samples glass or quartz cuvettes were used.

Fluorescence lifetimes were measured on a Edinburgh Instruments Lifespec-ps system with a Hammamatsu microchannel plate photomultiplier tube (MCP-PMT) and Picoquant diode lasers of appropriate wavelength as the excitation source. Fitting and further analysis of the spectra was performed with the instrument software or in custom-written MATLAB scripts.

2.2 Fluorescence Microscopy

Fluorescence microscopy experiments were performed on Olympus IX-70 or IX-71 inverted microscopes. Save for the spinning-disk confocal experiments the excitation light, provided by a laser or mercury lamp, was directed through the rear port of the microscope. The excitation was reflected up through the objective and to the sample by a dichroic mirror of appropriate transmission spectra so to reflect the excitation radiation but transmit the subsequent emission wavelengths. Emission was further

spectrally filtered through an emission filter, typically a long-pass or band-pass filter transmitting emission but not excitation wavelengths, before continuing on to a CCD, APD, or PMT detector. In most cases the excitation light was also passed through a band-pass filter before reaching the back aperture of the microscope to ensure that no extraneous wavelengths continued through the experimental apparatus.

Microscope objectives used in this work were either oil immersion (100x, 1.40 NA; 60x, 1.45 NA) or, more commonly, water immersion (60x, 1.2 NA). When precise control of the objective position was needed a piezo nosepiece (PI P-720) controlled by a benchtop DC power supply was used. Throughout all experiments samples were mounted on 22.5x22.5 mm glass coverslips (Fisher) of 0.15 mm thickness.

2.3 Time-Correlated Single Photon Counting

Time-correlated single photon counting (TCSPC) is a method by which the arrival times of individual photons are recorded with very high temporal resolution (picosecond or faster). In this method the photons are directed, upon exiting the microscope, to a high-sensitivity photodetector (avalanche photdiode (APD) or photomultiplier tube (PMT)), typically *via* an optical fiber. The photodetector transforms the incident photon into an electrical pulse, which triggers a photon counting module (Becker-Hickl SP630 or Time Harp).

Photon arrival times are divided into two distinct values which are measured separately. The macrotime of the photon arrival is measured from the beginning of the experiment with lower temporal resolution [185]. The microtime is measured with the use of a time-to-amplitude converter (TAC). The TAC is triggered by an incident pulse (the 'start' pulse) from the photodetector corresponding to the arrival of a single photon. Concurrently an external pulse train is supplied to the TCSPC module from an arbitrary function generator. These external sync pulses are known as 'stop' pulses. Upon arrival of a start pulse the TAC produces an analog pulse

whose amplitude is precisely tied to the time between the arrival of the start pulse and the next stop pulse. An anolog-to-digital converter transforms the amplitude of the analog TAC pulse to a digital signal corresponding to the time the photon arrived at between subsequent stop pulses. This more precise time signal is known as the microtime.

The microtime and macrotime data yield different information at their distinct experimental timescales. The macrotime resolution is on the order of hundreds of nanoseconds to microseconds up to seconds or longer. The microtime time resolution at the upper end is limited by the sync pulse train - often 100 ns. At the low end the microtime is measured with resolution of tens of picoseconds.

2.4 Super-Resolution Confocal Microscopy

Confocal microscopy experiments were performed on a homebuilt confocal system based around an Olympus IX-70 inverted microscope. A schematic appears in figure 2.3. To the pictured scheme a scanning stage was added to allow for confocal images to be built from single-point data. Excitation was provided by the 632.8 nm line from a HeNe laser that was passed through a 640/10X excitation filter, then a beam expander to generate a spot to overfill the back aperture of a 100x oil-immersion objective (Olympus, 1.40 NA) after reflecting off of a 670 nm long-pass dichroic mirror. Fluorescence from the emitter passed through the same objective and dichroic mirror, through a 710/40X band-pass emission filter and a 1.5x magnification lens, and then exited the side port of the microscope. A 50 μm optical fiber was aligned at the side port. The fiber was both acting as a pinhole and transmitting light to an APD.

The scanning stage was controlled by custom-written software (Microscoft Visual C++) which also acted as the acquisition software for a TCSPC module (Becker-Hickl). Data was collected serially at individual points to cover the area of interest. At each point a dwell time of 250 ms or 500 ms was used. For experiments presented,

an area of 1 μm x 1 μm was covered with 25 nm steps.

The emitter chosen was a DNA:Ag complex with excitation and emission maxima at 630 nm and 700 nm, respectively. This complex was synthesized by combining single-stranded DNA (5'- CCC TAA CTC CCC - 3') with silver nitrate ($AgNO_3$) and sodium borohydride (NaBH4) in a 1:6:3 ratio in aqueous solution. These solutions were spin cast 5% PVA (poly(vinyl alcohol)) with 2-, 10-, or 100-fold dilutions onto standard glass coverslips and imaged.

2.5 Spinning Disk Confocal Microscopy

A modification of typical confocal microscopy involves the use of a spinning disk with a large number of pinholes which trace out an image of the entire focal plane but reject the out-of-plane light. When static the pinhole array generates many spatially-constrained detection volumes in parallel [66]. By rotating the pinhole array at a rate much faster than the image acquisition the multiple pinholes trace out a path covering the entire field of view evenly, resulting in a widefield confocal image.

In the experiments appearing in this work this was achieved with a Yokogawa Confocal Scanning Unit 10 (CSU 10). This particular unit improves light throughput through a second disk with microlenses aligned with the pinhole array, focusing a larger amount of the excitation through the pinhole array [73].

Excitation light was aligned into a single-mode optical fiber which passed through the CSU, through the microscope side port, and onto the sample. Emission passed through the same side port, through the same pinholes, and then was diverted by a dichroic mirror through an emission filter before detection on a CCD. A diagram of the Yokogawa CSU 10 appears in figure 2.2 and a schematic for the experimental setup in figure 2.1.

The pinhole array traces out 12 images per rotation and rotates at 30 Hz. The frame rate of the camera must be synchronized to the 360 images per second to ensure

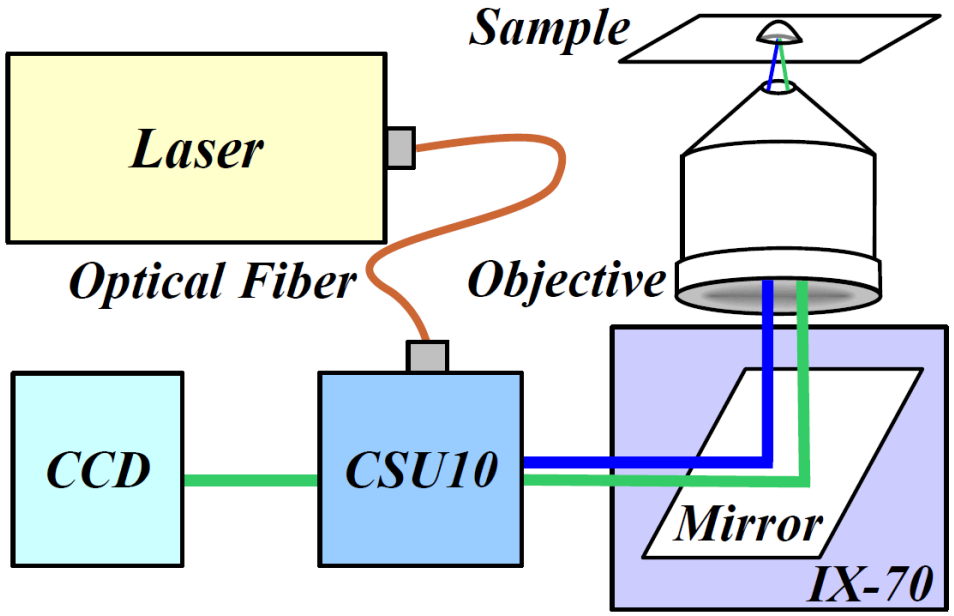

Figure 2.1: Schematic of the experimental setup for spinning disk confocal microscopy. Emission and excitation are shown as single side-by-side beams for clarity but would be colinear and multiple in experiment. Excitation light is indicated in blue and emission in green. Yokogawa Confocal Scanning Unit - CSU10; Olympus inverted microscope - IX-70; Andor iXon EMCCD camera - CCD

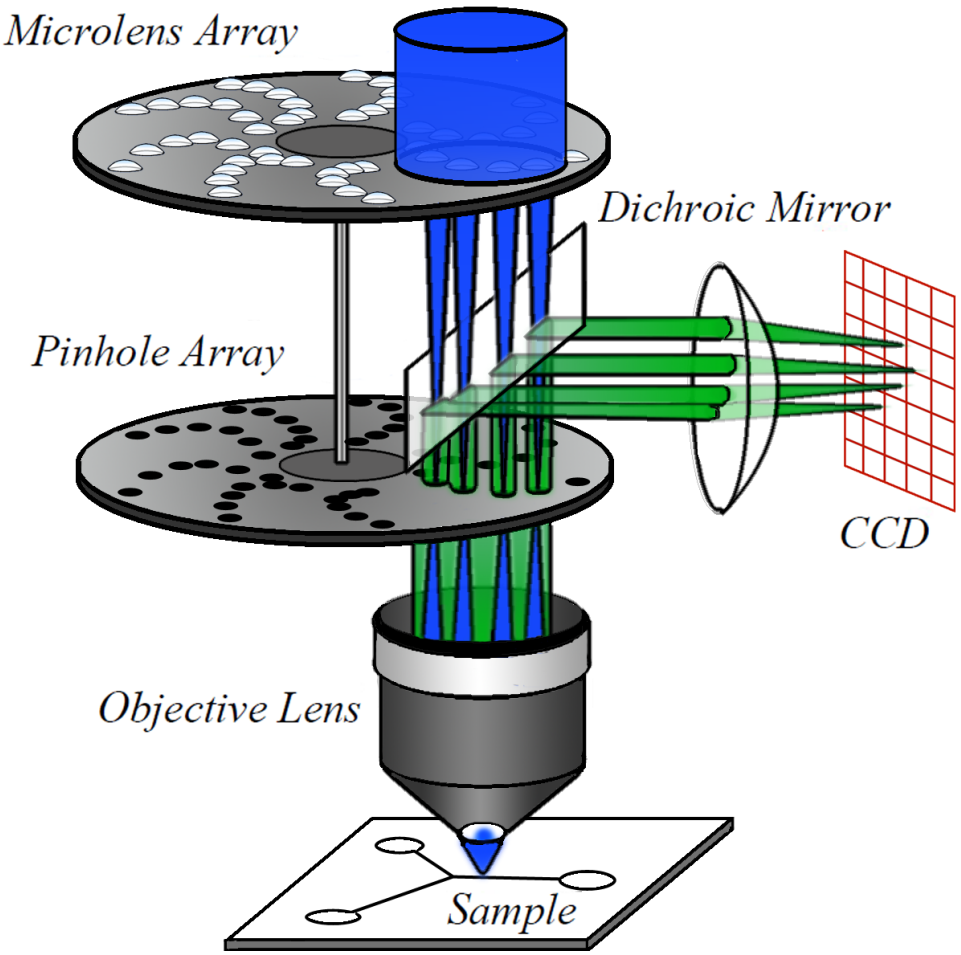

Figure 2.2: Schematic of Yokogawa Confocal Scanner CSU 10. Excitation light is indicated in blue and emission in green.

that even illumination across the field of view reaches the detector. The frame rates chosen were those that satasfied this condition and allowed for sufficient exposure time with minimal blurring.

2.6 Fluorescence Correlation Spectroscopy

Fluorescence Correlation Spectroscopy (FCS) is a powerful technique to measure many photophysical processes giving rise to fluctuations in the intensity *vs.* time signal. The fundamental technique in this field utilizes a single diffraction-limited focal spot and is useful in measuring diffusion constants, hydrodynamic radii, concentration, and blinking dynamics. In the experimental setup (Figure 2.3) a laser is focused through a microscope objective into a diffraction-limited spot, typically 1-15 femtoliters in volume, in the sample solution. Emission from fluorophores inside the focal volume passes through the same objective, then through the microscope optics and spectral filters, before exiting the microscope. Fluorescence signal continues through an optical fiber (50 μm or 100 μm core) acting as a pinhole before reaching an APD. Signals from the APD are recorded with a TCSPC module and later analyzed.

While any signal that yields fluorescence fluctuations can be analyzed through fluorescence correlation spectroscopy, the properties of interest in this work are the diffusion and blinking timescales. A more detailed derivation of the relevent equations appears in Appendix A. For independently-diffusing emitters in a Gaussian-approximated focal volume, the autocorrelation is

$$G(\tau) = \frac{1}{N}\left[1 + \frac{\tau}{\tau_D}\right]^{-1}\left[1 + \frac{\tau}{\omega_o^2\,\tau_D}\right]^{-\frac{1}{2}} \tag{10}$$

where N, τ_D, and ω_o correspond to the number of molecules in the focal volume, the diffusion time (seconds), and the aspect ratio of the focal volume, respectively. The aspect ratio is defined as $\omega_o = \frac{\omega_z}{\omega_{xy}}$, where ω_z and ω_{xy} are the e^2 radii (m) of the Gaussian focal volume in the axial and lateral directions, respectively. The

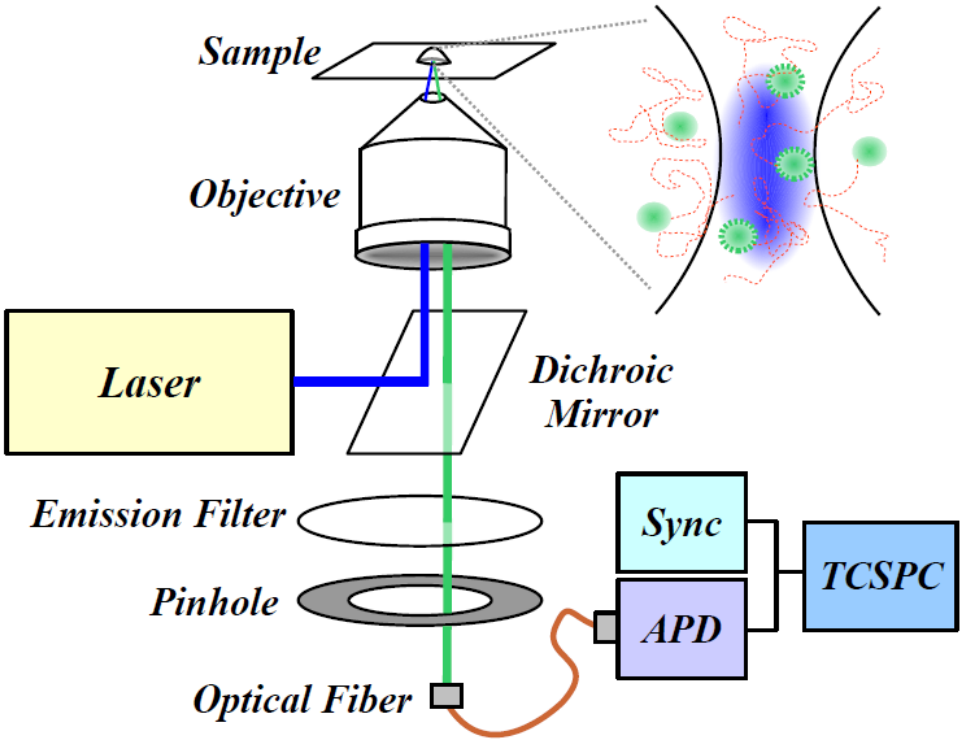

Figure 2.3: Schematic of a typical FCS experiment. Excitation is shown in blue and emission and fluorophores in green. Emission and excitation are shown as single side-by-side beams for clarity but would be colinear and multiple in experiment. Confocal experiments were performed on an identical setup with the addition of a scanning stage. Avalanche photodiode - APD; External sync source - Sync; Time-correlated single-photon counting module - TCSPC

three variables can be fit to an experimental autocorrelation (generated in BIFL or MATLAB). The value for N can be transformed into concentration, C, by

$$C = \frac{N}{V_{eff}} \tag{11}$$

where V_{eff}, the effective volume (m^3), is defined as

$$V_{eff} = \pi^{\frac{3}{2}} \omega_{xy}^2 \omega_z \tag{12}$$

The value for τ_D can be used to determine the diffusion constant, D ($m^2 sec^{-1}$), by

$$D = \frac{\omega_{xy}^2}{4 \tau_D} \tag{13}$$

and then onward to the hydration radius, R_h, (m), through the Stokes-Einstein equation

$$R_h = \frac{k_B T}{6 \pi \eta D} \tag{14}$$

where k_B is the Boltzmann constant ($1.3806503 * 10^{-23} m^2 kg s^{-2} K^{-1}$), T the temperature in Kelvin, and η the viscosity of the solvent ($8.94 * 10^{-4} N m^{-2} s$ for water at 298 K).

It is necessary to define the size of the focal volume in terms of some external property, either concentration or a known diffusion constant. The concentration for a sample of pure dye is straightforward to determine if the absorption cross-section is known. Running a range of known dilutions and using the experimentally-determined value for N at those concentrations generates a linear plot, which, when extrapolated to zero dilution, returns the number of dye molecules per focal volume for the original dye solution. From this information and equations 11 and 12 the dimensions of the focal volume can be determined. Alternatively if the diffusion constant is known the focal volume size can be calculated using the experimental diffusion time τ_D and

equation 13. In practice using the diffusion constant to determine focal volume is more consistient than through concentrations. For a typical xanthene derivative organic dye (Rhodamine, Alexa 488...) the diffusion constant is around 2 x 10^{-10} m^2 sec^{-1} [1].

After calibration of the focal volume with a dye standard the same setup can be used to determine values of concentration, diffusion constant, and hydration radius of an unknown fluorophore. Therein lies the power of FCS for these measurements - the sample does not need to be chemically pure, only soluble and emissive, to determine values such as size and extinction coefficient.

The strongest fluctuations are observed when only a few molecules, on average, are in the focal volume (see $\frac{1}{N}$ dependence in equation 10), requiring extremely dilute solutions (nM to pM) of fluorophore. Experiments were performed with the focal volume far enough away from the coverslip (approximately 30 μm) to avoid artifacts in the molecular diffusion. Because of the need for a long working distance between the focal volume and the objective a water immersion objective (Olympus, 60x, 1.2 NA) was used for all diffusion FCS experiments.

Static molecules that undergo fluorescence intermittancy (blinking) will also give rise to an autocorrelation signal. For most fluorophores (*i.e.* not quantum dots) these processes are exponential in nature and can therefore be fit to a single exponential function

$$G(\tau) = F\, exp\left(\frac{\tau}{\tau_F}\right) + 1 \tag{15}$$

where F and τ_F are the fraction of blinking emitters and the fluctuation timescale, respectively.

2.7 Microfluidics

Microfluidic channels were molded in poly(dimethysiloxane) (PDMS) and sealed on a glass coverslip. Flow was achieved through custom plumbing in a gravity-fed or

pressure-driven flow. Continuous pressure was supplied by a syringe pump delivering solution from a 50 μL glass syringe. Straight channels were 50 μm by 50 μm in cross-section in a simple Y-channel setup with one inlet and two outlets. Three-dimensional flow was achieved by introducing obstructions into a straight channel or with a microfluidic channel designed to generate flow vortices.

All microfluidic channels were obtained from a generous gift from Grant Hendrickson and Andrew Lyon.

2.8 Dual-laser experiments

Fluorescence modulation was achieved by introducing a secondary, longer wavelength laser into the same focal volume as the primary excitation. For single-point FCS experiments the two laser beams were combined with a dichroic mirror outside the microscope before the beams entered the rear port (see figure 2.4). For dual-laser excitation in conjunction with the spinning disk system, the primary excitation was intruduced through the side port of the microscope while the secondary excitation was routed through the back (see figure 2.5). In both cases careful choice of the dichroic mirror in the microscope turret was vital.

The modulation signal was introduced to the secondary laser through a mechanical chopper or shutter for low-frequency signals (up to 60 Hz). High frequency signals were introduced by routing the secondary illumination through an acousto-optic modulator controlled by an arbitray function generator. With such a setup several kHz signals are possible. Secondary lasers in all experiments were a Ti:Sapphire (Coherent) operating in CW mode or a diode laser, both operating at 805 nm.

2.9 Data Analysis

Data analysis was performed primarily with custom-written scripts in MATLAB. When warranted some data was analyzed with BIFL (Becker-Hickl) or Origin. The use of MATLAB scripts allowed the large number of available built-in functions to

be exploited, greatly streamlining the development of the analysis procedures. Image data was exported as ASCII data in the Andor Solis acquisition software for further analysis. Spectra were recorded as ASCII files for later analysis. Data from TCSCP experiments were utilized in the native file format for the Becker-Hickl board.

The large amount of image data that needed to be processed required careful management of memory through the analysis. This was accomplished originally by declaring each frame of image data as a cell in a cell array which allows for the image stack to be stored in non-contiguous memory. However addressing portions of this data is slow so subsequent analysis was accomplished by first converting the exported Andor ASCII files to a binary file. The necessary portions of this binary file could be read much more rapidly, increasing the speed of the analysis by several fold over the previous method.

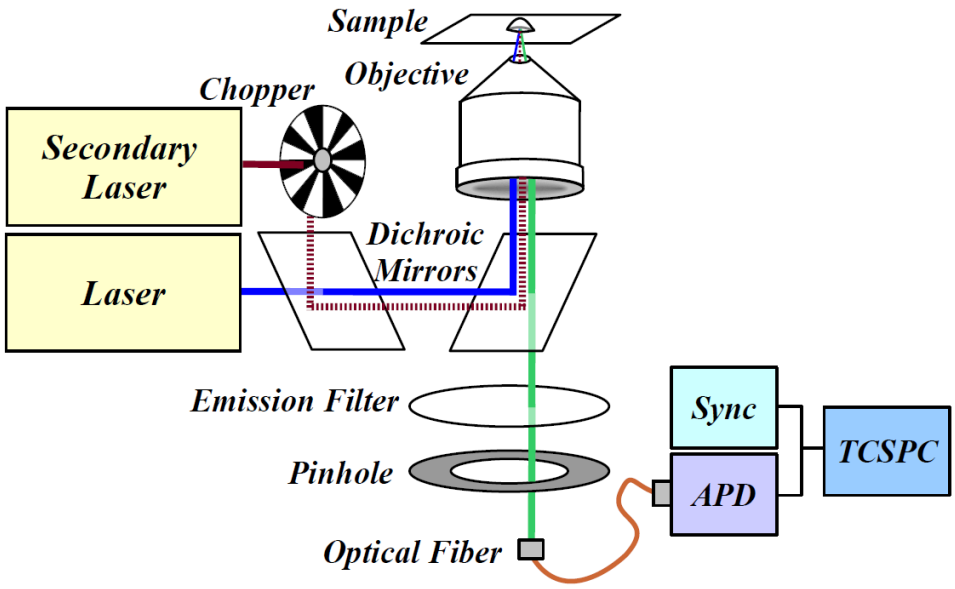

Figure 2.4: Schematic of a dual-laser FCS experiment. Excitation is shown in blue, emission in green, and secondary illumination in red. Beams are shown side-by-side for clarity but would be colinear in experiment. Avalanche photodiode - APD; External sync source - Sync; Time-correlated single-photon counting module - TCSPC

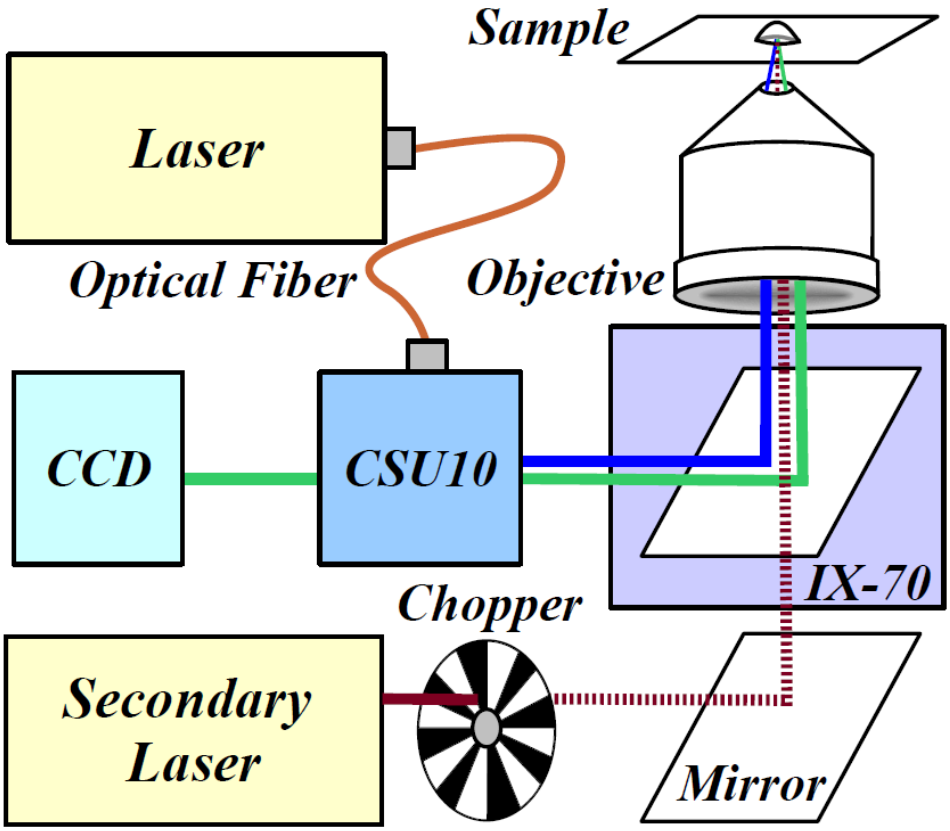

Figure 2.5: Schematic of a dual-laser spinning disk confocal experiment. Excitation is shown in blue, emission in green, and secondary illumination in red. Beams are shown as single side-by-side beams for clarity but would be colinear and multiple, for excitation and emission, in experiment. Yokogawa Confocal Scanning Unit - CSU10; Olympus inverted microscope - IX-70; Andor iXon EMCCD camera - CCD

CHAPTER III

WIDEFIELD CROSS-CORRELATION SPECTROSCOPY FOR FLOW IMAGING IN MICROFLUIDIC CHANNELS

3.1 Introduction

Microfluidic devices have become the basis for automated sensors and miniaturized chemical reactors in a wide range of applications [186, 187, 188]. To accommodate high throughput, even with low sample volume, these devices are becoming increasingly intricate, with additional functionalities packed into ever smaller designs. Often solution handling, processing, and sensitive detection are all to be performed on the same microscale device. The advent of 'nanofluidics', in which surface effects and fabrication processes play a large role in device performance, and the common need to direct analyte to the surface for sensing, make imaging the resulting flow inside devices more difficult [189]. Most flow imaging techniques rely on tracking many particles moving with the flow stream to determine their motion through consecutive images. Such methods require following large numbers of individual particles, but may still ineffectively map flow through all areas of the channel [76].

Brightly fluorescent tracer particles are often utilized to enable high signal, but the high concentrations necessary to rapidly map out flow leads to high background from out-of-focus tracer particles. Such single particle imaging requires a high number of photons per frame, coupled with efficient background rejection and tedious analysis to map out only a subset of flow vectors within the channel. Following rapidly flowing particles requires high frame rates and therefore bright particles (*e.g.* fluorescent beads of several hundred nanometer diameter). As microfluidic devices shrink, tracer particles must also become smaller, thereby limiting brightness. Below a certain

brightness threshold it becomes impossible to localize the individual particles in the image, precluding particle tracking algorithms from determining the flow speeds in the system [190].

Fluorescence Correlation Spectroscopy (FCS) and fluorescence cross-correlation spectroscopy (FCCS) have both been successfully applied to measure flow within microfluidic channels [191, 23, 27, 192, 193]. Such methods offer efficient background rejection due to imaging of fluorescence fluctuations due to dye or tracer traversal through individual (FCS) or pairs (FCCS) of diffraction-limited volumes [55, 56, 57, 58]. While background is efficiently rejected due to collection through a pinhole, the spatial resolution is severly limited, making the task of mapping the flow vectors in the entire channel arduous [25].

FCCS uses two focal volumes and the cross-correlation of the two signals from the individual focal volumes to improve flow measurements over that possible with FCS [59, 21, 22]. The cross-correlation that is generated has a maximum value whose position is dependent on the flow speed, distance, and angle between the flow vector and the vector connecting the two focal volumes (see section 3.2 **Theory** below). Cross-correlation analysis has some important advantages over autocorrelation techniques - the cross-correlation is more tolerant of non-ideal focal volume shape and saturation effects while simutaneously being more robust at measuring directional flow [194, 195]. Most importantly, FCS measures fluctuations in a single symmetrical focal spot, precluding the determination of direction in flow while the pair of spots in FCCS allows both speed and direction to be measured.

Combining the particle averaging advantages of FCCS and the large-area imaging of particle tracking would be beneficial in mapping flow. To reduce out-of-focus fluorescence a Spinning Disk Confocal Scanning Unit (CSU) enables visualization of fluorescence from a single image plane. Here, we develop optically-sectioned fluorescence cross-correlation imaging for rapidly measuring steady-state flow throughout

the entire channel.

The Yokogawa CSU unit consists of a pair of spinning disks, one with a series of pinholes, the other with aligned micro lenses, that trace out illumination over a wide area as the disks spin. The resulting emission is collected through the same set of pinholes, which rejects light from other focal planes and constrains the field of view in the axial (z) direction. The resulting confocal images are captured at high frame rates on an electron-multiplied CCD (EMCCD) camera. The EMCCD allows for detection of fluorophores with high sensitivity in a widefield configuration. With each pixel in the CCD acting as a focal volume, cross-correlations can be calculated by correlating the fluorescence *vs.* time trace between any two arbitrary pairs of pixels throughout the focal plane [65, 64]. Changing the focal plane in the z direction yields a map of the cross-correlation parameters through the entire volume of interest. Such a setup has previously been used with FCS to measure diffusion in aqueous solutions and collagen matrices [67].

The technique presented here provides a method to measure the amplitude and directional flow of particles through a large volume of interest. FCS and FCCS have been employed to measure flow speeds [21, 22, 23] or directions [24] in microfluidic devices. By repositioning the microscope objective, some have extended this to imaging beyond individual spots or pairs of spots to three dimensions as well [25, 26, 27]. However, to image an entire volume, these methods rely on taking individual intensity *vs.* time traces at each position. Here, data for all points in a single focal plane are recorded at once. From this, the individual time traces are reconstructed later, greatly reducing the total acquisition time versus serial repositioning of a single sample volume. At a single focal plane, the same data set can be used to also reconstruct the total flow vector, eliminating the need for repositioning the detection volume during data aquisition.

Extending flow measurements to allow motion in the axial direction, perpendicular

to the focal plane, to be quantified, has been attempted through several different experimental arrangements with some success. Three-dimensional extensions of particle velocimetry imaging (PIV) have existed for some time but necessitate multiple lasers or CCD cameras, greatly increasing the cost of such a setup. Similar adaptations to particle tracking (PTV) experiments have been performed, often at the expense of real-time feedback systems or previous knowledge regarding the motion in the system of interest. Mathematical assumptions can greatly simplify the measurement of these axial flows from planar flow measurements, but do not actually result from an experimental measurement of the axial flow. Single-point flow measurements utilizing variations of fluorescence correlation spectroscopy (FCS) have also been used, with some success, to measure out-of-plane flows in microfluidics and blood vessels of live organisms [26].

Particle-tracking algorithms require that the tracers be visible in subsequent focal planes, necessitating a high signal strength, which is compounded by the fact that a signal from a particle decreases as it leaves the focal plane. Single-point correlation techniques are limited by the small area probed in a single experiment, which is an even greater issue when the flow in an entire 3-D volume is of interest.

The nature of the steady-state analysis can determine flow velocities with probe brightnesses much lower than can be handled by particle-tracking algorithms. Because of the generality of this method, the technique could also be applied to motion or transport along cellular structures. In addition, because the original data is recorded as images, other desirable variables can be extracted from the same data set.

3.2 Theory

Fluorescence correlation spectroscopy uses the fluctuations of the fluorescence signal at time t about the mean fluorescence intensity, given by

$$\delta F(t) = F(t) - \{F\} \tag{16}$$

where the brackets indicate an average over time. The normalized cross-correlation function, $G_{cc}(\tau)$, resulting between the fluorescence signals F_1 and F_2 of two focal volumes, P_1 at position $\vec{r}$ and P_2 at position $\vec{r'}$, is given by

$$G_{cc}(\tau) = \frac{\{F_1(t,\vec{r})F_2(t+\tau,\vec{r'})\}}{\{F_1\}\{F_2\}} \tag{17}$$

in which the brackets indicate an average over all time t. From the equation 17 and those appearing in [21], the cross-correlation function for a system experiencing directional flow is given as

$$G_{cc}(\tau) = \left[N(1+\frac{\tau}{\tau_D})\sqrt{1+\frac{\omega_o^2\tau}{z_o^2\tau_D}}\right]^{-1} exp\left[-\frac{R^2}{\omega_o^2}\frac{1}{(1+\frac{\tau}{\tau_D})}\left(\frac{\tau^2}{\tau_{Flow}^2}+1-2\frac{\tau}{\tau_{Flow}}cos\,\alpha\right)\right] \tag{18}$$

where τ_D and τ_{Flow} are the time scales for diffusion and flow, respectively, and N the average number of molecules crossing between the two focal volumes. The derivations of this and subsequent equations are covered in more detail in appendix A. The two detection volumes are assumed to be equal volume 3-D Gaussians with $1/e^2$ radii ω_o and z_o in the xy and z directions, respectively, and separated in the xy plane by the "spacing" vector $\vec{R}$, with length R and in-plane angle α relative to the vector of flow. In this work the spacing vector is that connecting the center of each pixel pair chosen by the algorithm for generating each cross-correlation, the set of which yield the flow direction at each point.

The applicability of the cross-correlation analysis requires flow to be constant in speed and direction within the analysis volume and measurement acquisition time. In addition, the flow can be assumed to be much faster than diffusion, such that $\tau_{Flow} \ll \tau_D$, which simplifies equation 18 to

$$G_{cc}(\tau) = \frac{1}{N} exp\left[-\frac{R^2}{{\omega_o}^2}\left(\frac{\tau^2}{{\tau_{Flow}}^2} + 1 - 2\frac{\tau}{\tau_{Flow}}\right) cos\,\alpha\right] \tag{19}$$

which has a maximum value at $\tau = \tau_{Flow}\, cos\,\alpha$. For flow of unknown angle, the flow vector can be determined by exploiting the cosine dependence between the flow vector and the spacing vector, $\vec{R}$. The vector-variant flow analysis is described in more detail in section 3.3.5.

For flow in a single direction over the entire volume of interest, the form of the cross-correlation can be further simplified to reduce computational time. By choosing a spacing vector that is parallel to the flow vector, the $cos\,\alpha$ term is reduced to 1, reducing equation 19 to

$$G_{cc}(\tau) = \frac{1}{N} exp\left[-\frac{R^2}{{\omega_o}^2}\left(\frac{\tau^2}{{\tau_{Flow}}^2} + 1 - 2\frac{\tau}{\tau_{Flow}}\right)\right] \tag{20}$$

Here the maximum of the cross-correlation function is simply at τ_{Flow}, and since R is known, the flow speed at that point is given by

$$V = \frac{R}{\tau_{Flow}} \tag{21}$$

The details of the the flow analysis algorithm are covered in more detail in sections 3.3.4, 3.3.5, and 3.3.6. For constant-angle flow, pixel pairs separated by a constant spacing of distance R and parallel to the flow vector are iteratively repositioned throughout the image space and the resulting cross-correlation are fit to equation 20. The τ_{Flow} value at the location of the pixel pair is used with equation 21 to map the flow speed in the image space. Varying or unknown flow requires that the flow angle first be determined. For this, a central pixel is chosen and cross-correlations between this and a set of surrounding pixels are taken. From either the amplitudes or measured τ values of these cross-correlations as a function of position the flow angle, and subsequently the velocity can be determined.

The derivation of equation 18 invokes Gaussians to describe the shape of the focal volumes. Pixels of a CCD have definite non-Gaussian character, and previous works have defined the relevent physical parameters in terms of the pixel dimensions [196] or introduced corrections to ω_0 to account for this [67]. While these corrections were necessary for autocorrelations, the comparative robustness of the cross-correlation to the non-Gaussian character of the detection volumes makes these corrections unnecessary in this work [194].

3.3 Experimental

3.3.1 Experimental Setup

The experimental setup was based on a spinning disk confocal scanner (Yokoagwa CSU 10) mounted on an inverted microscope (Olympus IX 70). Imaging was achieved with a 1.2 NA 60x water immersion objective. Microfluidic channels (50 μm by 50 μm cross-section) were molded in poly(dimethysiloxane) (PDMS) and sealed on a glass coverslip. For the 3-D flow mapping experiments a y-shaped channel was used with a single input, a long ($>$ 5 mm) straight section, then a fork to two outputs. In the case of measuring axial flow a channel designed to yield a vortex along the flow direction was used.

Flow was achieved by loading a solution of fluorescent beads or dye into the inlet tube on one side of the channel and gravity-fed through the device or by syringe pump. The 496 nm line from an Ar^+ laser (Coherent Innova 90) was aligned into a 3.5 μm optical fiber, coupled into the scanner, and routed through the side port of the microscope. The excitation was directed through the microscope objective, exciting the tracer particles (fluorescein-impregnated polystyrene fluorescent beads of 100 nm or 20 nm nominal diameter or Alexa 488-labeled anti-mouse IgG).The emission was collected through the same objective, side port, and scanner, through the dichroic and emission filters inside the scanner, before detection with a back-illuminated EMCCD

camera (Andor iXon DV887).

To increase the frame rate of the camera, only a limited area of the CCD was used and pixels were binned together (4x4 bins). With these accommodations, an area of 100x512 pixels with 4x4 pixel bins could achieve over 1000 frames per second and full-frame images of 512x512 with 4x4 binning (creating 128x128 superpixels) up to 150 frames per second. The finite number of pinholes of the spinning disk requires that the frame rate of the camera be synchronized to the rotation of the disk, so the frame rates used were the fastest possible that achieved the necessary synchronization.

All chemicals were used as received. Alexa Fluor 488 and Alexa Fluor 488-conjugated anti-mouse IgG and 100 nm FluoroSpheres fluorescent microspheres were obtained from Invitrogen (Carlsbad, California, USA) and Polyethylene Glycol 8,000 (PEG 8K) was obtained from Teknova (Hollister, California, USA).

3.3.2 Data Analysis

A series of images, typically 1000-50,000 frames, in a single focal plane were collected. A collection of these image stacks taken at a sequence of z-positions constituted a data set. Data sets were exported as ASCII files and analyzed in MATLAB on a PC.

3.3.3 Flow Simulations

Imaging of flow was simulated in MATLAB with initial particle locations being evenly distributed randomly in 3-D across a 100x100 pixel CCD image. The z position of the particle was used to simulate the effect of focal depth in the system. A pre-chosen parabolic flow function was used to translate the center positions of each of the points for the subsequent frame based on the current position. The flow function was a parablolic displacement along the x-axis of 1.0 pixels/frame at the peak and 0 at the walls with additional 3-D diffusion appropriate for 100 nm beads. Simulations and experience indicate that 0.5 pixels/frame is an optimum flow rate for the cross-correlation algorithm described here (data not shown). From the (x, y, z) position

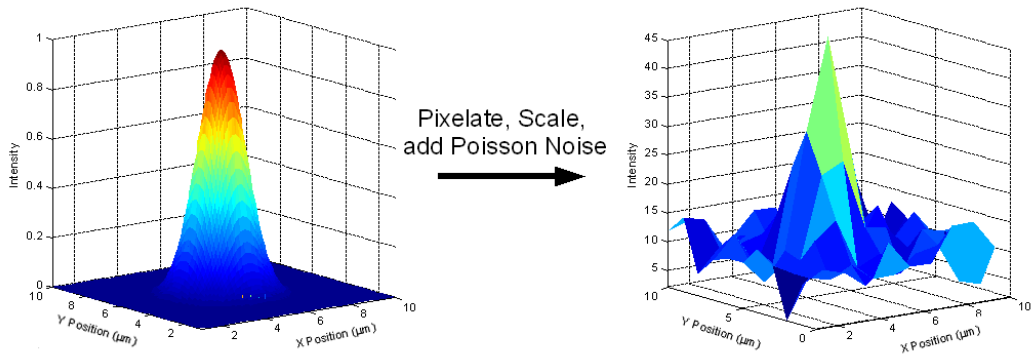

Figure 3.1: Generation of simulated bead images - first a center point for a bead is generated, which is then used as the center point for a 2-D projection of a Gaussian. The Gaussian is scaled, a constant background added, pixelated to simulate CCD images, and Poissonian noise added based on pixel intensity. A peak with S/N = 3.4 is shown here.

of the particle centers, an image frame was generated by modeling the intensities as symmetric 2-D Gaussian distributions.

$$I = I_0\, exp\left(\frac{-[(x-x_0)+(y-y_0)]^2}{2\sigma_{xy}^2}\right) exp\left(\frac{-z^2}{2\sigma_z^2}\right) \tag{22}$$

Here, σ_{xy} and σ_z represent the e^{-2} radii of the experimentally-determined PSF for the system. To simulate the pixelation from the CCD, the function was only evaluated in integer steps in the xy direction. The zero for the z-axis was taken as the focal plane and the distance above or below resulted in a change in intensity projected on the image.

Typically 10,000 frames were simulated, and the requisite number used to determine the image noise tolerance of the cross-correlation algorithm. To simulate Poisson noise inherent in CCD-based fluorescence imaging, the images generated as above were first scaled to a maximum intensity per particle from $10^{0.25}$ to 10^3 (1.77 to 1000) counts per frame. To this was added a constant background of 10 counts per frame. The value for the final intensity at each pixel was taken as a Poisson-distrubuted random number (generated with MATLAB's poissrnd function) with a mean equal

to the raw intensity (the sum of the scaled signal and constant background).

The S/N ratio for these images were determined by

$$\frac{I}{\sqrt{\sigma_{bkgd}^2 + \sigma_{obj}^2}} \tag{23}$$

with σ_{obj}^2 and σ_{bkgd}^2 as the variances of the signal and background, respectively. Here the noise is Poissonian, so these variances are also equal to the mean raw intensity values used to generate the simulated images. Substitution for the variance with the respective raw intensity yields the easily calculable equation 24.

$$\frac{\lambda}{\sqrt{10 + \lambda}} \tag{24}$$

Images were generated in this fashion with identical time-dependent particle locations, but with peak S/N values ranging from 0.8716 to 31.47.

The RMS deviation between the model and expected flow maps were defined as follows:

$$Error = \sqrt{\{Expected - Fit\}^2} \tag{25}$$

The expected values were taken from the initial displacements used (here, 1 pixel/frame in the center of the channel, 0 at the walls) to build the simulated image stacks, and the fits measured to determine the analysis algorithm's ability to return the expected values in the presence of varying amounts of Poisson noise. Because the flow speed was made to vary with the position along the x-axis, the fit values in a single column from the flow speed map were averaged in the determination of the error. Increasing number of frames for simulations generated with varying S/N ratios were taken when generating the cross-correlation.

Simulations for estimating the experimental limits of the different flow mapping

algorithms were performed in a similar manner as above with some alterations generating the specific properties of interest. In all cases constant flow through the entire region of interest was simulated along with appropriate diffusion of the simulated particles (100 nm beads if not otherwise stated). Acquisition rates for all simulations were held at 100 Hz with pixels corresponding to 1 μm in the image plane.

For the in-plane angle fitting algorithm flow was simulated at a S/N of 31.47 and speed of 0.5 pixels per frame. For each stack of 10,000 frames the flow direction was varied from 0 to 2π radians relative to the x-axis. A similar method was employed for axial flow angles, but with the axial flow angle varying from 0 to π radians relative to the focal plane and the in-plane angle held constant at $\pi\backslash 2$ radians relative to the x-axis. To replicate experimental data two focal planes of a spacing of 4 μm in the axial direction were simulated (20,000 frames each) and then interlaced, resulting in a single image stack with alternating images corresponding to the two focal planes. In order to determine the influence of diffusion on the resulting flow map data at a range of flow speeds was simulated for each of four diffusion constants (appropriate for 10 nm, 50 nm, 100 nm, and 1000 nm beads in water). The results generated from the analysis of these diffusions is discussed in the subsequent sections.

3.3.4 3-D Flow Mapping

To create a map of flow velocities in 3-D, a series of flow maps in 2-D are first determined and later reassembled to form the flow map for the entire volume. For a 2-D flow map, the analysis algorithm chooses a pair of pixels in the image stack separated by constant spacing vector, $\vec{R}$, which has length R and is parallel to the flow vector.

This vector is initially set in a distance in pixels in the image stack to be analyzed, but this is easily converted to units of distance (*e.g.* μm) upon calibrating the effective object-space pixel dimensions. The data for each of the pixels in the pair through

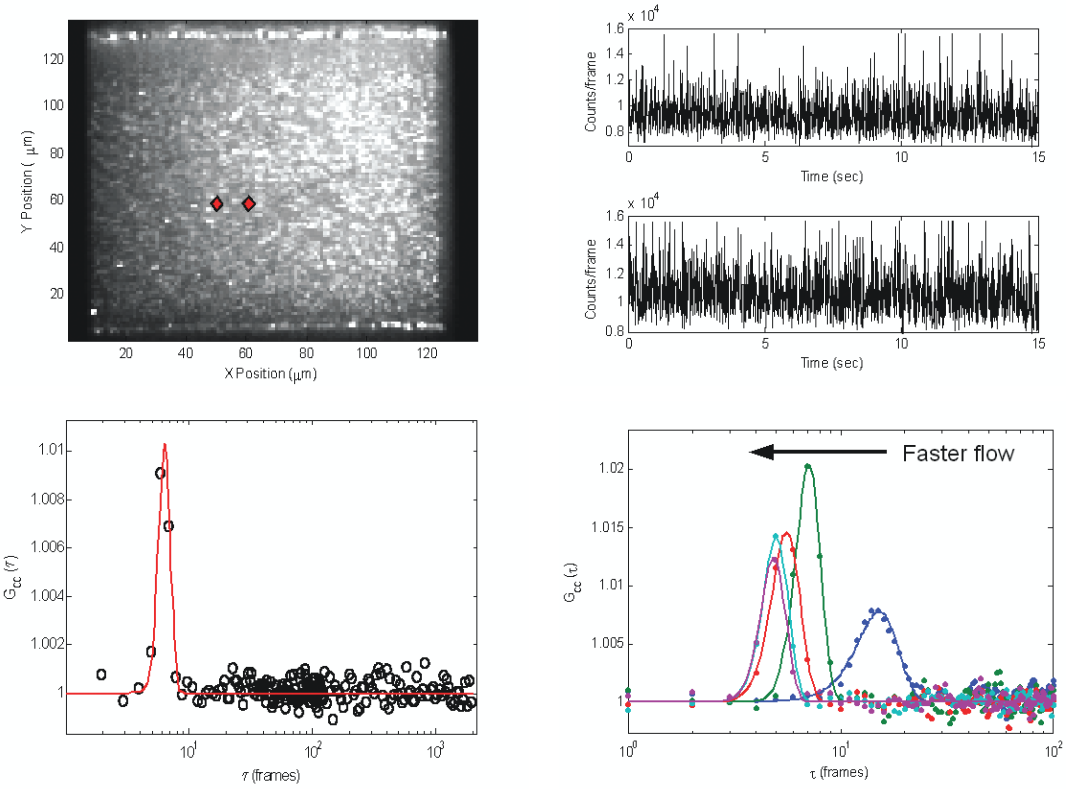

Figure 3.2: Cross-correlation between a single pair of pixels: 2(a) Fluorescence image with pixels chosen for cross-correlation(diamonds); 2(b) Intensity *vs.* time traces for pixels chosen; 2(c) Resulting cross-correlation (circles) and fit (red line) from two pixels; 2(d) Cross-correlations between pixels of constant spacing moving from wall to center of channel (right to left). The peak position shifts to shorter delays with increasing flow speed.

the entire image stack are transformed from intensity *vs.* position plots to a pair of intensity *vs.* time traces. The cross-correlation of the intensity *vs.* time traces is fitted to equation 20, yielding τ_{Flow}, and then velocity (V) from equation 21. The resulting velocity is mapped back onto the position of the upstream pixel of the pair. Iterating the position of the pixel pair with constant spacing vector throughout the entire xy image results in a 2-D flow map, a series of which can be stacked at known positions along the z axis to form a 3-D flow volume map.

3.3.5 Flow Angle Fitting

While straight sections of a microfluidic channel operating under laminar flow conditions rarely see any significant deviation from a single flow direction, there are many areas surrounding bends, obstructions, or other inconsistencies in a channel that alter both the magnitude and direction of flow. To determine both components of the flow vector in such a case, the dependence of the cross-correlation function on $cos\,\alpha$, as seen in equation 19 is exploited. For a single cross-correlation, the apparent τ from the fit will follow the form

$$\tau = \tau_{Flow}\, cos\, \alpha \tag{26}$$

in which α is the angle between the spacing vector and the flow vector. As diagrammed in Figures 3.3 and 3.4, choosing a series of pixels about a central pixel and taking the cross-correlations between the central and surrounding pixels, a plot of the measured τ/R values *vs.* β, the angle between the spacing vector and an arbitrary zero angle vector, will result in a cosine curve with an amplitude τ_{Flow} and phase Ψ. To produce a full 2π range of angles, both the forward and reverse cross-correlations are performed for each pair of pixels. The cross-correlation that fits best and yields the greatest τ value of the two is chosen as the data point for that β, with those taken from reverse cross-correlations taken as the negative.

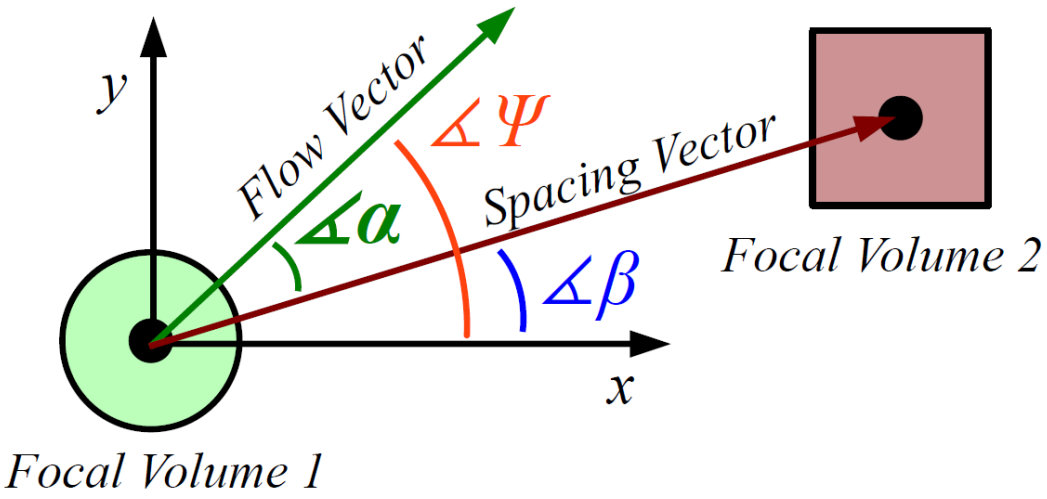

Figure 3.3: Diagram of angles used in angle-fitting analysis. Here, α designates the angle between the flow vector and the spacing vector, $\vec{R}$, β the angle between $\vec{R}$ and the x-axis, and Ψ that between the flow vector and x-axis.

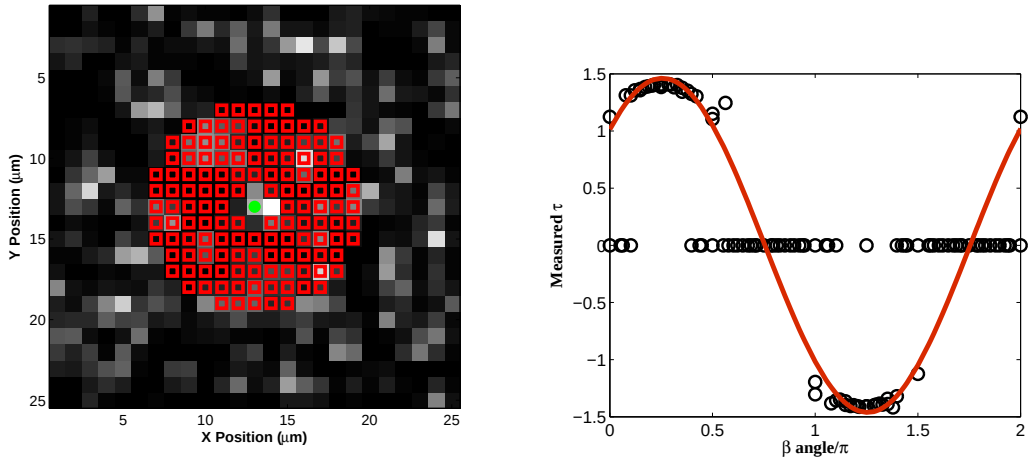

(a) (b)

Figure 3.4: 4(a) From single simulated image (of 50,000), center point (green circle) is chosen. Cross-correlations between this point and many surrounding points (red squares) are taken. 4(b) Measured τ as a function of angle β from cross-correlations determined between points in 4(a) (circles) and fit (red line). Those values not fitting within constraints are set at $\tau = 0$ and not included in the fit.

In practice, it is challenging to take advantage of the cosine dependence because of the highly directional flow. A more effective method involves mapping the maximum amplitude of the cross-correlation between a central and surrounding pixels onto the position of the surrounding pixel. The cross-correlation amplitude function can be found by substituting the value for the peak position (equation 26) for τ in equation 19, yielding equation 27.

$$G(\tau_{max}) = S\frac{1}{N}exp\left[\left(\frac{R^2}{\omega_o^2}\right)sin^2\alpha\right] \tag{27}$$

To remove the ambiguity in the angle resulting from the identity $sin^2(\alpha) = sin^2(-\alpha)$ an additional parametric term, S, is introduced (eqn. 28).

$$S = \begin{cases} 1 & : \quad -\frac{\pi}{2} \leq \alpha \leq \frac{\pi}{2} \\ -1 & : \quad -\frac{\pi}{2} > \alpha > \frac{\pi}{2} \end{cases} \tag{28}$$

As before, forward cross-correlations between the center pixel and surrounding pixel are taken as positive values and the reverse cross-correlation as the negative. Once the value for the angle is known, the velocity can be determined using equation 26 with pixel pairs most closely colinear with the determined flow angle. While equation 26 relies on values returned from the fitting of cross-correlations, equation 27 determines angles when using the maximum of the measured cross-correlation, removing the need for an accurate fitting to a potentially noisy data set. This shortcut does not allow for the highest precision when mapping maximum correlation amplitudes, but this lack of precision is of little consequence when averaged out in the subsequent fitting of the cross-correlation map.

Pixel pairs that are far from the flow vector will return poor cross-correlations of low intensity. Fitting the peak position rather than the amplitude weights these pixels equally with those closer to the flow vector and so a fit to a noisy correlation

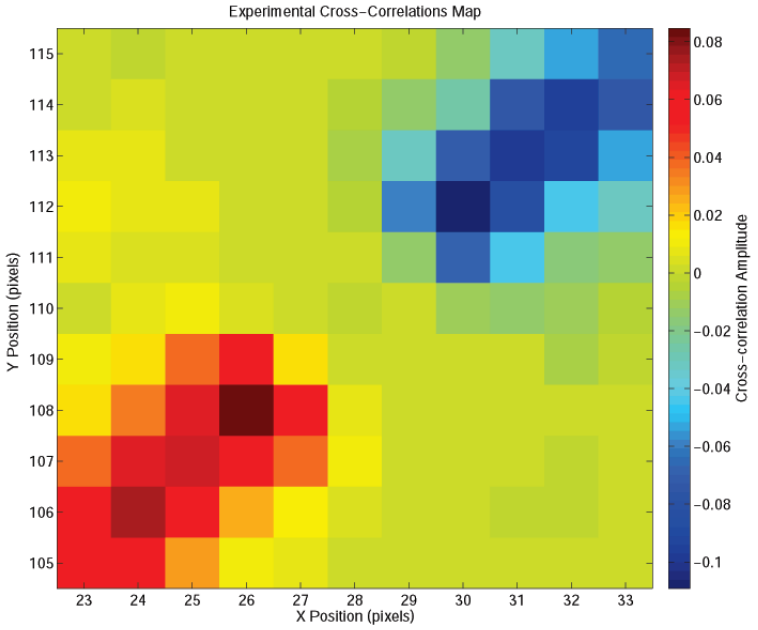

(a)

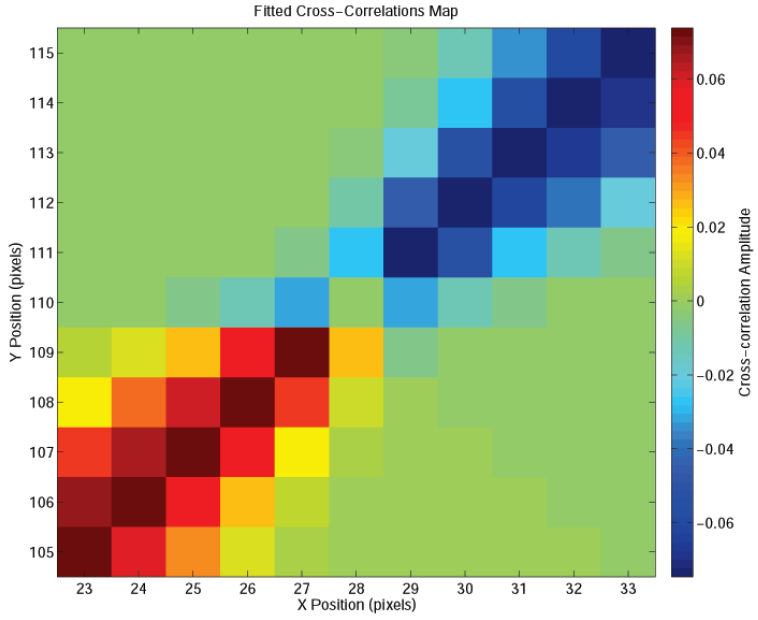

(b)

Figure 3.5: 5(a) Measured cross-correlation amplitude map for a single central pixel and set of surrounding pixels. 5(b) Calculated map fit to 5(a) using equation 27. Result is fit with angle of -2.386 radians.

would obscure the expected cosine dependence. To avoid such an issue, strict constraints must be placed on the acceptable τ values returned by the algorithm. In addition, very large (upwards of 50,000 frames) data sets are required in order to improve the quality of the cross-correlations and therefore accuracy of the returned τ value. With the amplitude-mapping algorithm those poor cross-correlations have low amplitudes and pixel pairs closer to the flow vector will yield cross-correlations of higher amplitude, effectively weighting the angle fit in favor of directions of higher-quality cross-correlations and closer to the true flow angle. This results in an order of magnitude decrease in the length of the necessary data set and an increase in accuracy in the flow vector measurements over the method relying on measured delays.

3.3.6 Axial Flow Mapping

Extending the analysis to allow for 3-D vector information requires the adaptation of previous equations to include both axial and planar components. The nature of cross-correlation analysis requires that data taken at different focal planes be on the same time axis in order to generate a correlation. This is accomplished experimentally by rapidly repositioning the focal plane of the objective with a piezo nosepiece driven by a periodic square-wave type function. Imaging rates of the CCD correspond to twice that of the repositioning function, resulting in data from the two focal planes being interlaced in the experimental data set.

The labels and geometry for this method appears in figure 3.6. Here, the flow angle is separated into the planar and axial components (θ and ϕ, respectively) and the general angle is designated as α. The measurement relies on taking cross-correlations at two focal planes, designated as the *High* and *Low* planes (henceforth H_a and L_b, where $a, b = 1, 2$, specifying which of the 4 possible positions) separated by distance $\vec{R}_z$. The total distance between two focal volumes (P_1 and P_2) is $\vec{R}$ which can be determined from the in-plane projections $\vec{R}_{planar}$ and $\vec{R}_z$ with equation 29.

$$\vec{R} = \sqrt{\vec{R}_{planar}^2 + \vec{R}_z^2} \tag{29}$$

In order to perform the axial angle-finding analysis a series of points about a central pixel are chosen and the intensity *vs.* time traces for all pixels are extracted from the data set. These traces contain data for both focal planes in alternating time steps so each original time trace is unstitched into two time traces corresponding to data at a single focal plane each. Between a single pair of pixels there are four time traces (two pixels and two focal planes each) and a resulting 12 possible cross-correlations (see Figure 3.7). Of this set of cross-correlations, only four are used to determine the axial angle and another four to determine the velocity. Two maps, referred as the, 'forward,' and, 'reverse,' maps, created from mapping the maximum amplitude of the $(H_1 : L_2 - L_2 : H_1)$ and $(H_2 : L_1 - L_1 : H_2)$ functions. Subtracting reverse cross-correlations removes the influence from auto-correlations in the cross-correlation functions. These maps can be fit to equation 30 to return the planar and axial flow angles. To determine the flow speeds the measured delays (τ_{Planar}) of single-plane cross-correlations ($H_1 : H_2, H_2 : H_1, L_1 : L_2$, and $L_2 : L_1$) were utilized in conjunction with equation 31.

Separating equation 27 into the planar and axial components yields equation 30.

$$G(\tau_{max}) = \left\{ \frac{1}{N_z} exp\left[\left(\frac{R^2}{\omega_z^2} \right) sin^2\phi \right] \right\} * \left\{ \frac{1}{N_{xy}} exp\left[\left(\frac{R_{planar}^2}{\omega_{xy}^2} \right) sin^2\theta \right] \right\} \tag{30}$$

Equation 30 is fit to experimental data, yielding flow angles θ and ϕ, which can then be used to in conjunction with in-plane cross-correlation fits (utilizing equation 19, yielding τ_{planar}) to determine the amplitude of the flow velocity V via equation 31.

$$V = \frac{R_{planar}}{\tau_{planar}\, cos(\phi)\, cos(\theta)} \tag{31}$$

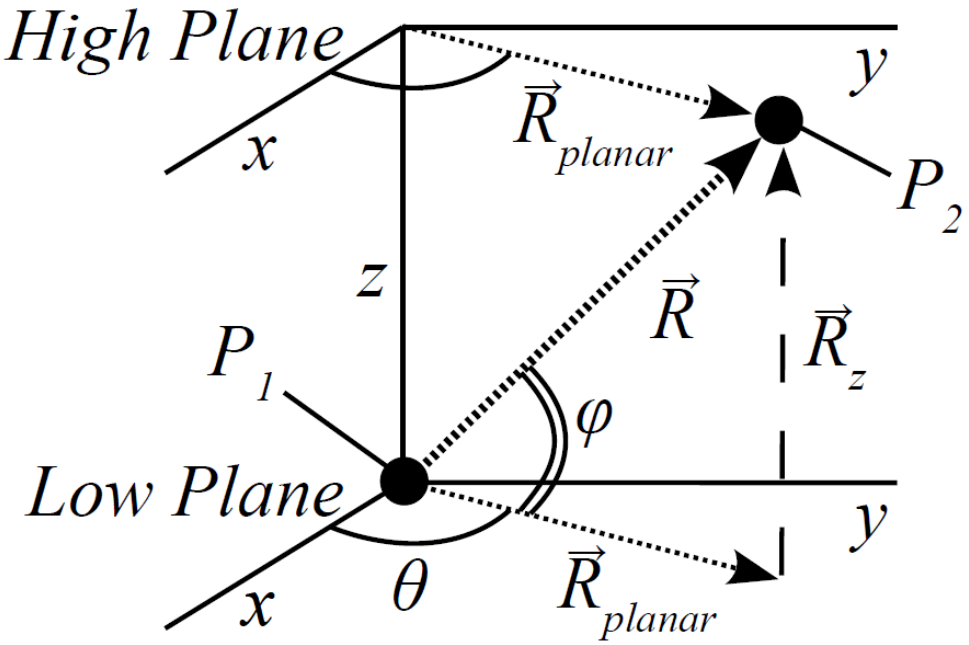

Figure 3.6: Diagram of labels used in axial flow analysis.

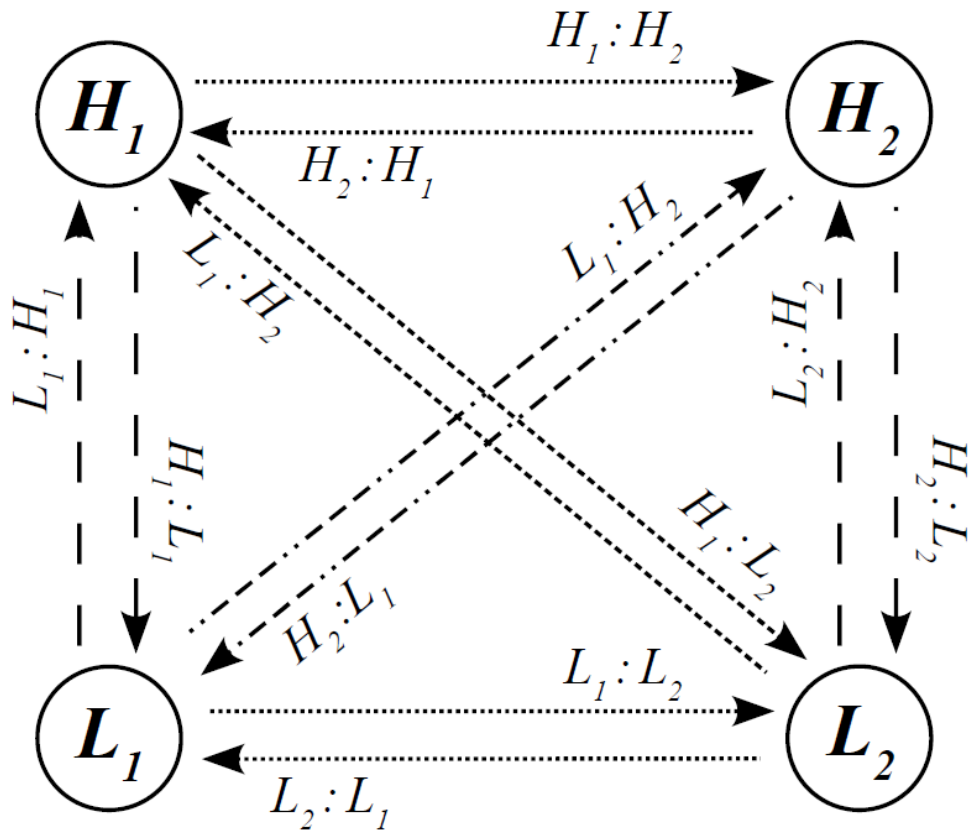

Figure 3.7: Diagram of cross-correlations possible in axial flow analysis.

Contrary to the angle-fitting algorithm, which uses forward and reverse cross-correlations simultaneously, the two correlation maps are treated separately here to yield a pair of results for θ and ϕ, with the appropriate rotation operation performed for fits in the reverse direction. The average value is used as the final experimentally-fit value.

A result of the mapping procedure yields an experimental amplitude map as seen in figure 3.8. The shape of this plot is an extension of the analagous plot generated in the angle-fitting algorithm in the strictly in-plane case in that the direction of the in-plane ridge corresponds to the planar flow angle. The position of the peak in the amplitude map is indicative of the axial flow angle.

There can be derived a set of equations to yield out-of-plane flow direction from the dependence on flow angle of the peak position, analogous to what has been demonstrated in equation 26. This approach is mathematically sound, but in practice proves prohibitively difficult for the same reasons that the in-plane angle fitting by way of peak positions was abandoned. For a given cross-correlation the peak position is essentially the position of the maximum value, which, for strongly correlated signals, is straightforward to determine. However, for weakly correlated signals, the resulting cross-correlation is essentially noise and the position of the maximum of that signal is random. It then becomes difficult to determine which peak positions can be trusted without some sort of scaling factor taking into account the strength of the correlation. This is exactly what occurs by fitting the peak amplitude as a function of spacing vector angle. Those signals showing a strong correlation rise above the background while the weakly correlated signals consistently yield low amplitude correlations and are consequently much less likely to interfere with the fitting routine.

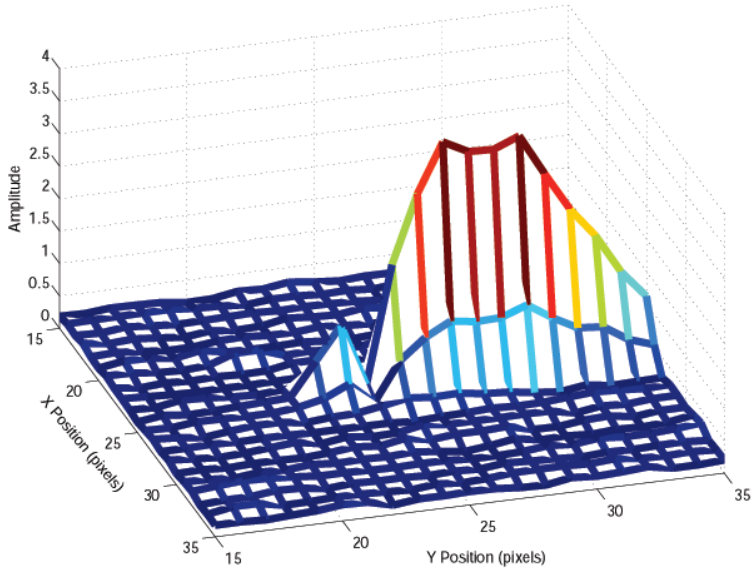

(a)

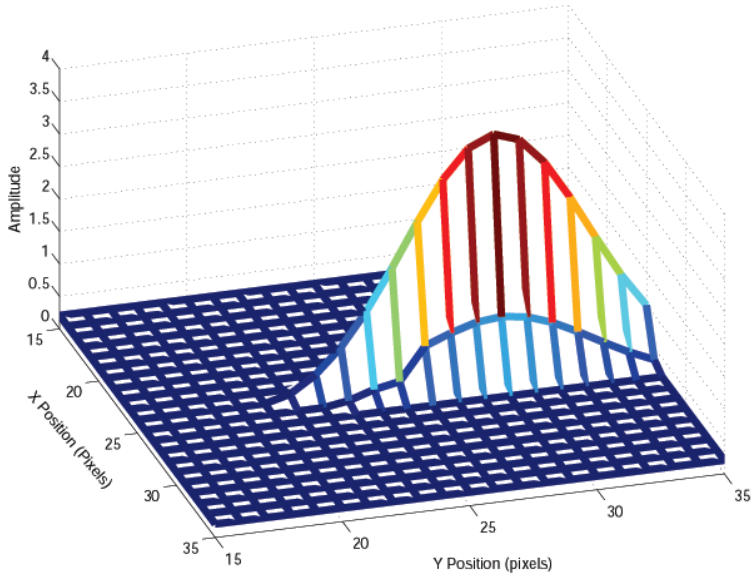

(b)

Figure 3.8: 8(a) Measured cross-correlation amplitude map for a single central pixel and set of surrounding pixels in a second focal plane in a simulated data set. 8(b) Calculated map fit to 8(a) using equation 30. Result is fit with in-plane angle of $\theta = \pi\backslash 4.07$ radians and axial angle $\phi = \pi\backslash 2.00$ radians to expected values of $\theta = \pi\backslash 4$ and $\phi = \pi\backslash 2$

3.4 Results and Discussion

3.4.1 Noise Tolerance

Cross-correlations have the distinct advantage of being able to accurately measure steady-state properties by trading precision in time for the often more important tolerance to noise. While particle tracking algorithms can more precisely determine the translation of a particle between one frame and the next, it comes at the cost of having to have particles bright enough to locate in every frame, requiring a S/N of around 4 to determine individual particle displacements with an average error of less than 0.1 pixels/frame[190].

The advantage goes to correlation analysis when the average across a larger time range is acceptable and steady-state values are desired. Only the intensity fluctuations corresponding to actual physical events are correlated - those due to noise are uncorrelated. In addition, fluctuations from particles making the transit through only one of the two focal volumes in a cross-correlation yield no contribution to the resulting correlation function. In particle tracking, out-of-plane diffusion seriously limits trajectory lengths.

An improvement in S/N of each image will improve the quality of the analysis in both correlation and particle tracking methods. For the most difficult case of fast-moving, dim particles, one can have longer exposure times or take more frames of data, both of which benefit correlation analysis, while for particle tracking, only the former is an available option. Because the particles must be located in each individual frame, more frames with too low a S/N will be of no benefit.

The resulting error in measuring flow speeds demonstrates the ability of the algorithm to tolerate a low S/N in the input image data. Simulations indicate that by sampling 10,000 frames, the maximum tested, a S/N as low as 1.4 will generate fits as good as any higher S/N value (see Figure 3.9). At these intensities, it is very difficult to find the particle locations, rendering particle tracking even more difficult,

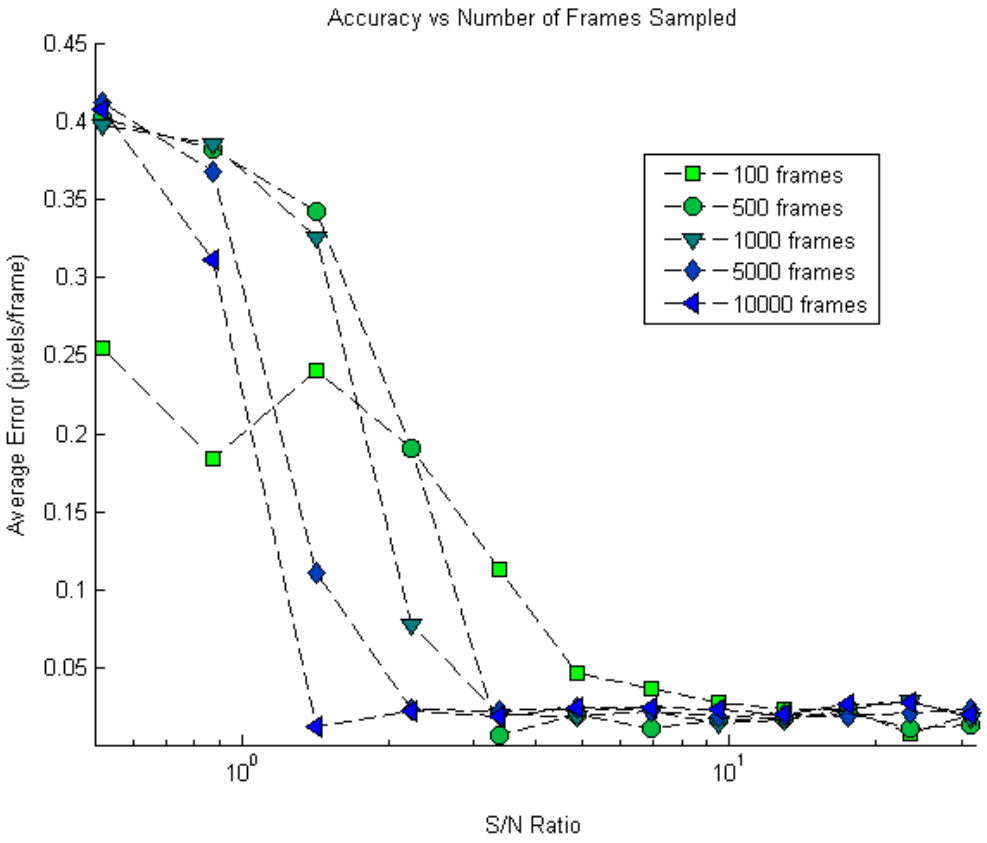

Figure 3.9: Relative error of the flow map with simulated data as a function of S/N of individual frames (eq. 24) and number of frames sampled. With 10,000 frames sampled a S/N as low as 1.4 is sufficient to obtain a correlation map comparable to higher S/N values.

if not impossible (see figure 3.10).

While particle tracking does allow one to know the exact positions of the imaged particles in each frame of data, this information does come at the cost of necessary S/N and often is unnecessary, especially for the application described here. For situations where the locations of the particles is unimportant but rather the average motion of the particles is of concern, the use of cross-correlation flow mapping allows the use of data with lower S/N with improved accuracy.

3.4.2 3-D Flow Mapping

As described previously, 3-D flow mapping is achieved by stacking the 2-D flow maps determined at the known axial distances at which the image stacks were recorded. From this determination of the flow volume, slices along any arbitrary vector or axis can be taken. The resulting plots of a microfluidic device show a radially symmetric cross-section with flow fastest in the center. To our knowledge, this is the first time the flow for an entire microfluidic device has been imaged using a correlation method. The obvious applications of this method include the straight-forward manner that devices can be screened for asymmetries and anomalies inherent in device manufacture.

The 3-D flow maps measured for a rectangular channel appear in Figure 3.12. Stacked correlation maps can be arbitrarily sliced to yield different views of the of the flow throughout the device volume. Here slices have been taken along three perpendicular axes. Flow speeds at different positions in the channel can be fit to the analytical solution for laminar flow in a rectangular channel [197, 27].

$$\nu_x(y,z) = \frac{\nu^*}{2} b^2 \left\{ 1 - \frac{z^2}{b^2} + 4 \sum_{n=1}^{\infty} \frac{(-1)^n}{\gamma_n^2} \frac{cosh[\gamma_n (y/b)]}{cosh[\gamma_n (a/b)]} cos\left(\gamma_n \frac{z}{b}\right) \right\} \tag{32}$$

$$\gamma_n = \frac{\pi(2n-1)}{2} \tag{33}$$

in which a and b designate the half widths of the rectangular channel and ν^* is the

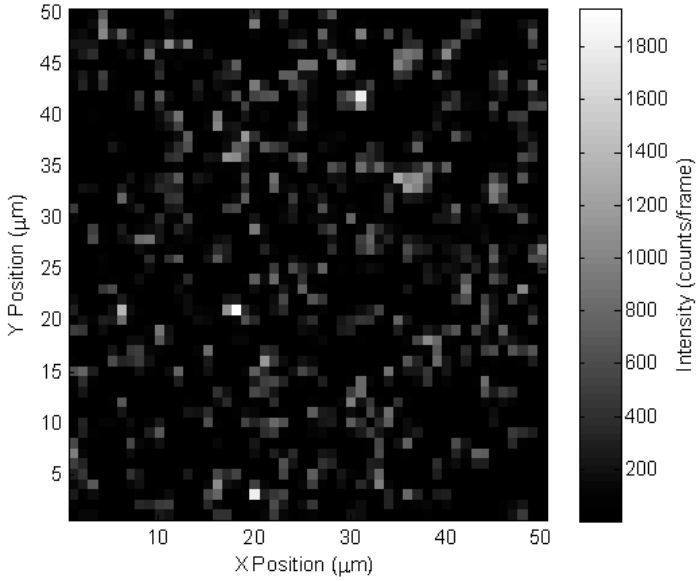

(a)

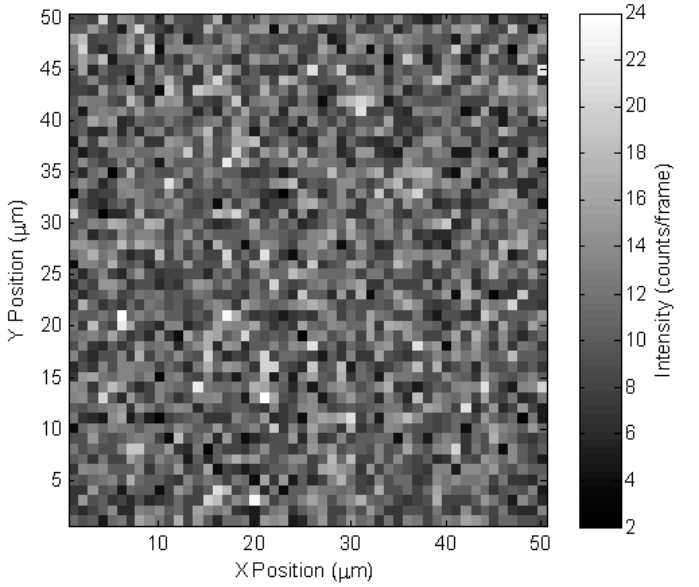

(b)

Figure 3.10: Pair of simulated images with identical bead positions with S/N ratios of 31.4 (10(a)) and 1.4 (10(b)) from a stack of 10,000 under a simulated parabolic flow between 0 and 1 pixels/frame towards the top of the image. With sufficient frames the flow map of both image stacks can be determined with an error less than 0.02 pixels/frame.

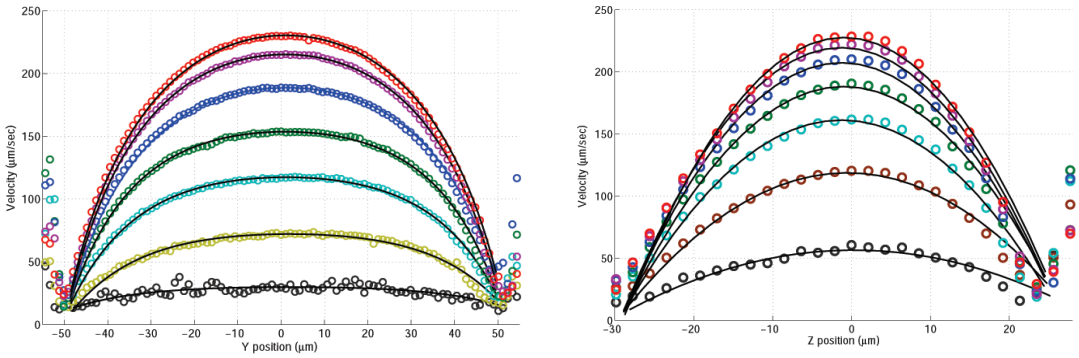

Figure 3.11: Velocity profiles taken along axes perpendicular to flow. 11(a) Data (circles) taken for varying z positions from bottom of channel (gray) to center (red). 11(b) Data taken along varying y positions from left (gray) to center (red) of channel. Fits to equation 32 in black.

characteristic velocity of the channel. The infinite series arises from the analytical solution for the correction of flow in a rectangular channel versus two infinitely-spaced parallel plates. Velocities were averaged along the flow direction at the desired positions to yield the data plotted in Figure 3.11. As seen, the data fit the expected form for a rectangular channel very well along the in-plane axis (xy) while there is a reasonable fit along the axial (z) direction. This slight asymmetry is suspected to be due to nonlinearities in the translation of the piezo nosepiece or influences of out-of-focus light in the correlation analysis. The curves approach, but do not reach, zero at areas of the channel near the wall. Without sufficient flow between the two focal volumes, there is little cross-correlation between the two resulting signals.

Experiments were commonly run at high enough concentrations of tracers to obscure the positions of the particles. At these higher concentrations the entire area of the channel is occupied with multiple particles at once, avoiding any danger of missing subtle effects in the channel from lack of recorded particle paths.

Because of the advantages afforded by correlation analysis, the option to reduce the size, and therefore brightness, of the tracer particles becomes possible. A single data frame and the resulting flow map appear in figure 3.13 While 100 nm radius beads were the typical tracer of choice, it was possible to image flow speeds with

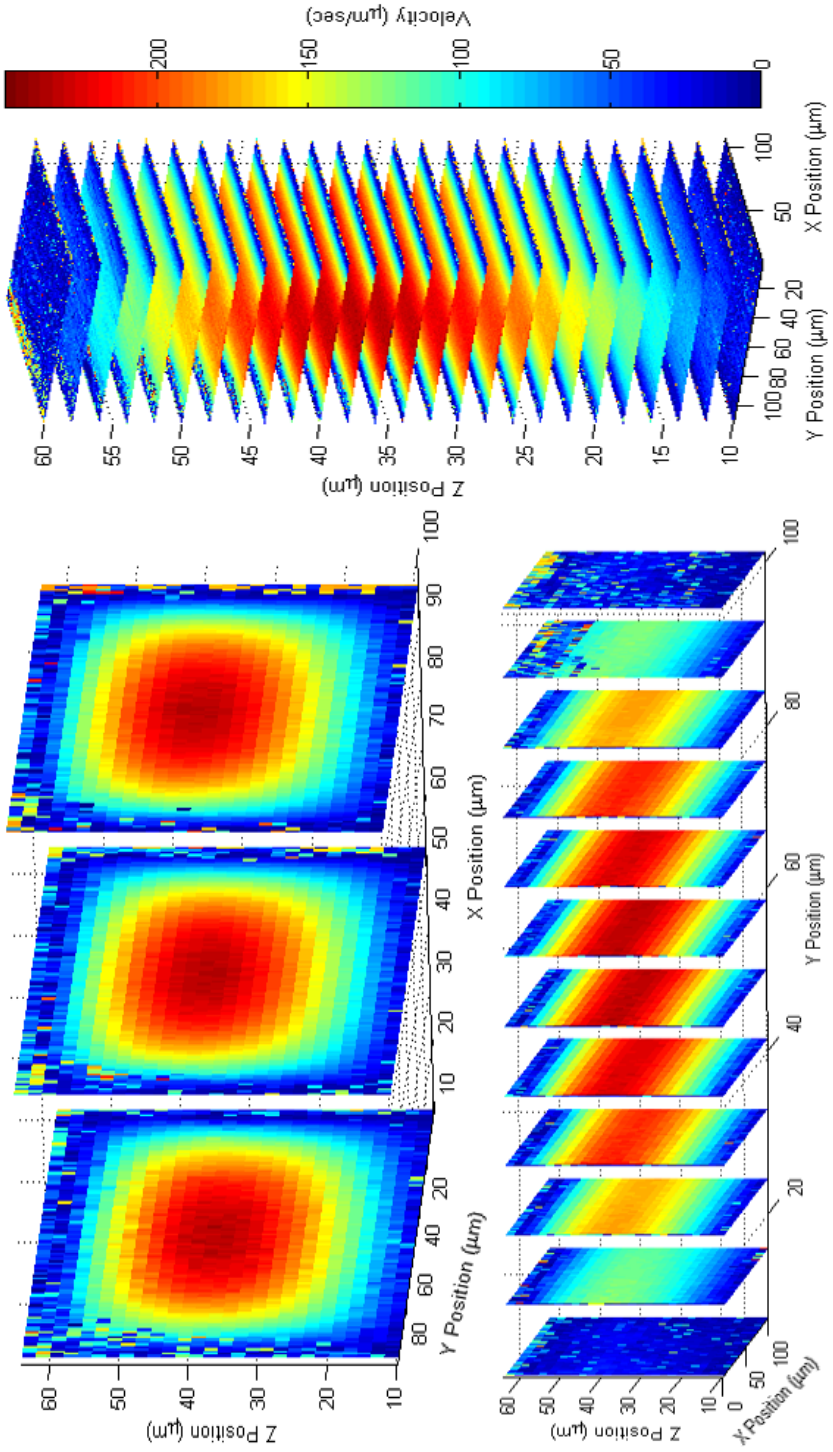

Figure 3.12: Slices of 3-D flow volume taken along perpendicular axes. Flow in channel was parallel to x-axis.

Table 1: Values used in the determination of the hydration radius of Alexa 488-labeled Anti-IgG. † - the diffusion constant (D) and hydration radius (R_h) of the free dye were taken from [1] and the diffusion time (τ_D) was measured experimentally.

Determination of Antibody Size				
Sample	$\tau_D(sec)$	$D(m^2s^{-1})$	$R_h(nm)$	Remarks
Alexa 488	4.718 (± 0.452) x 10^{-4}	2 x 10^{-10}	1.4	†
Anti-IgG	6.02 (± 1.79) x 10^{-3}	1.57 (± 0.526) x 10^{-11}	15.6 (± 4.6)	

20 nm radius beads and anti-mouse IgG antibodies conjugated to approximately 5-7 Alexa 488 dyes. Diffusion of the antibodies was retarded by adding 10% PEG 8K to the solution in order to decrease diffusion of the tracers out of the focal plane. FCS indicates the radius of hydration for these particles to be $R_h = 15.6 \pm 4.6$ nm. The hydration radius was determined through standard single-point FCS by ratiometrically comparing the diffusion time of the labeled antibody to a known standard, here free Alexa 488 dye. Details of the experimental data appear in table 1. From the experimentally-determined diffusion times (τ_D) and the known diffusion constant (D) of the Alexa 488 dye standard, the diffusion constant of the antibody was determined with equation 34. With knowledge of the solution parameters the hydration radius can then be determined with the Stokes-Einstein relationship (equation 35) [1]. The relevant parameters in equation 35 are k_B, the Boltzmann constant ($1.3806503 * 10^{-23} m^2\, kg\, s^{-2}\, K^{-1}$), T the temperature in Kelvin, η the viscosity of the solvent ($8.94 * 10^{-4} N\, m^{-2}\, s$ for water at 298 K), and R_h the radius of the particle (m).

$$\frac{\tau_{D,1}}{\tau_{D,2}} = \frac{D_1}{D_2} \tag{34}$$

$$D = \frac{k_B\, T}{6\, \pi\, \eta\, R_h} \tag{35}$$

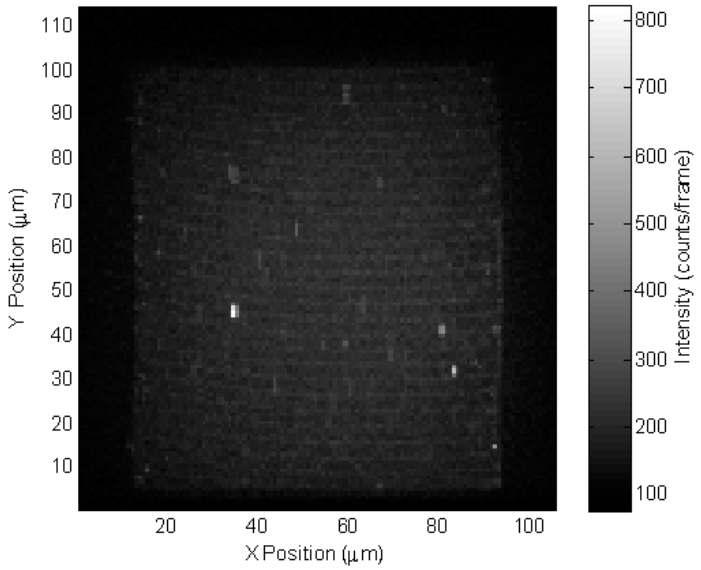

(a)

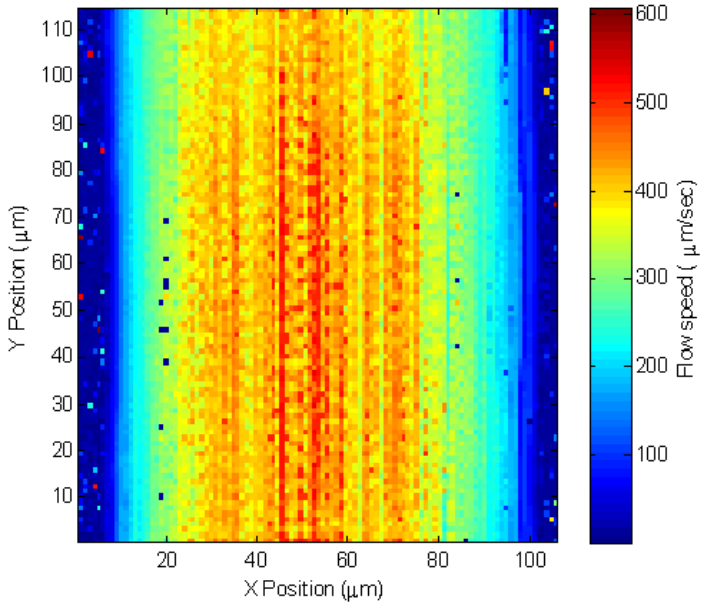

(b)

Figure 3.13: 13(a) Single frame of Alexa 488-labeled IgG in 10% PEG solution flowing towards top of image. 13(b) Measured flow for channel with labeled IgG as tracers. The streaks in the flow map result from a less-than-ideal concentration of tracers in the channel.

3.4.3 In-plane Flow Vector Determination

The interesting parts of channels are rarely where things actually move in a straight line. Here, we have calculated the flow vectors near a partial obstruction (position indicated by blue circle) in a channel (Figures 3.14 and 3.15). The flow vectors follow the expected path around the obstruction to recombine downstream with flow moving faster at positions away from the obstruction than closer.

The accuracy for this method was probed by executing the analysis program on a series of simulated image stacks generated for a range of flow angles. In each case the flow angle about 49 points was measured and the results plotted in figure 3.16. The resulting fits yielded the expected flow angle with high accuracy and precision. A fit to a plot of measured angle *vs.* expected angle had a slope of 1.004 with R^2 of 0.9998. The largest standard deviation measured across the 49 points was 0.009753 radians. In addition, the measured flow speed was 0.4965 pixels per frame (representing an 0.7% error relative to the expected value of 0.5 pixels per frame) with a standard deviation of 0.0112 pixels per frame. The value for flow speed is especially relevant because this measurement contains the errors for both the angle and delay contained therein.

Demand for computational time is much higher for this method for two main reasons- 1: this algorithm involves taking typically 10-25 pairs of pixels at each center instead of a single cross-correlation in the above flow-aligned method; 2: each pixel pair requires two cross-correlations, not just one. Even with these additional needs the ability to measure flow vectors in a device without prior knowledge of the flow direction at a particular point in a channel is, in practice, more useful than measuring flows in a straight channel.

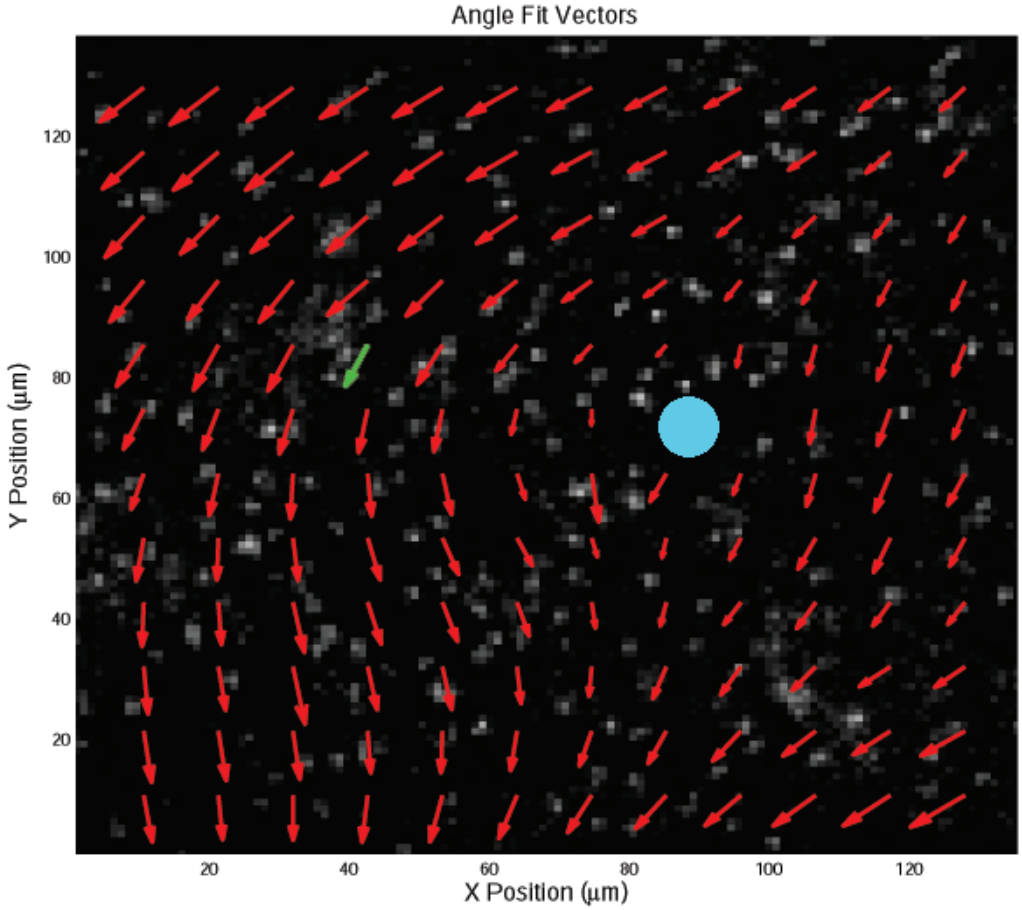

Figure 3.14: Flow vectors around a channel obstruction (blue circle). For reference, the green arrow indicates a flow at -2.01 radians relative to the x-axis and a speed of 287 μm/sec.

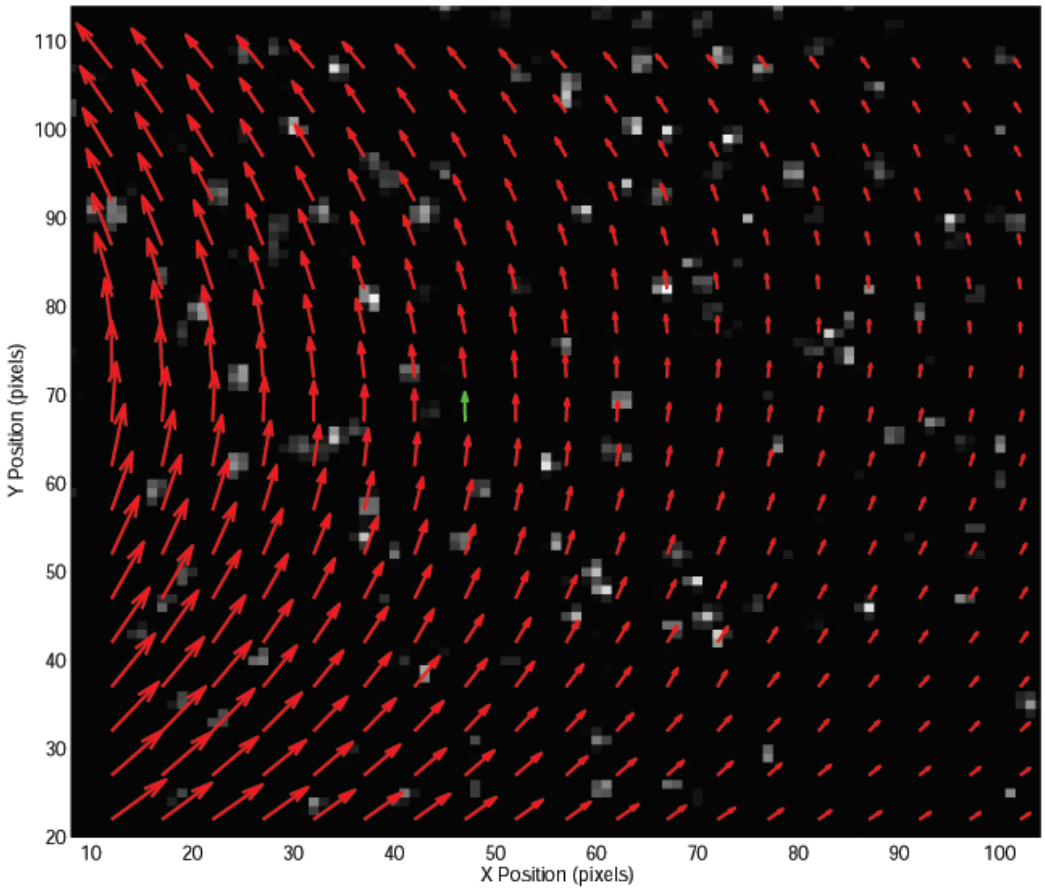

Figure 3.15: Flow vectors in and out of the imaging area. For reference, the green arrow indicates a flow at 1.576 radians relative to the x-axis and a speed of 80.9 μm/sec.

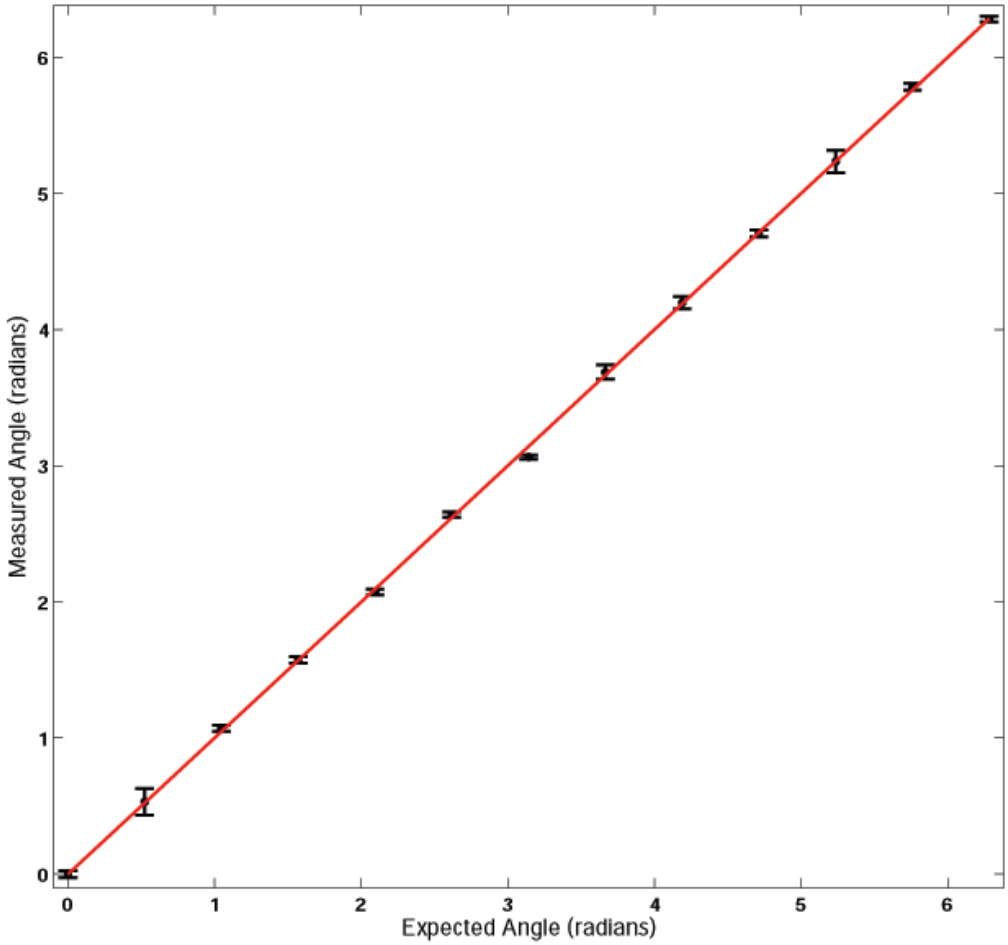

Figure 3.16: Measured angle (black squares) and standard deviation (error bars, 49 data points) for simulated flow measured with the presented in-plane angle fitting algorithm. The best-fit line (red) has slope, y-intercept, and R^2 values of 1.004, -0.004, and 0.9998, respectively (expected slope = 1).

3.4.4 Axial Flow Vector Mapping

While in most microfluidic channels the flow is strictly planar, there are many cases where the flow in the axial direction is significant. Especially for functional channels incorporating vortices and other features or analogs for three-dimensional devices such as filters or porous media the flow in and out of the focal plane is an important portion of the total flow profile. As a result any flow-mapping technique should incorporate a method for measuring these axial flow vectors.

Beginning with simulated data stacks with axial flows in the range of 0 to π radians, the axial flow vectors were measured. The results of these measurements appear in figures 3.17 through 3.19. Axial flow direction is best determined when the angle is away from flow angles approaching totally in-plane. In that case the fitting algorithm is essentially struggling to fit the peak of the amplitude map when the peak exists outside of the local cross-correlation amplitude map (see equation 30 and figure 3.17). This problem can be somewhat remedied by enlarging the generated correlation map surrounding each point, but with the resulting trade-off that the flow angle is averaged over this area. Alternatively the data can be taken for two focal planes that are closer together in axial position, yielding increased sensitivity for near-planar angles but decreased sensitivity for angles nearing purely axial.

The fits of planar flow angles are accurate for purely planar flow, as seen in figure 3.18 and previously in figure 3.16. As flow becomes more axial, however, the accuracy for planar angles decreases. This can be seen in the resulting correlation amplitude maps as a transition from a peaked ridge similar to that seen in figure 8(a) to a 2-D Gaussian peak for the case of purely axial flow. This Gaussian peak is symmetric with respect to rotation in the planar direction and as a result is difficult to detect a planar flow direction when the amplitude map has a large amount of this character. Even so, the contribution to the total flow vector from that in the planar direction in a case such as this is diminished and so a poor fit under these condtions is less

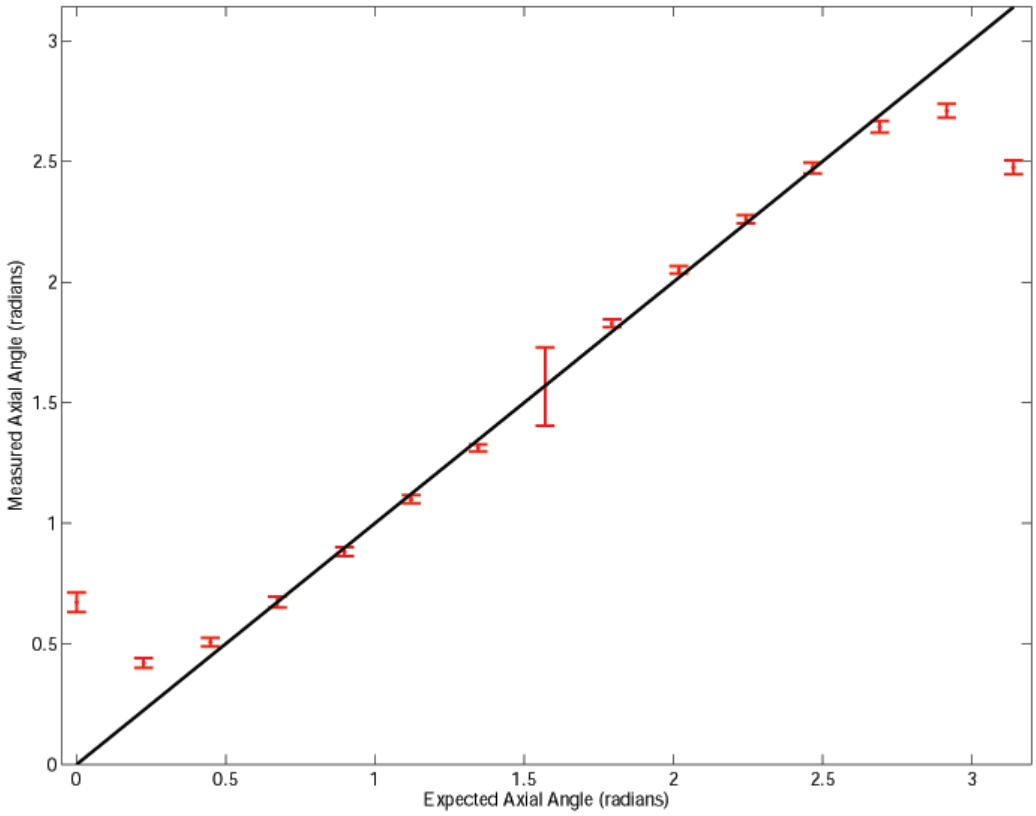

Figure 3.17: Measured axial angle (red) and standard deviation (error bars, 49 data points) for simulated axial flow measured with the presented axial angle fitting algorithm. The indicated line is at the expected value for a slope = 1. Measured flow angles for all but the most planar directions are close to the expected angle.

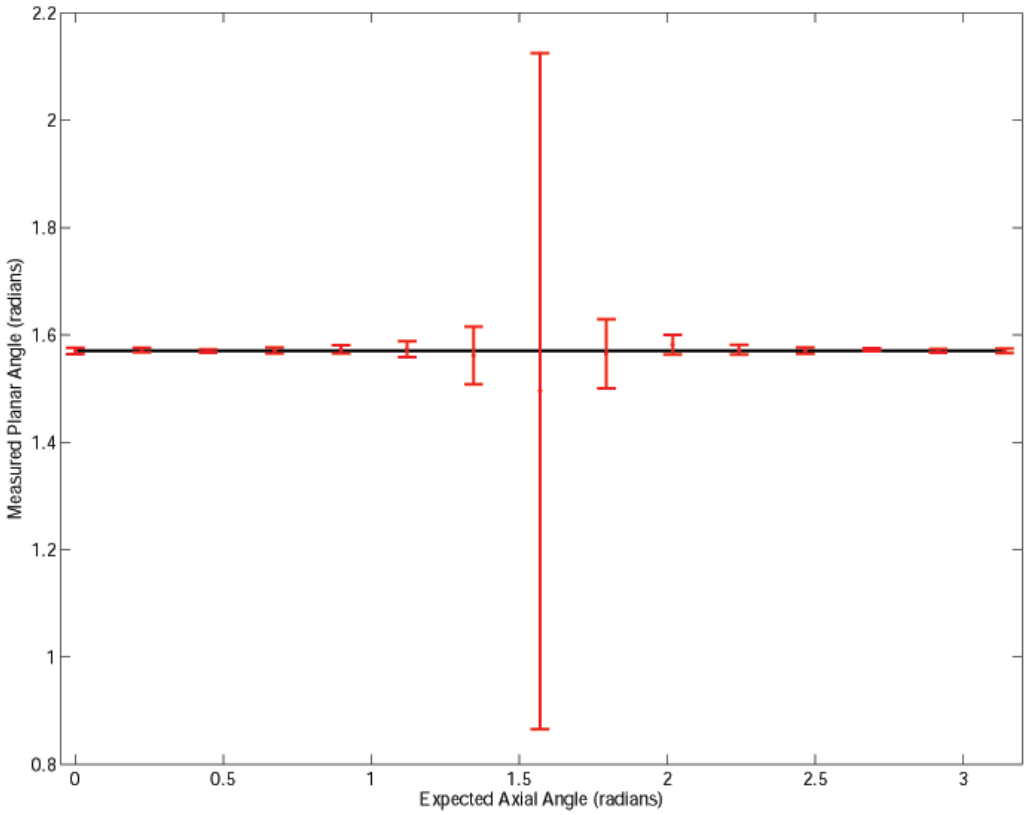

Figure 3.18: Measured planar angle (red) and standard deviation (error bars, 49 data points) for simulated axial flow measured with the presented axial angle fitting algorithm. The indicated line is at the expected value at $\pi\backslash 2$. Measured flow angles for all but the most axial direction are close to the expected angle.

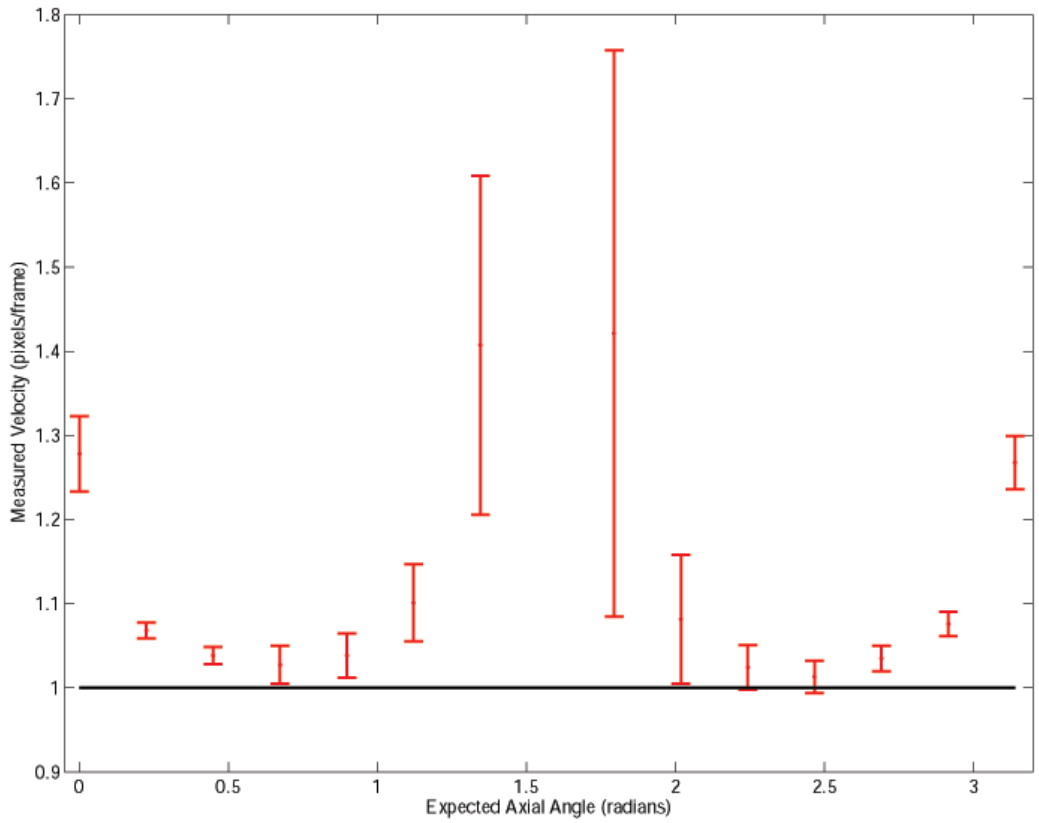

Figure 3.19: Measured total speed (red) and standard deviation (error bars, 49 data points) for simulated flow measured with the presented in-plane angle fitting algorithm. The indicated line is at the expected value at 1 pixel/frame. Measured speeds best fit the expected values for axial angles away from the most planar axial angles (0 or π radians) and the most axial ($\frac{\pi}{2}$ radians).

detrimental.

Because the flow speed, as determined by equation 31, contains the error in the measurement of both the axial and the planar flow angles, the fit to the expected value for the flow speed is best when the errors in those two measurements are diminished. As can be determined from the previous two graphs, the error in flow speed in axial flow directions approaching purely planar is due to errors in the axial flow angle measurement. The error in flow speed as the axial flow becomes more significant is due to the error in the planar flow angle measurement as the axial flow becomes more significant, but to one other additional factor. The speed is primarily determined by the delay fit for in-plane correlations (τ_{planar} in equation 31 from correlations ($H_1 : H_2, H_2 : H_1, L_1 : L_2$, and $L_2 : L_1$) in figure 3.7) and corrected for the axial and planar flow angles. Typically, when the correlation between the signals at two pixels is strong, the value for τ_{planar} is straightforward to accurately measure. However, for cases where the flow is strongly axial there are few pixels in a single plane that show strong correlations due to the small number of tracers that cross between both pixels. In addition time for this transit is very short in these cases, leading to further inaccuracy in the measurement of the flow delay. These shortcomings can be overcome somewhat by incorporating flow delays between focal planes in cases of strong axial flow, but even as the method stands the flow speed can be measured to within 10% of the actual flow speed across a large portion of the axial angles tested.

To demonstrate this technique in an experimental setup flow was measured through a channel designed to yield strong amounts of axial flow with the addition of shaped barriers at an angle to the flow direction. As the flow moves down and under the barrier the flow increases in speed and in axial displacement. A single region of interest of a channel appears in figures 3.20 through 3.25.

Figures 3.20 through 3.22 show a general flow direction through an arm of the channel with a significant axial contribution. This axial portion grows larger as the

flow approaches the barrier. The magnitude of this total flow and separate axial and planar contributions can be seen in figures 3.23, 3.24, and 3.25, respectively. The planar contribution largely matches the mean of the vector plot of the two individual focal planes, shown in figure 3.26. The vector projections overestimate the flow speeds relative to the in-plane fits, which is to be expected due to the additional error in the speed introduced with the incorporation of axial angle.

3.4.5 Experimental Limitations

The eventual goal of the cross-correlation technique presented here would be to allow for flow mapping in microfluidics with single dye molecules as probes. A crucial step in that goal, the increased noise tolerance, has been presented. This demonstrates a capacity for dimmer probes, which smaller probes will be more often than not. Data presented for flow mapping with single antibodies containing 5-7 organic dyes has shown that a particle containing a small number of organic dyes can be used as tracers. However, dividing the apparent intensity of a dye-labelled antibody in figure 13(a) by the expected 5-7 dye molecules would place the already small signal from these probes well into the dark counts of the CCD detector (apparent at the edges of figure 13(a)).

These low count rates are largely limited by the small transmission of emission through the pinhole array contained in the confocal scanning unit. At any instant a diminutive percentage of the focal plane is illuminated and transmissive to emission. There do exist other confocal scanning instruments with larger light throughputs that improve this limitation. In addition, it is possible to perform the same cross-correlation analysis on data collected in other geometries. The confocal scanning unit allows for a narrow axial slice of the entire focal volume to be imaged at one time, but other techniques exist to accomplish the same result. If the region of interest is located strictly at the surface then total internal reflection (TIR) microscopy can be utilized. For regions farther away from a TIR interface, planar excitation as is commonly used in PIV techniques would be effective to limit the emission away from the desired focal plane. In fact a PIV setup capable of high sustained frame rates would be easily adapted to produce flow maps through the cross-correlation technique.

While the low count rates from small tracers can be overcome with better imaging that is not the only issue regarding the use of these probes for flow mapping. The diffusion constant of the tracer decreases with the radius of the tracer particle, obscuring

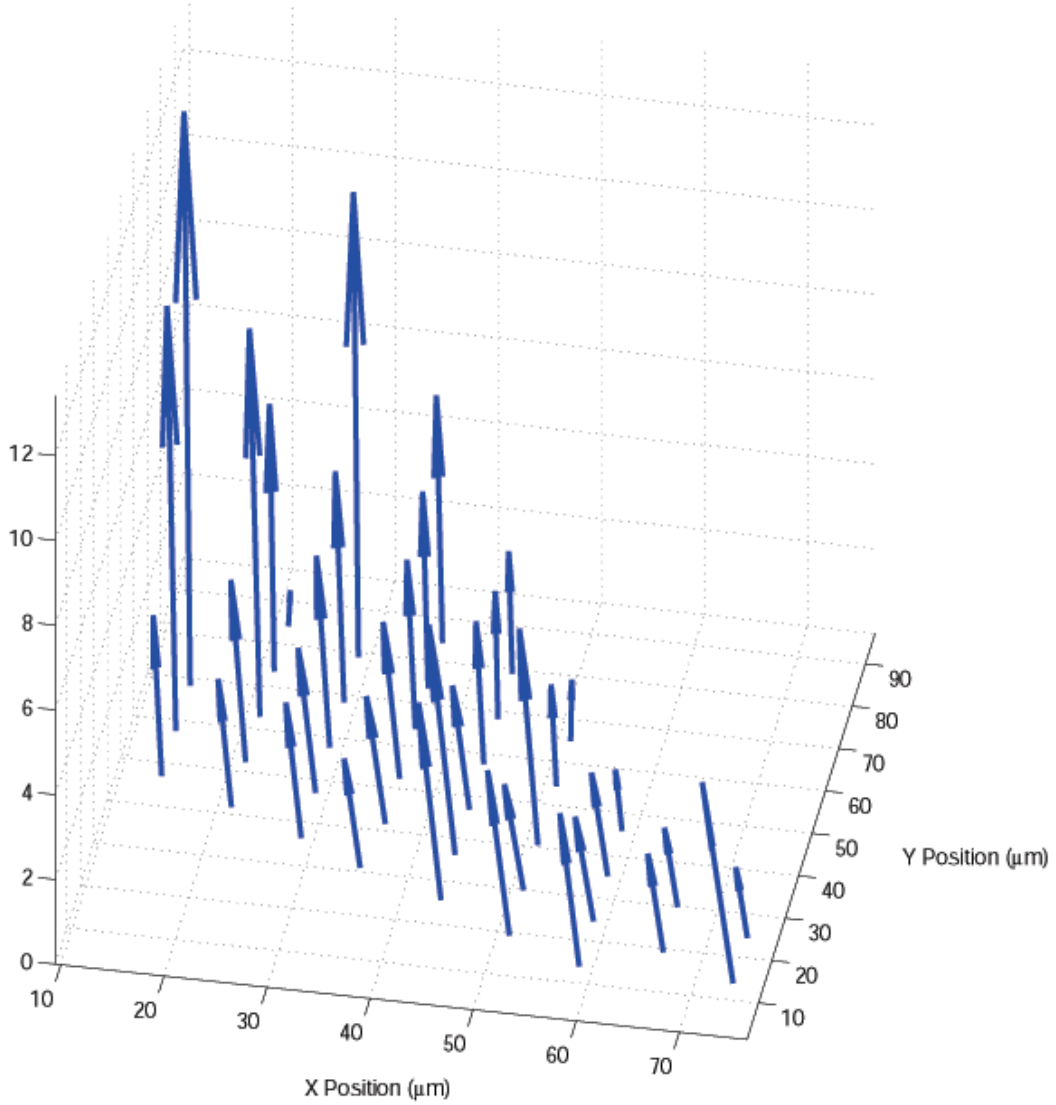

Figure 3.20: Measured flow vectors in a microfluidic device with a large axial flow contribution. The coordinates correspond to those pictured in figure 3.23 through 3.25. View 1 of 3.

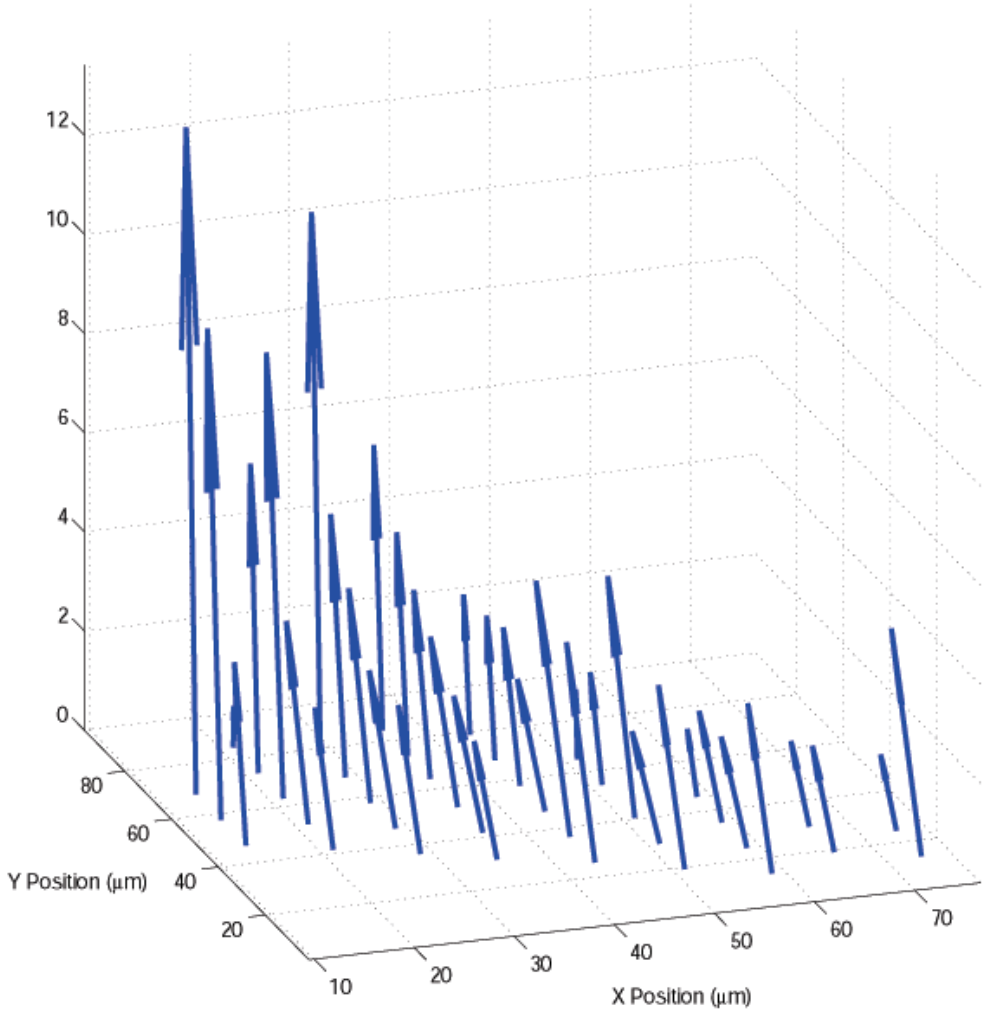

Figure 3.21: Measured flow vectors in a microfluidic device with a large axial flow contribution. The coordinates correspond to those pictured in figure 3.23 through 3.25. View 2 of 3.

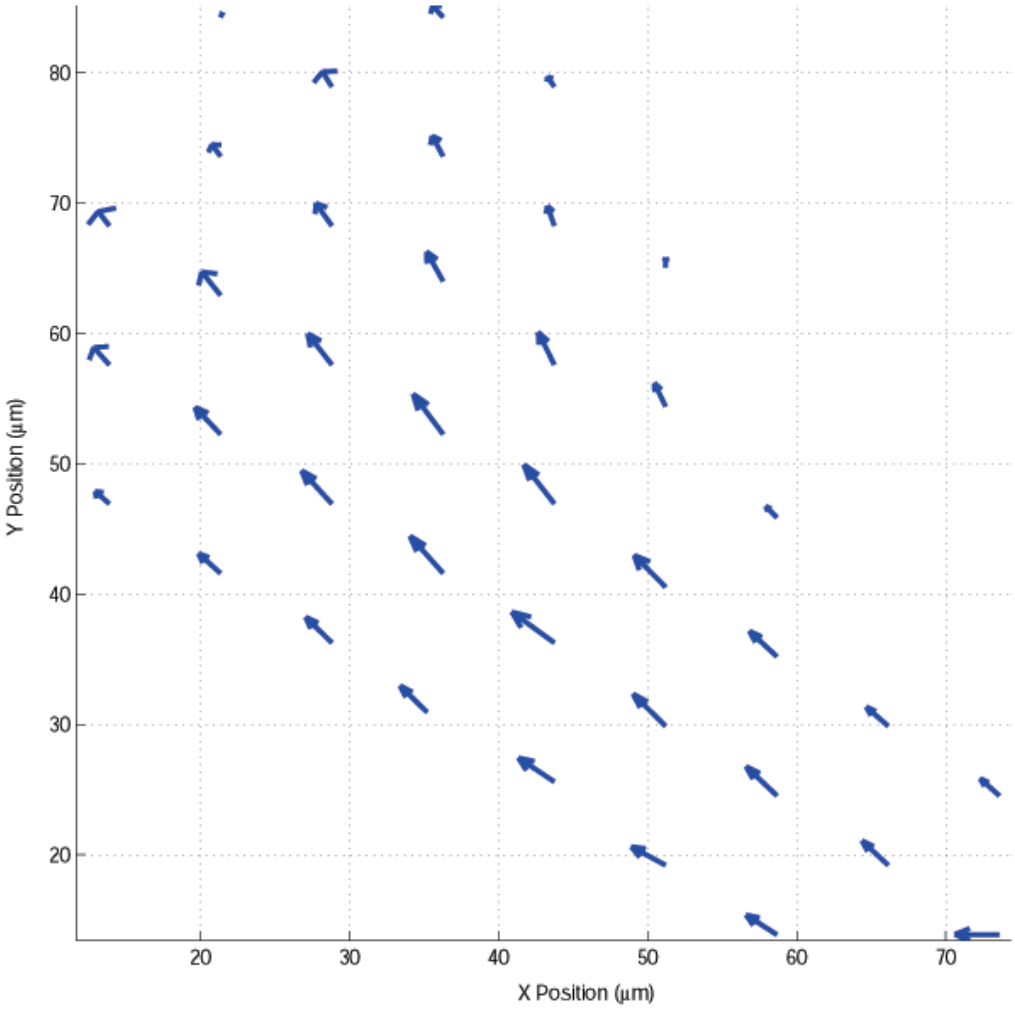

Figure 3.22: Measured flow vectors in a microfluidic device with a large axial flow contribution. The coordinates correspond to those pictured in figure 3.23 through 3.25. View 3 of 3.

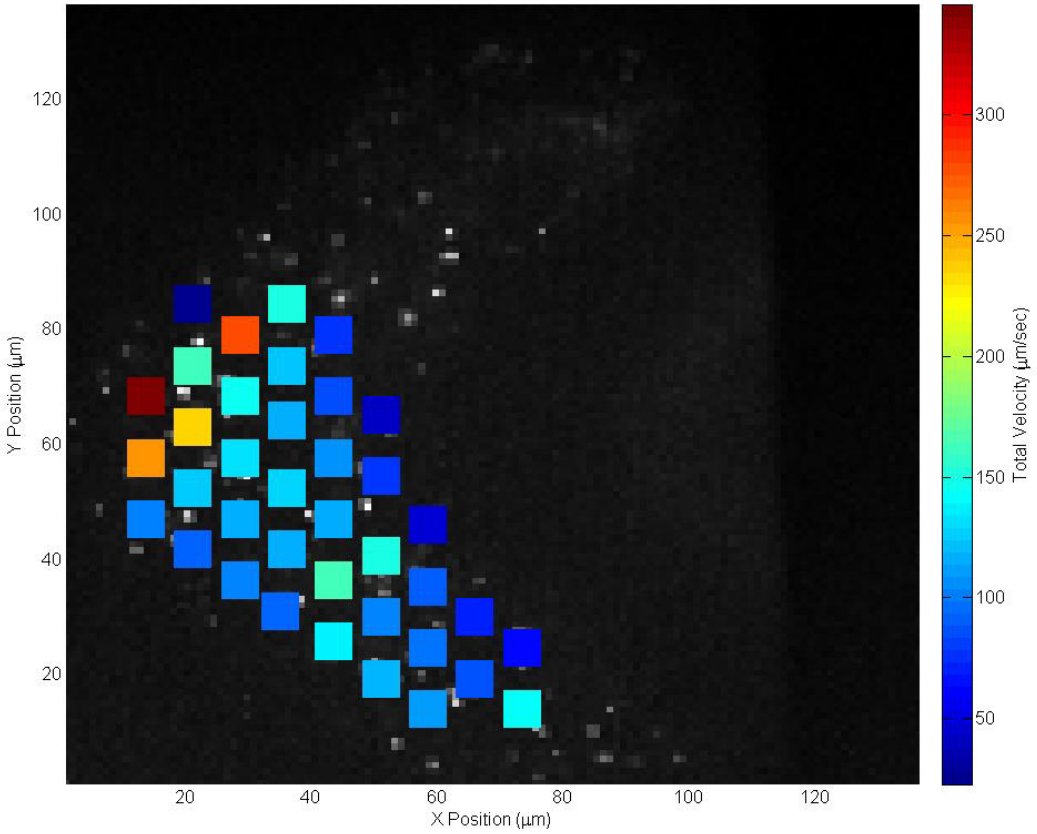

Figure 3.23: Measured total flow speeds in a microfluidic device with a large axial flow contribution. The coordinates correspond to those pictured in figure 3.20 through 3.22.

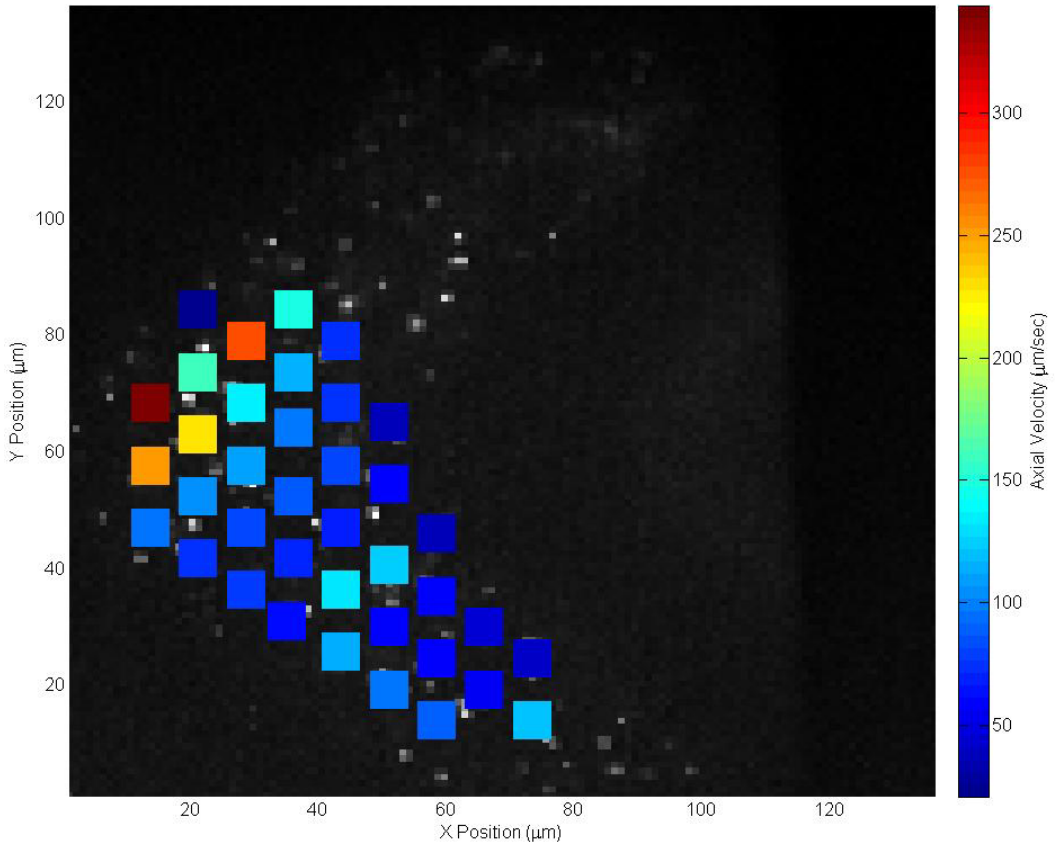

Figure 3.24: Measured axial flow speeds in a microfluidic device with a large axial flow contribution. The coordinates correspond to those pictured in figure 3.20 through 3.22.

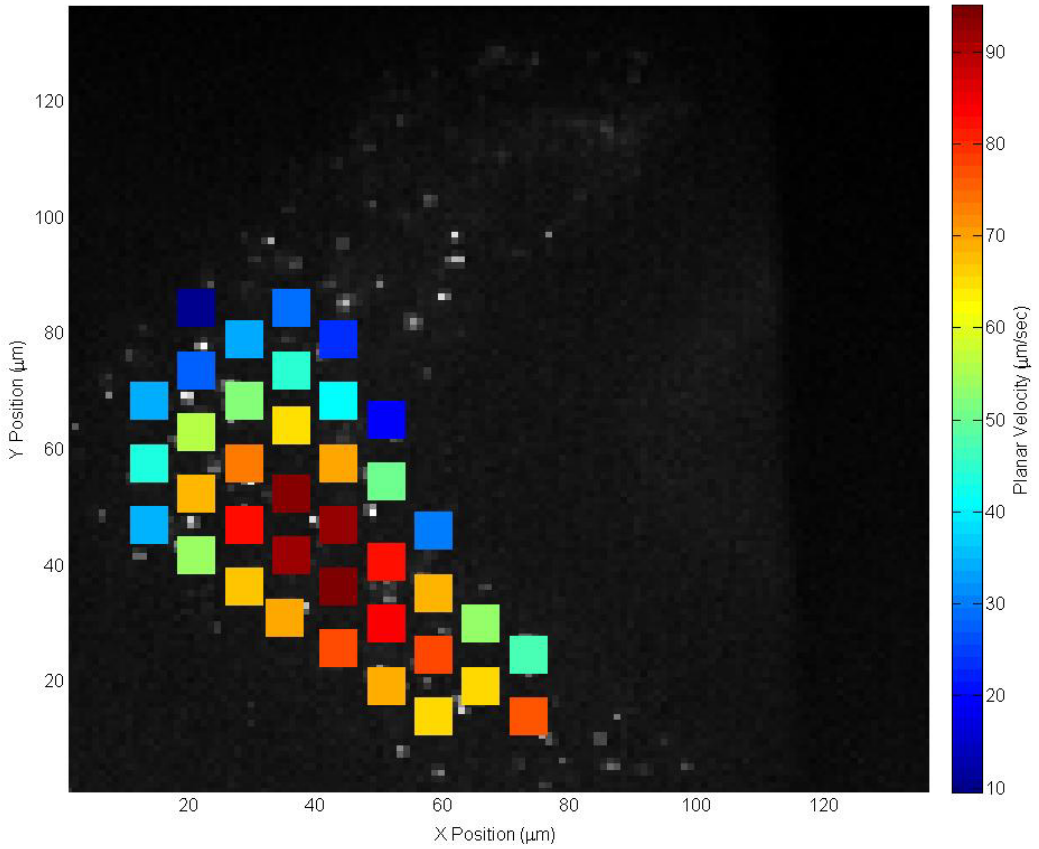

Figure 3.25: Measured planar flow speeds in a microfluidic device with a large axial flow contribution. The coordinates correspond to those pictured in figure 3.20 through 3.22. Compare to the results in figure 3.26.

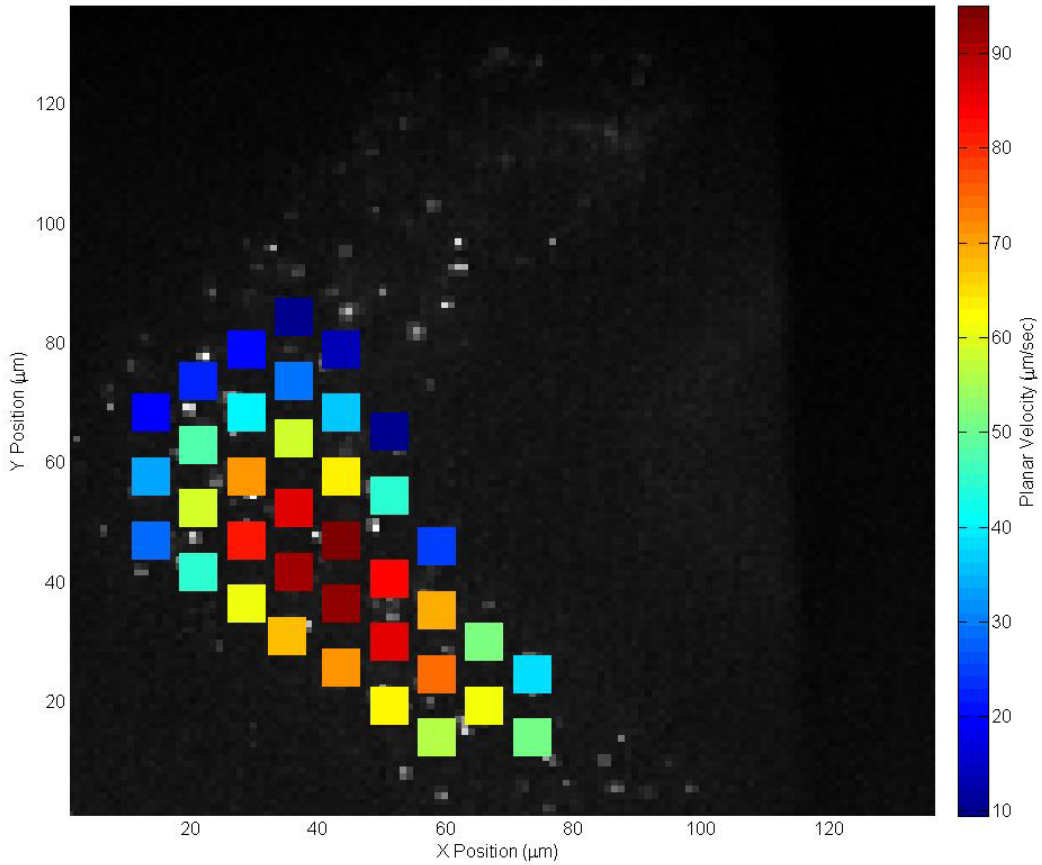

Figure 3.26: Mean planar velocity as determined by averaging in-plane flow speeds of the two individual focal planes in used to generate figures 3.20 through 3.25 This plot matches well with the planar flow projection appearing in figure 3.25.

the motion due to flow with the particle diffusion. The diffusion is random and so the average motion due to Brownian motion averages to zero, but a large amount of diffusion greatly decreases the chances of a particle transiting from one focal volume to the next without exiting the focal plane. Data showing the capacity to measure flow speeds as a function of particle size appear in figures 3.27 through 3.30. These results indicate that the length of the spacing vector chosen for flow mapping has little bearing on the eventual results outside of the case of very large diffusion. Deviation from the slope = 1 line at high flow speeds indicates a situation where the particles exit the image region too quickly to be effectively measured. This final problem can be somewhat mediated for very rapidly moving particles by using a very long imaging area in the flow direction and a correspondingly long spacing vector.

As can be seen in figures 3.27 through 3.30, is it difficult to accurately map the flow of particles when the flow rate is smaller than the average diffusion. An expression for this value, D_{RMS}, appears in equation 36.

$$D_{RMS} = \frac{k_B\, T}{\pi\, \eta\, R_h\, F\, P_D^2} \tag{36}$$

Here, k_B is the Boltzmann constant ($1.3806503 * 10^{-23} m^2\, kg\, s^{-2}\, K^{-1}$), T the temperature in Kelvin, η the viscosity of the solvent ($8.94 * 10^{-4} N\, m^{-2}\, s$ for water at 298 K), R_h the radius of the particle (m), F the frame rate (Hz), and P_D the pixel dimensions (m). The resulting value for D_{RMS} is in units of pixels per frame. In order to decrease the diffusion the easiest variable to control experimentally is the viscosity. As such, to yield acceptable flow maps for tracers the size of individual antibodies ($r_h = 15$ nm) the viscosity was increased by using 10% PEG 8000 solution ($\eta = 8.9 * 10^{-3} N\, m^{-2}\, s$, [198])in the place of water for the solvent. Under similar experimental conditions (1 μm x 1 μm pixels, 100 Hz frame rates, ambient conditions) with tracers 1 nm in diameter and 100 μm per second flow it would require a viscosity of $1.3 * 10^{-2} N\, m^{-2}\, s$, comparable to a solution of approximately 15% PEG 8000.

However, in order to map the flow near the walls of a channel the flow rates would approach zero. In the same situation, assuming a flow rate as low 1 μm per second this would require a solvent viscosity two orders of magnitude higher ($1.3 * N\, m^{-2}\, s$) corresponding to over 50% PEG 8000. This solution is possible to drive through a microfluidic channel but difficult to control precisely.

As demonstrated in figure 3.29 and 3.30 it is quite straightforward to measure flow speeds over 10 pixels per frame. Under the conditions tested this corresponds to particle speeds of 1 mm per second. The confocal scanning unit has a maximum frame rate of 360 frames per second, but a frame-transfer EMCCD such as the one used here is capable of acquisition rates of over 1000 frames per second. Ignoring the limitation of the confocal scanner, this pushes the maximum flow rate measurable by this method to 10 mm/sec. It is possible to further improve this flow speed at the cost of spatial resolution by increasing the pixel size.

In order to acquire reliable data for the in-plane and axial angle fitting algorithms it is necessary that the particles not leave the sub-imaging area (typically a 21 pixel x 21 pixel area) before yielding correlations across several pixels. Because of this constraint the best results anecdotally come from data with flow rates between 0.5 and 5 pixels/frame in the focal plane. With the typical experimental dimensions mentioned above this corresponds to flows of approximately 50 to 500 μm per second. In addition, a similar constraint on the flow speed is necessary in the axial direction. Exacerbating this issue is the limited focal plane switching rates attributed to the piezo nosepiece. The absolute speed is dependent on flow angle, but for the worst case of purely axial flow and focal plane spacing of 4 μm this corresponds to an axial flow rate of 266 μm/sec. In practice slower flow speeds are easier to measure correctly.

The motion of the piezo nosepiece imparts an important uncertainty the axial flow measurements. As mentioned, the maximum speed of the nosepiece used in these experiments is near the 33 Hz used in these experiments. A single cycle of the nosepiece

yields a pair of images (one for each focal plane). Rapidly changing the voltage applied to the piezoelectric material caused ringing of the nosepiece and so the driving function was not a true square wave with steps of infinite slope. Instead the travel time between the two voltage values was 3.0 ms with 12.0 ms at a constant voltage. The CCD had only 160 μsec between frames and the acquisition was aligned in phase to the motion of the nosepeice as best as possible. Under ideal phase alignment, 19% of each frame acquisiton represents time that the nosepeice is in motion. The ability to control the dead time of the CCD or a piezo nosepiece capable of more rapid repositioning would allow this error to be avoided. Even so, the axial flow measurements represent an average between the two focal planes and a small amount of uncertainty in the position between the two focal planes should not have a detrimental effect on the accuracy of these measurements.

Cross-correlation time series analysis is, at its core, an average over the measurement window. For systems where dynamic information at timescales between the acquisition rate (tens of ms) and the experimental duration (seconds) is paramount, the cross-correlation analysis is at a disadvantage relative to particle tracking algorithms. However, in steady-state systems where the average value over the experimental timeframe is acceptable, cross-correlations allow for an important improvement in noise tolerance over particle tracking. In a particle tracking experiment the correction to overcome a high-noise environment is to increase the exposure time for image acquisition, which can lead to uncertainty in the particle position due to motion blurring. On the other hand, the same correction for the cross-correlation method presented here is to extend the data set. There exists a trade-off between uncertainty in particle positions (and therefore speeds) and time-averaging between particle tracking and cross-correlation time series analysis.

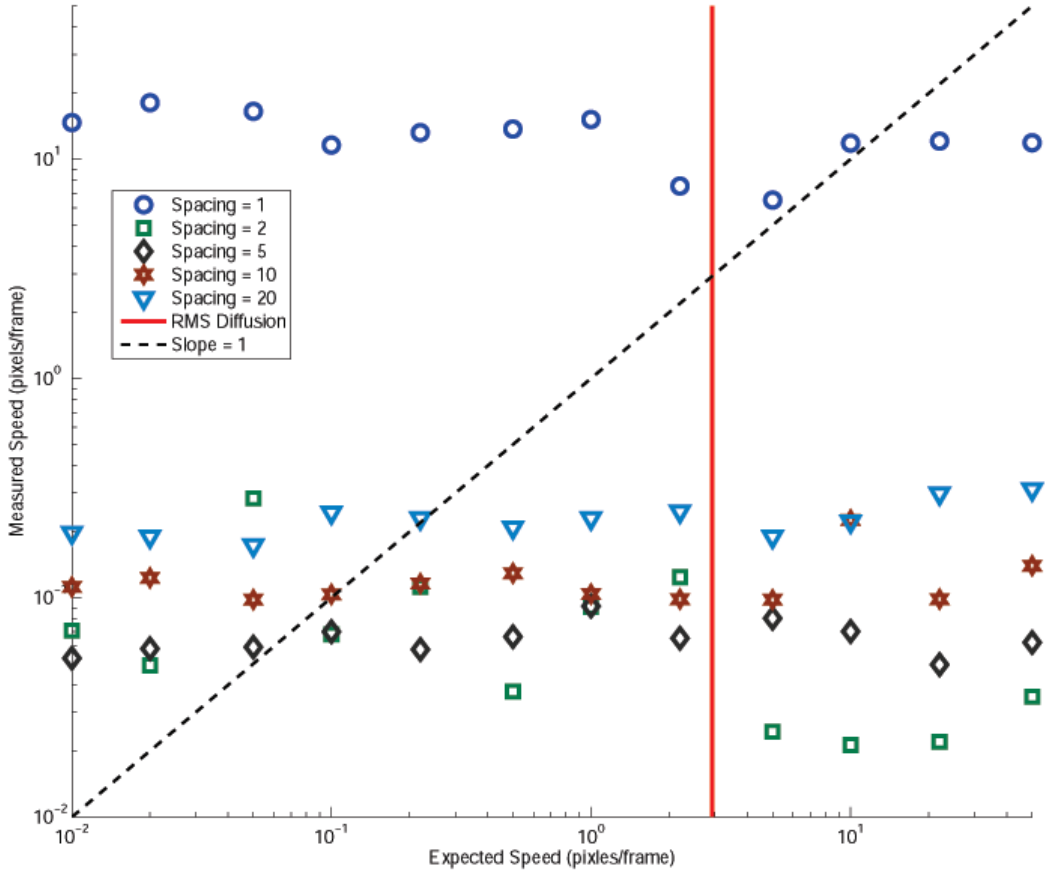

Figure 3.27: Measured flow speeds in simulated data for particle diameters of 10 nm with varying flow speed and spacing length. In each case a typical experimental setup with pixels 1 μm on a side in the image space, 100 Hz frame rates, and water as the solvent was used. Red line indicates the average diffusion per time step in the simulation and the dashed black line the expected results.

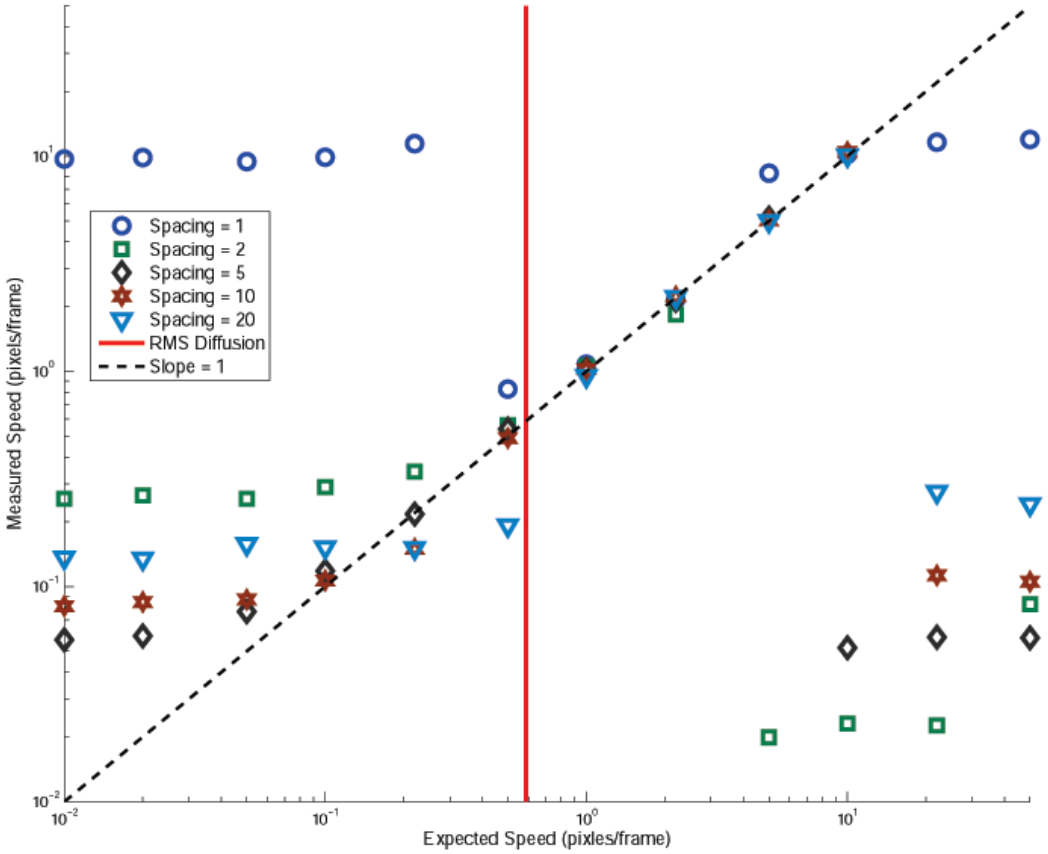

Figure 3.28: Measured flow speeds in simulated data for particle diameters of 50 nm with varying flow speed and spacing length. In each case a typical experimental setup with pixels 1 μm on a side in the image space, 100 Hz frame rates, and water as the solvent was used. Red line indicates the average diffusion per time step in the simulation and the dashed black line the expected results.

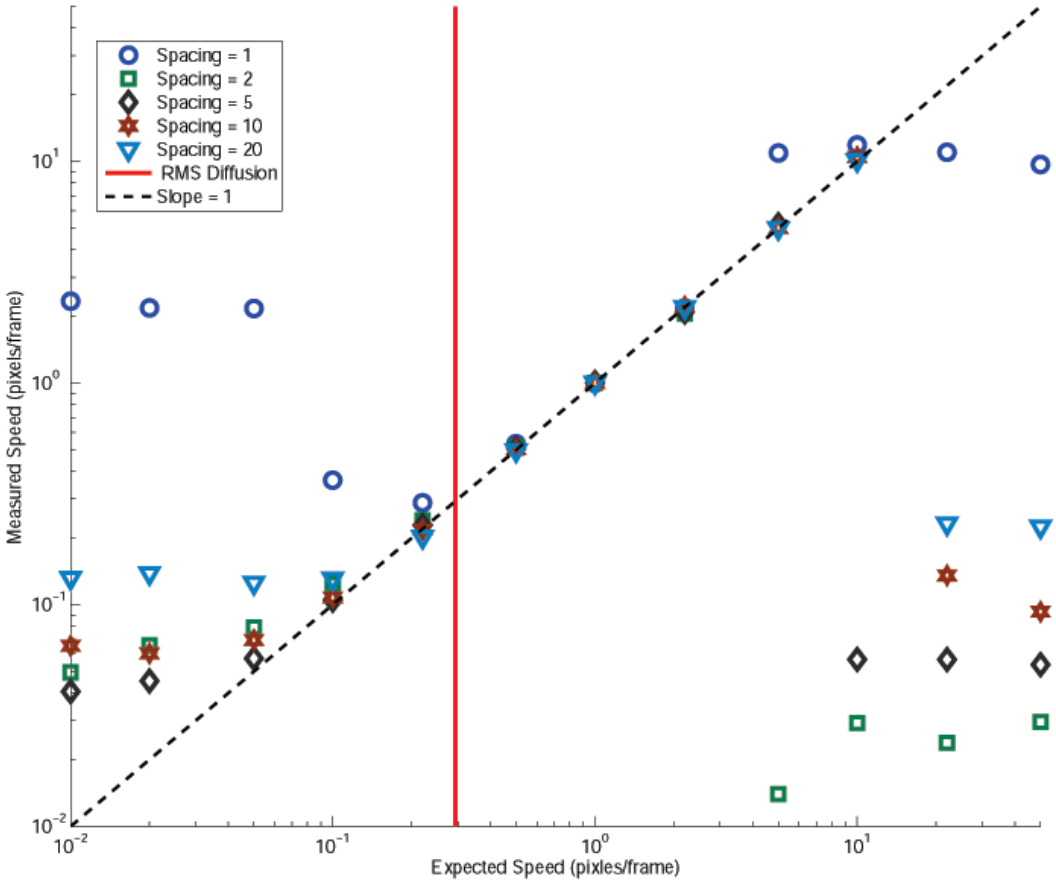

Figure 3.29: Measured flow speeds in simulated data for particle diameters of 100 nm with varying flow speed and spacing length. In each case a typical experimental setup with pixels 1 μm on a side in the image space, 100 Hz frame rates, and water as the solvent was used. Red line indicates the average diffusion per time step in the simulation and the dashed black line the expected results.

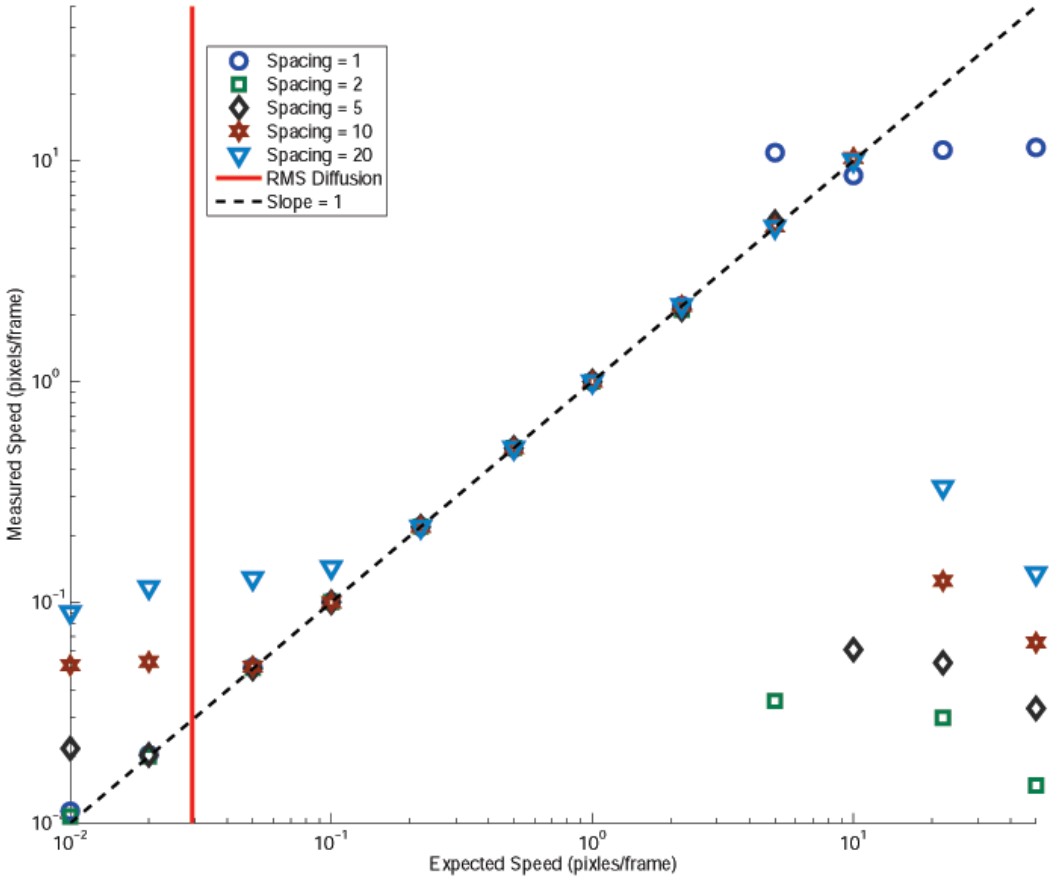

Figure 3.30: Measured flow speeds in simulated data for particle diameters of 1000 nm with varying flow speed and spacing length. In each case a typical experimental setup with pixels 1 μm on a side in the image space, 100 Hz frame rates, and water as the solvent was used. Red line indicates the average diffusion per time step in the simulation and the dashed black line the expected results.

3.5 Conclusions

Presented here is a novel method for determining flow vectors through pixel-pair cross-correlation analysis. In conjunction with a Nipkow disk confocal scanner, 3-D flow maps in a microfluidic device were determined as well as flow vectors in an area with inhomogeneous flow vectors. This method has also demonstrated a large tolerance for noise and low fluorescence intensity from the tracer particles. Because of the generality of the algorithm put forth here, the use of this method on systems other than microfluidic devices should be straightforward. In addition, cross-correlations are not limited to flow phenomena. By fitting the cross-correlation to other models (diffusion, hindered diffusion, etc.) this method can be applied to a large number of other systems. With the use of brighter dyes and appropriate experimental conditions, this method could well be applicable to measuring flow rates over large fields of view in three dimensions with single organic dyes as tracer particles.

CHAPTER IV

ADVANCED WIDEFIELD CONFOCAL MICROSCOPY - SIGNAL EXTRACTION AND SUPER-RESOLUTION IMAGING

4.1 Introduction

While previously presented work in this thesis has focused on using widefield confocal microscopy as a tool for mapping microfluidic flow, the generality of the data collection process allows for straightforward adaptation of many other analysis methods to work in conjunction with or addition to the previously reported methods. These methods all share a common foundation - data is collected as a time series of images which yield intensity *vs.* time traces at each pixel. The analysis of these traces are what define the different techniques. Here we report two additional techniques which result from alternative methods of analysis. The first relies on the phenomenon of dynamic fluorescence enhancement due to dark state depletion by a secondary laser, resulting in increased sensitivity for modulatable probes. The second utilizes higher-order statistics in conjunction with stochastic blinking processes to generate super-resolution images from a typical single-point confocal microscope.

4.2 Fluorescence Modulation Signal Extraction

4.2.1 Introduction

A constant challenge with fluorescence microscopy is isolating those fluorophores of interest above the background. This problem is made more difficult when imaging in complex media, such as living tissues, which themselves will fluoresce under visible or near-UV excitation. While increasing the number of the fluorophores of interest will

increase signal above the background, often these fluorophores exist in very low copy numbers and retaining the information in the heterogeneity of the probes is desired. In addition an increase in the single-molecule brightness of the fluorophores of interest will yield a greater signal, but this is a difficult problem that many groups continue to work towards.

An intriguing solution to the problem of signal sensitivity has been developed by members of this group [165]. It has been shown that increasing the excitation intensity increases the return of some molecules, namely DNA-templated silver clusters, from the dark state back to the emissive state [155]. This transition has been further characterized, confirming a transient absorption in the near-IR on the microsecond timescale for these molecules [164]. Excitation of this transient dark state with secondary irradiation pumps the electron back into the singlet (emissive) manifold, resulting in a decrease in the dark state lifetime and increased emission rates [165]. This secondary illumination is of a longer wavelength than the fluorescence, in contrast to similar techniques that use two coaligned lasers of higher energy than the fluorescence [178, 180].

The increase in sensitivity towards desired probes over the background is accomplished through lock-in detection. The signal of interest is modulated at a known frequency and detection is tuned to amplify signal carrying this specific frequency. Given time series data $f(t)$, the intensities at a range of frequencies $F(\nu)$, known as the power spectrum, can be determined through the Fourier transform (equation 37).

$$F(\nu) = \int_{-\infty}^{\infty} f(t) e^{2\pi i \nu t} dt \tag{37}$$

By mapping the power at the desired modulation frequency as a function of spatial position an image can be produced that extracts signals from only those emitters that undergo fluorescence modulation.

The range of probes that can be modulated is a small subset of the large number of emissive molecules. DNA:Ag nanodots are particularly adept at this process [165]. Other common fluorophores will also undergo this process, but at much higher secondary laser illuminations [44]. Common organic fluorophores investigated by Ringemann, *et. al.* had typically high emission quantum yields which limited the amount of fluorescence enhancement that could be achieved. The opposite approach proved more useful, using organic dyes with high triplet quantum yields and using secondary illumination to deplete the triplet state and enhance fluorescence from the singlet state [199]. While DNA:Ag nanodots show more enhancement, in addition to the other useful photophysical characteristics, triplet-sensitized organic dyes are much more amenable to chemical modification and thus are used in this work.

This fluorescence enhancement can be accomplished on rapid time scales, here extended to produce video-rate CCD data and kHz-rate single-point TCSPC data. For experiments presented, Rose Bengal was used as the modulatable fluorescence probe. This dye typically shows low fluorescence yield due to the high triplet quantum yield, which allows for a large amount of fluorescence modulation. The low fluorescence yield was overcome by coating large numbers of these dyes onto polystyrene beads to increase the local concentration of dye.

4.2.2 Methods

4.2.2.1 Dual Laser Experimental Setup

The experimental schemes for dual-laser experiments are detailed elsewhere (see chapter 2.8). For widefield measurements, primary illumination was achieved through a Yokogawa CSU 10 confocal scanning unit (Figure 2.5) and the secondary laser was aligned onto a dichroic mirror in the microscope turret. Emission was passed through a band-pass filter before continuing back through the confocal scanning unit and to the CCD detector. In the single-point case two laser beams were combined on a dichroic mirror external to the microscope and then focused as a single laser beam

(Figure 2.4). Emission was passed through the dichroic mirror and a band-pass filter before continuing on to an optical fiber and APD.

For CCD-based data, subsequent frames were collected at high frame rates (typically 50 Hz) with modulation of the secondary laser at approximately 25 Hz by a chopper. These movies were converted to intensity *vs.* time traces at each pixel and processed wtih custom-written MATLAB scripts. The power at the peak modulation frequency was mapped back onto the spatial position of the pixel to generate the extracted images.

Single-point dual-laser data was collected with a TSCPC module. Modulation was accomplished by passing polarized secondary illumination though an acousto-optic modulator driven by an programmable function generator. This allowed the modulation frequency to be tuned to any desired frequency. Typically 1-10 kHz modulation frequencies were used. Analysis was again performed with custom-written MATLAB code.

For data presented here all beads were spin-cast in 5% PVA (poly(vinyl alcohol)) onto standard glass coverslips.

4.2.2.2 Synthesis of Rose Bengal-functionalized Beads

Functionalized beads were synthesized through a modification of established methods. A synthesis schematic appears in Figure 4.1. The free carboxylate on Rose Bengal was transformed into the hexanoic acid ester(**1**) by refluxing free Rose Bengal and 6-bromohexanoic acid (1:2 molar ratio) in 70% Acetone for 18 hrs [200]. The reaction mixture was acidified with 5% aqueous H_2SO_4 and then extracted with chloroform. The chloroform extract was evaporated to dryness and final purification was done by column chromatography (80:20:1 to 50:50:2 Hexanes:Ethyl Acetate:Acetic Acid).

This product was transformed to the *N*-Hydroxysuccinimide ester by co-dissolving **1** with *N*-hydroxsuccinimide (1:2 molar ratio) in dimethylformamide (DMF). Two

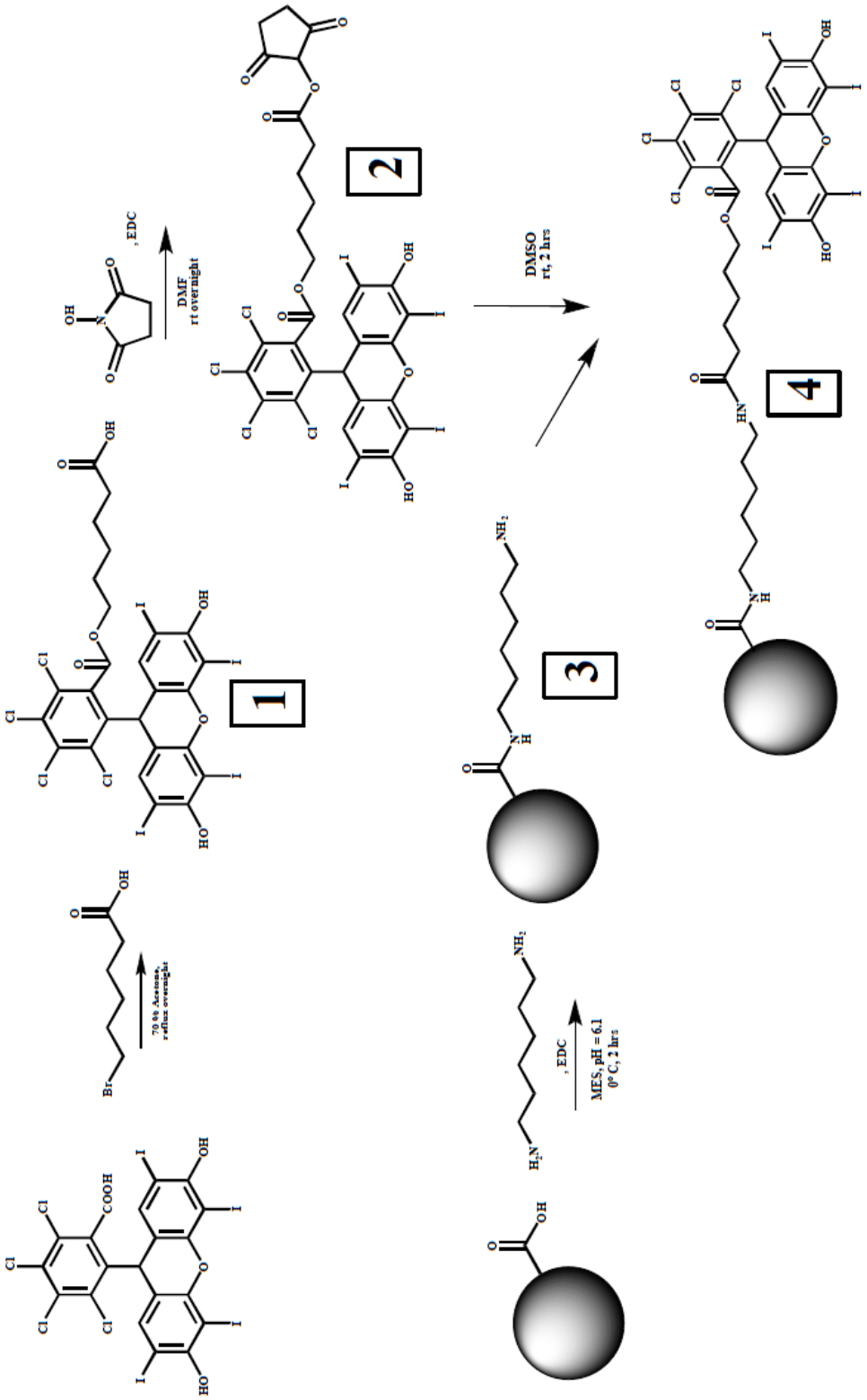

Figure 4.1: Schematic of synthesis of Rose Bengal-functionalized polystyrene beads.

equivalents of EDC (1-ethyl-3-(dimethylaminopropyl)carbodiimide) were added and stirred overnight. The DMF was removed *in vacuo*. The residue was dissolved in chloroform and washed with deionized water, 1 M NaOH, and brine. The organic layer was dried, filtered, and concentrated by approximately half before triturating with diethyl ether, producing a precipitate **2** [201].

Amine-functionalized beads **3** were synthesized in a similar manner as the amine linkage forming **2**. Into MES (2-(*N*-morpholino)ethanesulfonic acid) buffer (50 mM, pH = 6.1) was dissolved 1,6-diaminohexane to yield a final concentration of 10 mM at 0 °C. Carboxylate-modified beads were dissolved to give a concentration of 25 mg/mL and EDC added to final concentration of 12 mg/mL. After 2.5 hours stirring the beads were recovered by dialyzing against 0.1 M NaCl (100-500 MWCO membranes, 3x changes over 24 hrs), yielding **3** [202].

The final Rose Bengal-functionalized beads **4** were formed by codissolving **2** and **3** in dimethyl sulfoxide (DMSO) for 2 hours in a round-bottom flask in a sonicator. The product was isolated by centrifigation with multiple rounds of washing [203]. Characterization was perfomed through dynamic light scattering (DLS) and fluorescence correlation spectroscopy (FCS).

4.2.3 Results and Discussion

Characterization by DLS and FCS indicated that Rose Bengal beads aggregated and possibly cross-linked during the synthesis procedure. The beads were of 70 nm nominal diameter. Experiments run after functionalization indicated a diameter of 180 nm and 300 nm by DLS and FCS, respectively. While ideally the diameter should not change a significant amount through the functionalization procedure, the actual diameter of these particles was not of great consequence to the subsequent experiments.

Widefield modulation of the Rose Bengal beads was accomplished in the confocal

scanning setup. As can be seen in figures 4.2 and 4.3 and subfigures, the constant background obscuring the modulated bead is suppressed by the modulation extraction procedure. This same procedure can be accomplished in a binned manner such that subsets of frames were combined to produce a single extracted frame, resulting in dynamic information up to approximately one-tenth the maximum frame rate of the CCD, easily approaching video-rate data.

Because this procedure takes image stacks as both input and output, the type of data is largely insensitive to the details of the experiment. In addition, there exists the power to couple this method with particle tracking, widefield cross-correlation microscopy, or other image analysis procedures to output results with greater sensitivity to the probe of interest. This is especially important in biological samples that have large amounts of non-modulatable background.

Single-point modulation measurements allowed the modulation rate to increase from the 10 to 100 Hz possible with CCD imaging to 10 kHz. Fourier tranforms of TCSPC time traces of spin-cast Rose Bengal beads modulated at various frequencies appear in figure 4.4. The data from these modulated time traces can be selectively amplified at times during secondary illumination and attenuated for times under only primary illumination, resulting in a lock-in amplifier operating at rapid timescales. Amplified data can then be binned and longer timescale processes for modulated fluorophores selectively investigated.

To illustrate this procedure, consider a system containing both modulatable and unmodulatable fluorophores in solution. If the sizes, and therefore diffusion timescales of the two fluorophores are similar and there exists a large amount of spectral overlap, neither the fluorescence correlation characteristics nor the spectral differences can be used to separate information from these two molecules. In a biological system the native non-modulatable fluorophores would be at a higher concentration, obscuring the signal and fluctuations due to the modulatable fluorophore of interest. With the

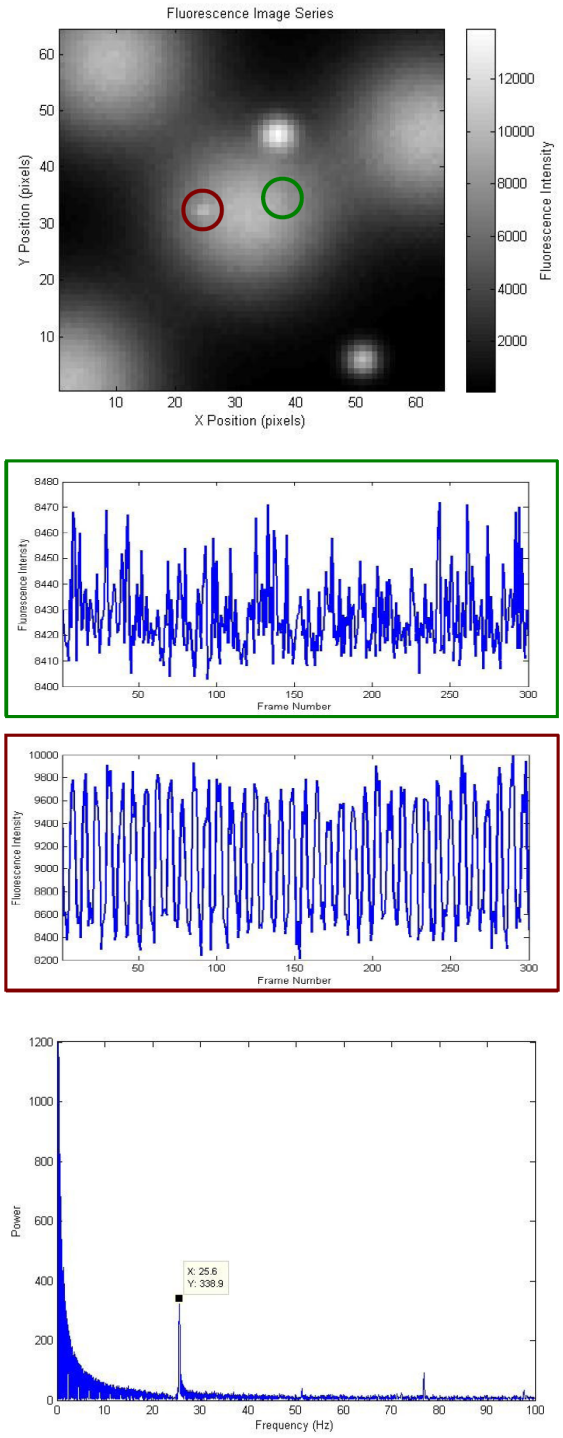

Figure 4.2: Widefield Fluorescence Modulation Signal Extraction: 2(a) Composite experimental and simulated fluorescence image. Modulation data was experimentally collected and later added to large constant background; 2(b) Intensity *vs.* time traces for pixels chosen in 2(a). Modulation is apparent in red (top) trace, taken near the secondary laser, but not in bottom (green) trace, taken away from the secondary laser; 2(c) Resulting Fourier Transform of the time trace from 2(b) showing peak at modulation frequency of 25.6 Hz. The resulting image appears in figure 4.3

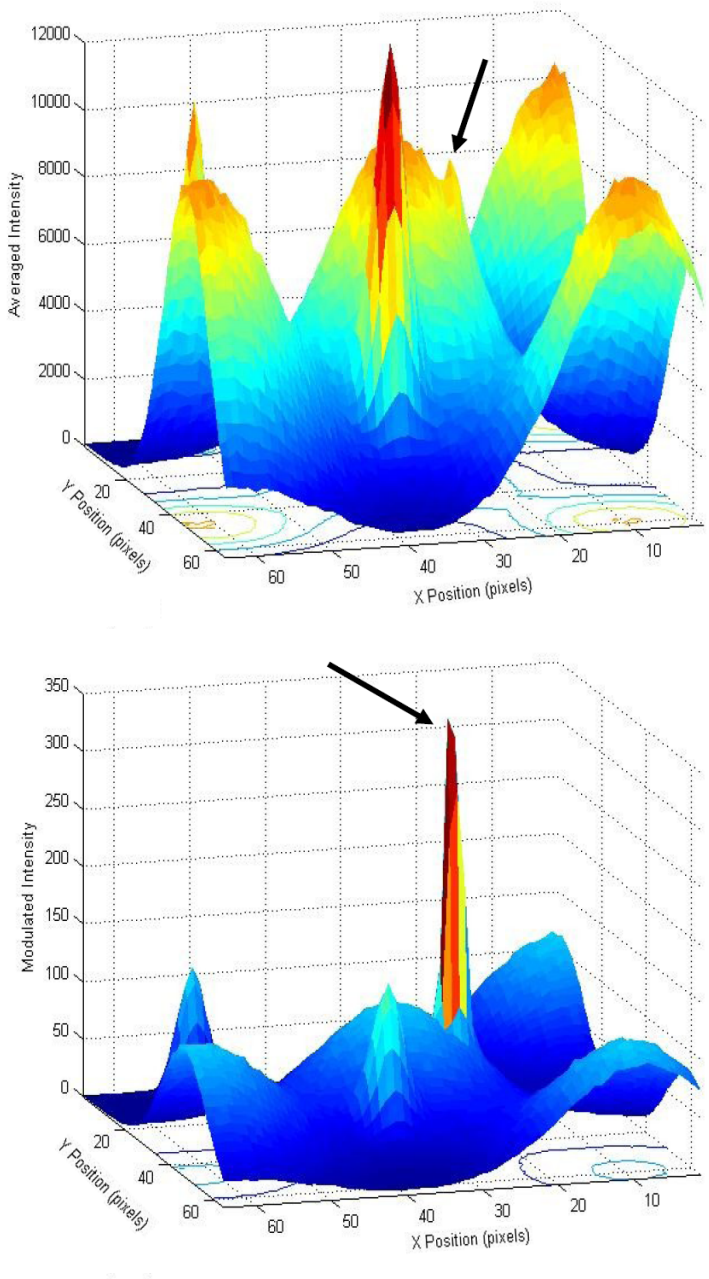

Figure 4.3: Widefield Fluorescence Modulation Signal Extraction: 3(a) Averaged image of entire image stack. Arrow indicates modulated region; 3(b) Extracted image made through plotting power at 25.6 Hz throughout image space. Arrow indicates modulated area that is much more intense relative to constant background compared to 3(a). Representative data appears in previous figure.

addition of fluorescence modulation, those photons arriving during times of secondary illumination are amplified and those arriving during times of primary excitation only are suppressed. Secondary illumination modulated at a frequency of 100 kilohertz would yield a fluorescence signal that can be demodulated at that frequency, then binned at 100 μsec (corresponding to a 10 kilohertz frequency). This demodulated and binned time trace can be used to generate correlation functions for processes longer than the bin time, including diffusion, which occurs on timescales of milliseconds in a typical FCS setup. As a result, the FCS signal from the desired fluorophore only can be isolated from a complex system precluding typical analysis.

This technique can be similarly extended to selectively obtain dynamic information from CCD data. Imaging rates for this experiment would be 2-5 times that of the modulation frequency. By demodulating over a series of frames representing 2-5 times the modulation period, a demodulated image over 4-25 times the original frame rate is obtained. For a CCD camera capable of 500 frames per second, demodulated images at rates from 40 Hz up to 125 Hz can be obtained. These demodulated image stacks can further be utilized as input for particle tracking or widefield correlation analysis with the added benefit that only those emitters that show a modulation signal are retained in the demodulated images.

4.2.4 Conclusions

The work presented has shown the compatability of widefield confocal imaging with emerging fluorescence modulation techniques. The signal from modulatable fluorophores can be enhanced over the static background signal in a manner that allows for investigation of dynamics on the tens of milliseconds timescale. In addition, the foundation for work to utilize this technology in a sub-millisecond timescale has been completed, which could potentially be an asset for increased sensitivity in experiments such as FCS in living systems.

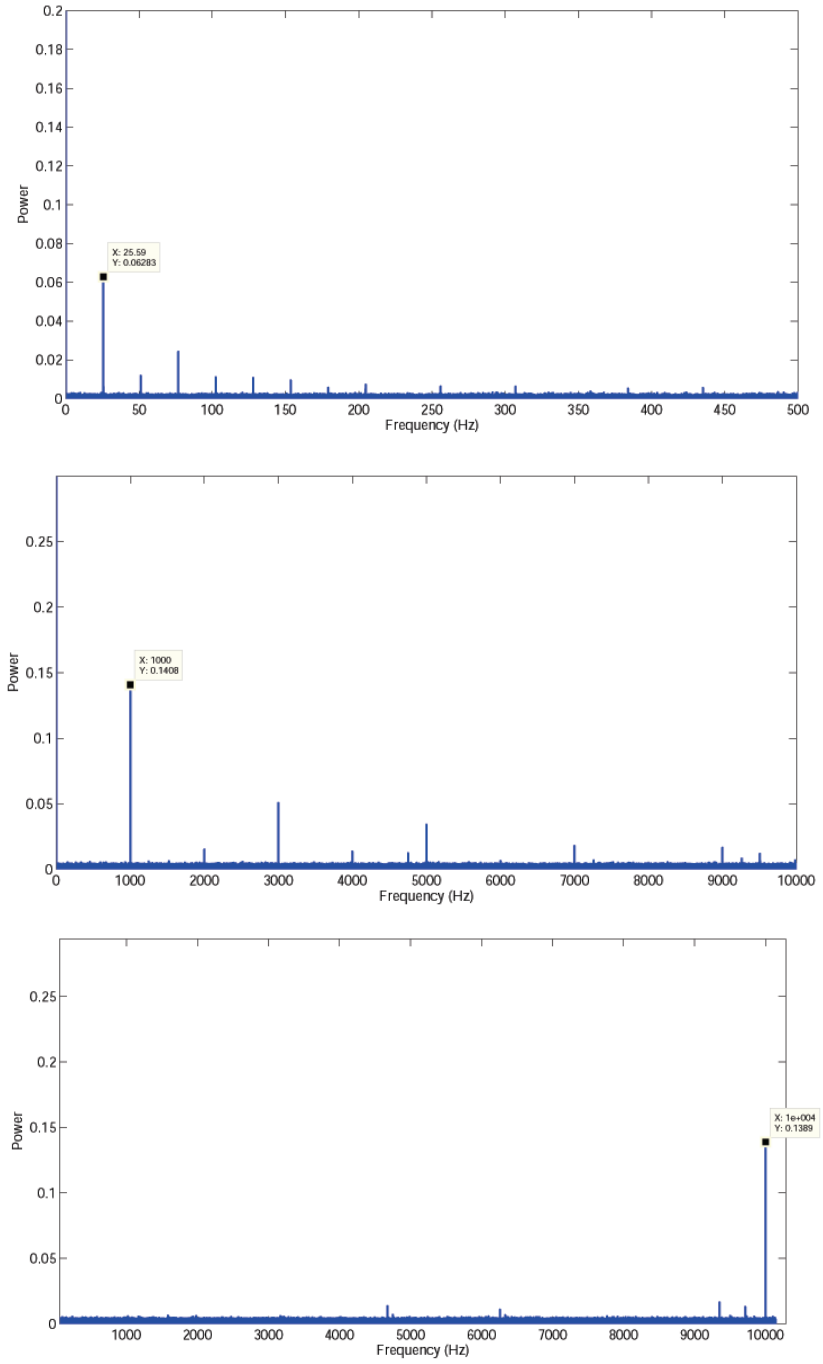

Figure 4.4: Single-point Fluorescence Modulation Signal Extraction: Fourier transforms on binned TCSPC data for Rose Bengal beads modulated with a secondary laser frequency of 25.58 Hz (4(a)), 1 kHz (4(b)), and 10 kHz (4(c)).

4.3 Super-resolution Imaging

4.3.1 Introduction

While fluorescence microscopy contines to be a widely popular technique for investigating living cells, microscopic structures, and even whole multicellular organisms in three dimensions, the technique is limited by its inability to resolve structures smaller than the diffraction limit. This limit, first described by Ernst Abbe in 1897, is around 200 nm for visible light [8]. Other microscopic techniques, such as EM, AFM, and STM, allow for higher spatial resolution down to the molecular level, they are not compatable with imaging living cells.

Multiple new techniques (STED, SIM, 4Pi, I5) have appeared in recent years that have overcome the diffraction limit with the use of specialized imaging equipment [91, 84, 85, 102, 204, 205, 206]. Techniques expoloiting stochastic photoswitching processes (PALM, STORM, ...) avoid the specialized equipment but require long acquisition times and limited fluorophore selection [109, 110]. A more in-depth review of the established techniques appears in section 1.6.

Recently Weiss, Enderlein, *et.al.* have reported their SOFI technique, which uses higher-order statistics analysis of fluorescence fluctuations arising from stochastic blinking of quantum dots [45]. The power of this technique was demonstrated with a 5-fold enchancement in resolution through analysis of movies taken with a standard CCD-equipped widefield fluorescence microscope. The apparatus is arbitrary and insensitive to the actual emitter, required that the emitters demonstrate independent, stochastic fluctuations in fluorescence output at timescales longer than the acquisition time step. This pioneering work relied on the power-law blinking statistics of quantum dots, which will demonstrate fluorescence itermittancy at all timescales. This allowed the use of a standard EM-CCD camera for acquisition, which is typically limited to frame rates around 1000 Hz (1 ms time steps).

While live-cell imaging has been accomplished with quantum dots, the large size

and native bioincompatability of these emitters make them less than ideal for many biological applications. A large body of work exists concerning the use of organic dyes as fluorophores in a biological context as well as the excellent biocompatability and genetic encoding available with fluorescent proteins. For this super-resolution technique to see wide adoption in cell biology studies the technique ideally should utilize such well-characterized fluorophore systems. The majority of organic fluorophores, fluorescent proteins, and DNA-templated silver clusters demonstrate the necessary fluorescence itermittancy but at much shorter (< 100 μsec) timescales [10, 36, 30, 37]. These fluorophores are much more compatable with live-cell imaging and their fluorescence fluctuations can be detected with the use of TC-SPC techniques, which allow for nanosecond or greater time resolution. This adaption to utilize faster blinking timescales requires that the data be acquired serially - a geometry commonly used in a typical confocal microscope.

Here we will demonstrate the extension of SOFI to work with common biocompatable fluorophores in a standard single-point confocal geometry. By recording an intensity *vs.* time trace at each acquisition point and later analyzing these data a super-resolution image can be reconstructed.

4.3.2 Theory

Following the formalism of Dertinger *et. al*, for N independent emitters centered at $\mathbf{r}_k$, the time-dependent fluorescence signal at position r can be expressed as the convolution of the distribution of the fluorescence source and the point-spread function (PSF) of the system ($U(\mathbf{r})$):

$$F(\mathbf{r},t) = \sum_{k=1}^{N} U(\mathbf{r}-\mathbf{r}_k)\,\epsilon_k\,\sigma(t)_k \tag{38}$$

with ϵ_k the constant molecular brightness and $\sigma(t)_k$ the time-dependent fluorescence fluctuation of emitter k at time t. The PSF of the system can be approximated as a

3D Gaussian at position (c_x, c_y, c_z):

$$U(\mathbf{r}) = exp\left(-\frac{(x-c_x)^2+(y-c_y)^2}{2\,\omega_o^2} - \frac{(z-c_z)^2}{2\,\omega_z^2}\right) \tag{39}$$

with ω_o and ω_z describing the radius in the planar and axial directions, respectively. More specifically, these values are equal to the distance from the center of the Gaussian to where the intensity falls to $1/e^2$ times the maximum height, known as the e^2 radius. When approximating a PSF as a Gaussian, the width of the PSF is given as the e^2 diameter.

Given time-series data for a single position $F(\mathbf{r}, t)$, the n^{th} order autocorrelation, $G_n(\mathbf{r}, \tau_1, \ldots, \tau_{n-1})$ is given by

$$G_n(\mathbf{r}, \tau_1, \ldots, \tau_{n-1}) = \{\delta F((r), t)\, \delta F(\mathbf{r}, t+\tau) \ldots \delta F(\mathbf{r}, t+\tau_{n-1})\} \tag{40}$$

where the brackets indicate an average over all time, t. Cumulants of 2^{nd} and 3^{rd} order are equal to the correlation function of the same order. As a result the correlation function is sufficient to observe a decrease in PSF width by transforming from U to U^n for the n^{th}-order correlation. The width of the resulting Gaussian transforms from ω_o as in equation 39 to $\omega_o/\sqrt{n}$, resulting in a $\sqrt{n}$ decrease in the size of the PSF. However, for higher-order correlations, the included lower-order correlations (*e.g.* the 2^{nd} order correlation terms contained in the 4^{th} order correlation that are subtracted out to generate the 4^{th} order cumulant) obscure the expected *sqrtn* decrease in PSF width by the lower-order correlations.

To obtain super-resolution in this case, the correlation is not sufficient. Instead, what must be used is the higher-order cumulants (C_n), which do not contain these lower-order cross-terms. The cumulants can be expressed in terms of correlation functions as seen in equations 41 through 43, shown up through the fourth order cumulant.

$$C_2(\mathbf{r},\tau_1) = G_2(\mathbf{r},\tau_1) \tag{41}$$

$$C_3(\mathbf{r},\tau_1,\tau_2) = G_3(\mathbf{r},\tau_1,\tau_2) \tag{42}$$

$$\begin{aligned} C_4(\mathbf{r},\tau_1,\tau_2,\tau_3) &= G_4(\mathbf{r},\tau_1,\tau_2,\tau_3) \\ &\quad - G_2(\mathbf{r},\tau_1) * G_2(\mathbf{r},\tau_3) - G_2(\mathbf{r},\tau_1+\tau_2) * G_2(\mathbf{r},\tau_2+\tau_3) \\ &\quad - G_2(\mathbf{r},\tau_1+\tau_2+\tau_3) * G_2(\mathbf{r},\tau_2) \end{aligned} \tag{43}$$

With the removal of the lower-order cross terms, the cumulant yields super-resolution even in the case of multiple emitters contributing signal at a single position because the cumulants of cross-terms go to zero. The cumulant can be described in terms of the relevant physical characteristics by the following:

$$C_n(\mathbf{r},0) = \sum_k U^n(\mathbf{r}-\mathbf{r}_k)\,\epsilon_k^n\,w_k(0) \tag{44}$$

with $w_k(0)$ a weighting function, based on the fluctuation properties of emitter k, with the expression for the function dependent on the order n of the cumulant. As previously mentioned, the transformation of the PSF from U to U^n for the n^{th}-order cumulant yields a $\sqrt{n}$ increase in spatial resolution.

Cumulants calculated by way of correlation functions becomes computationally expensive very quickly with increasing order. For the SOFI technique only the amplitude of the cumulant is needed, which can be calculated by setting all of the time lags to zero ($\tau_n = 0$). Through this transformation the n^{th} order correlation function is reduced to the n^{th} order central moment, μ_n, given as

$$\mu_n = \{F(\mathbf{r},t) - \{F\}\}^n \tag{45}$$

where the brackets indicate an average over all time, t. The second-order central moment is commonly known as the variance, the third the skewness, and the fourth kurtosis. Strictly speaking, the first-order central moment is zero, but here the 'first

order moment' will refer to the mean. These higher-order central moments can be transformed into higher-order zero-delay cumulants κ_n for the n^{th} order cumulant) through a recursive formula (equation 46).

$$\kappa_n = \mu_n - \sum_{k=1}^{n-1} \binom{n-1}{k-1} \kappa_k \, \mu_{n-k} \tag{46}$$

The results of this formula for the first six cumulant orders appear in equations 47 through 52.

$$\kappa_1 = \mu_1 \tag{47}$$

$$\kappa_2 = \mu_2 \tag{48}$$

$$\kappa_3 = \mu_3 \tag{49}$$

$$\kappa_4 = \mu_4 - 3\,\mu_2^2 \tag{50}$$

$$\kappa_5 = \mu_5 - 10\,\mu_2\,\mu_3 \tag{51}$$

$$\kappa_6 = \mu_6 + 30\,\mu_2^3 - 10\,\mu_3^2 - 15\,\mu_2\,\mu_4 \tag{52}$$

As can be seen, the expressions for the cumulants above 4^{th} order increase in complexity quite rapidly with the 25^{th} order cumulant in terms of central moments having 232 terms. Even with the complexity, for each fluorescence signal the higher-order moments are straightforward to calculate, leaving the calculation of the zero-delay cumulants to be simple multiplication of the necessary central moments. This reliance on the central moment of a single time trace does have disadvantages regarding shot noise that will be discussed later as well as possible methods to avoid such an issue.

It should be noted that for all Gaussian distributions the higher-order ($n \geq 3$) moments, and therefore the higher-order cumulants, are zero. Herein lies the requirement that emitters imaged by the SOFI method must blink on an experimentally-relevant time scale. A constant emitter will generate a Gaussian emission distribution at

sufficiently high count rates and therefore no signal at higher orders. Conversely a non-constant emitter with m emission states will show an m-modal emission distribution and will yield signal at higher orders due to the non-Gaussian character of this distribution. The more non-Gaussian this distribution is the greater the higher-order signal will be.

4.3.3 Methods

Simulations to demonstrate the performance of the SOFI analysis were written in MATLAB. A shared fluctuation trajectory was generated with the `hmmgenerate` function with a length typically 1000 points longer than the desired number of time steps per pixel and amplitude either 1 or 0. Transition statistics between the emissive and nonemissive states were equivalent for all emitters. A single CCD-type 2-D fluorescence image was generated individually for each Gaussian-modeled emitter. To generate the intensity *vs.* time trace of length k for a single pixel, the amplitude of each emitter was multiplied by a different k-length piece of the common fluctuation trajectory. These products were then summed over all emitters, generating a single intensity *vs.* time trace for that pixel. Poissonian shot noise was modeled by multiplying this trace by a specified amplitude, adding a constant background to all points in this trace, then choosing a Poissonian-distributed random number from a distribution of mean equal to the base value at that time step using the `poissrnd` function.

To demonstrate an increase in resolution an image area of 100 x 100 pixels with width of 10 nm containing 6 stationary emitters was simulated. These emitters had individual PSF widths of 203 nm corresponding to a diffraction-limited spot at 500 nm with a 1.2 NA objective. For this test case the emitters were placed in pairs with distances 3.2, 2.0, and 1.0 times the width of the PSF apart. Pairs were placed 350 nm or 250 nm apart from one another in the orthoganal dimension. Similar simulations

were run with a single isolated emitter to show the expected decrease in PSF width with increasing cumulant order.

Analysis was performed again in MATLAB. For each pixel in the image, the needed central moments (with MATLAB's `moment` function) were calculated from the intensity *vs.* time trace for that pixel. These central moments were then utilized in the necessary moments-to-cumulant function generated by equation 46 evaluated by the MathStatica package in Mathematica. Values for the cumulants were mapped back to the pixel location to produce the final higher-order cumulant super-resolution images.

Experimental data was acquired on a homebuilt confocal system based around an Olympus IX-70 inverted microscope. An experimental schematic and description appears in chapter 2.4. The 632.8 nm line of a HeNe laser at 27.8 μW or 3.9 μW was aligned into the back aperature of the microscope and reflected off a 670 nm long-pass dichroic mirror and through a 100x oil immersion objective (1.4 NA, Olympus) before exciting a sample. The emission from the sample was collected with the same objective, passed through a 710/40X band-pass filter and 1.5x magnification lens, before entering a 50 μm fiber aligned to the conjugate focal plane at the side port of the microscope. This fiber served the purpose of the confocal pinhole as well as transmitting light to an APD photodetector.

Signal from the APD was recorded with a TCSPC module controlled by custom-written software (Microsoft Visual C++) that also controlled the scanning stage. Data for an entire region of interest was acquired by raster scanning the single confocal point in 25 nm steps across a 1 μm by 1 μm area. At each point TCSPC data was recorded with a dwell time of 250 or 500 ms.

DNA:Ag emissive nanoclusters (630 nm/700 nm excitation/emission) were used as the fluorophore for this study. These emitters were synthesized by combining single-stranded DNA (5'- CCC TAA CTC CCC - 3') with silver nitrate ($AgNO_3$) and sodium

borohydride (NaBH4) in a 1:6:3 ratio in aqueous solution. These solutions were spin cast 5% PVA with 2-, 10-, or 100-fold dilutions onto standard glass coverslips and imaged.

4.3.4 Results and Discussion

The properties of the SOFI method can be easily demonstrated with simulated data. For the case of a single isolated emitter the square-root dependence of the width of the PSF on the cumulant order can be seen in figures 4.5 and 4.6. This dependence can clearly be seen in figure 4.6 where the data points fall very well along the expected $PSF/\sqrt{n}$ line for the n^{th} order cumlant.

To demonstrate an increase in resolution leading to the separation of previously unresolvable emitters, an array of 6 emitters was simulated as described in section 4.3.3. As can be seen in figure 7(a) the particles simulated were at spatial separations ranging from nearly resolvable in the most widely-spaced case to a spacing resulting in a single local maximum. With increasing cumulant order these emitters, thanks to their stochastic blinking, can be more and more effectively resolved. Figures 7(b) through 7(d) demonstrate this increase in resolution finally leading to the spatial separation of the two most closely-spacedd points. Cross-sections taken along the row containing the closest pair of emitters shows this progression from a single wide Gaussian peak to separable emitters with nearly baseline resolution is shown in figure 4.8.

Due to the nature of the cumulant technique, those pixels containing a constant signal, either from non-blinking fluorophores or random background, will not appear in the higher-order images. This does have the advantage of selectively amplifying blinking emitters over a constant signal. For those emitters that do blink, the amplitude of the fluctuations is amplified by a greater and greater amount as the cumulant order increases. In addition to brightness differences, it is also possible for a molecule

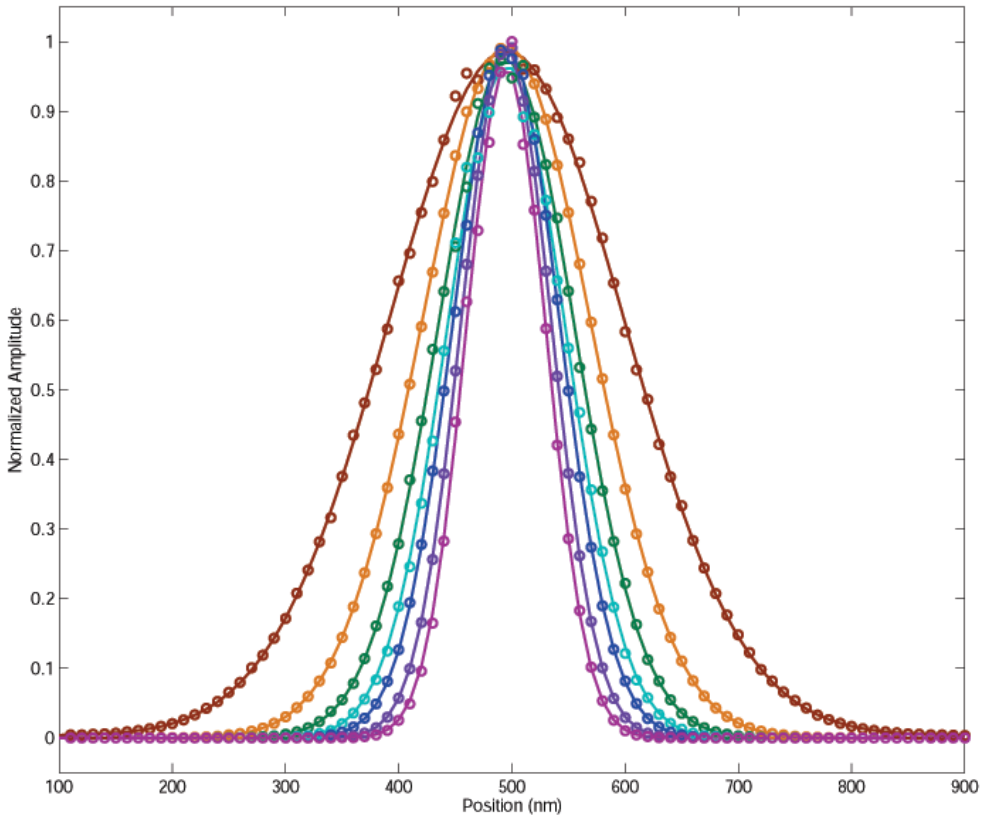

Figure 4.5: Simulated data (circles) and Gaussian fits (lines) for a single isolated emitter and higher-order cumulants. Orders pictured are the first through ninth, save for sixth and eighth, omitted for clarity.

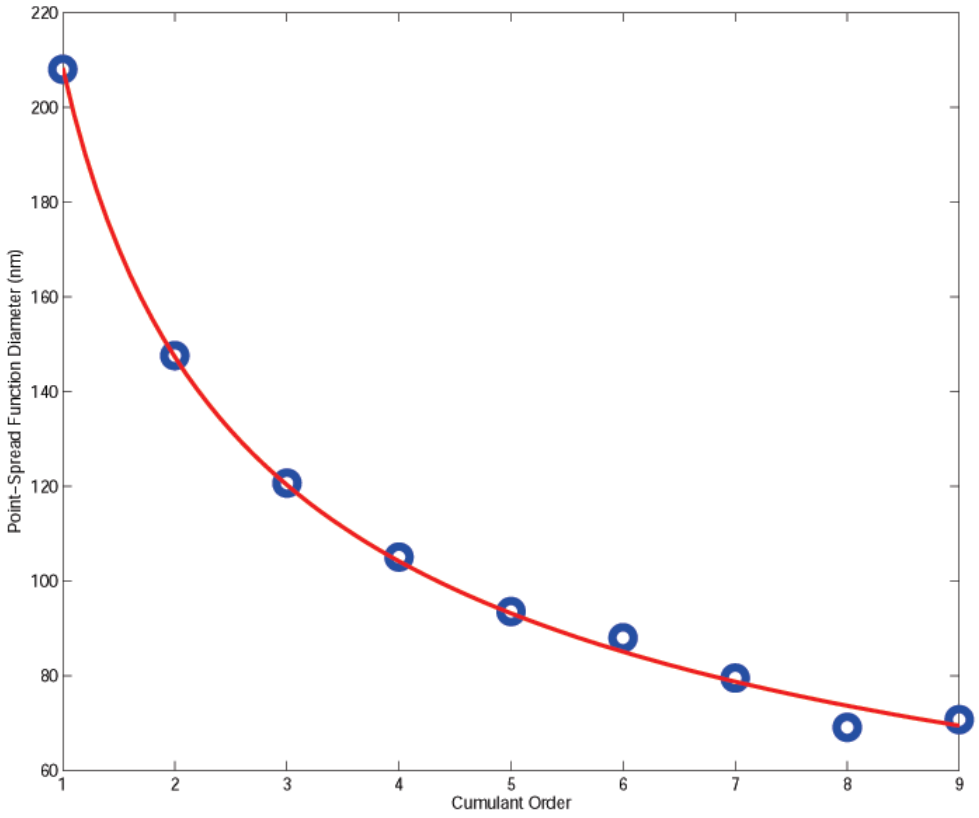

Figure 4.6: Gaussian widths (circles) for peaks fit in 4.5. Red line represents expected square-root dependence of PSF on cumulant order.

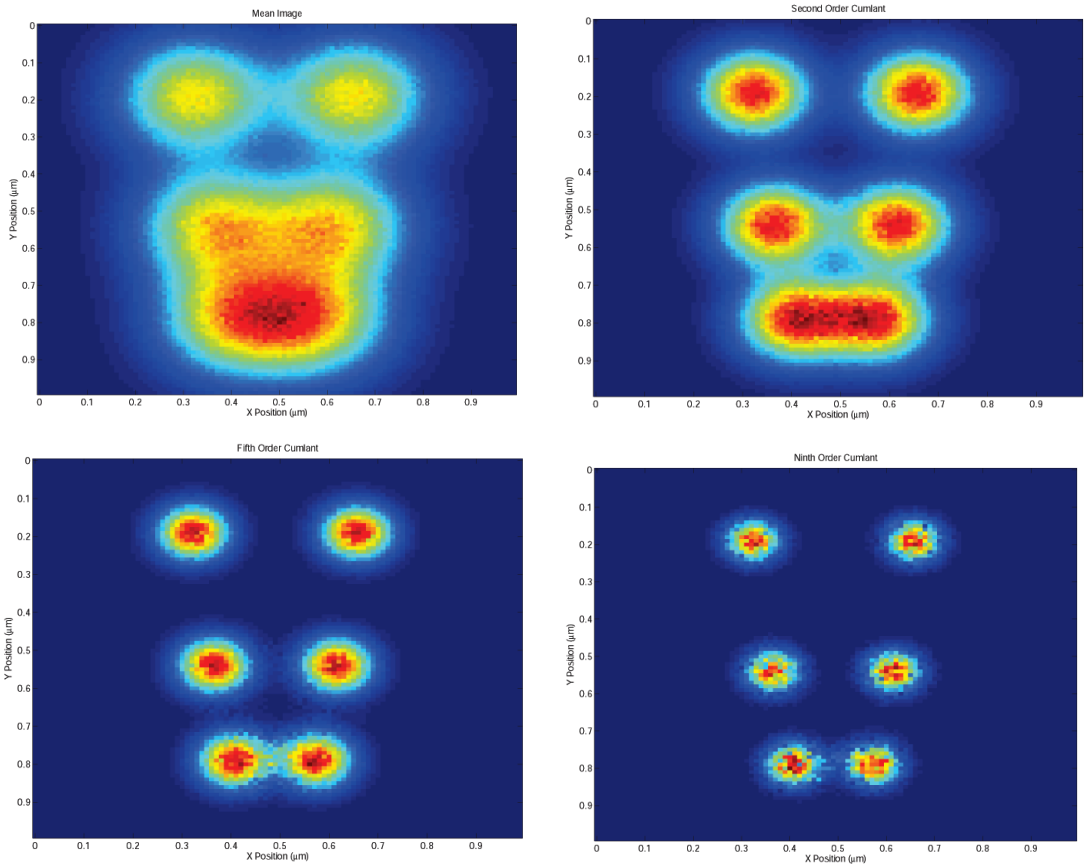

Figure 4.7: Mean of emission from six emitters (7(a)) and cumulant maps of second, fifth, and ninth order (7(b), 7(c), and 7(d), respectively).

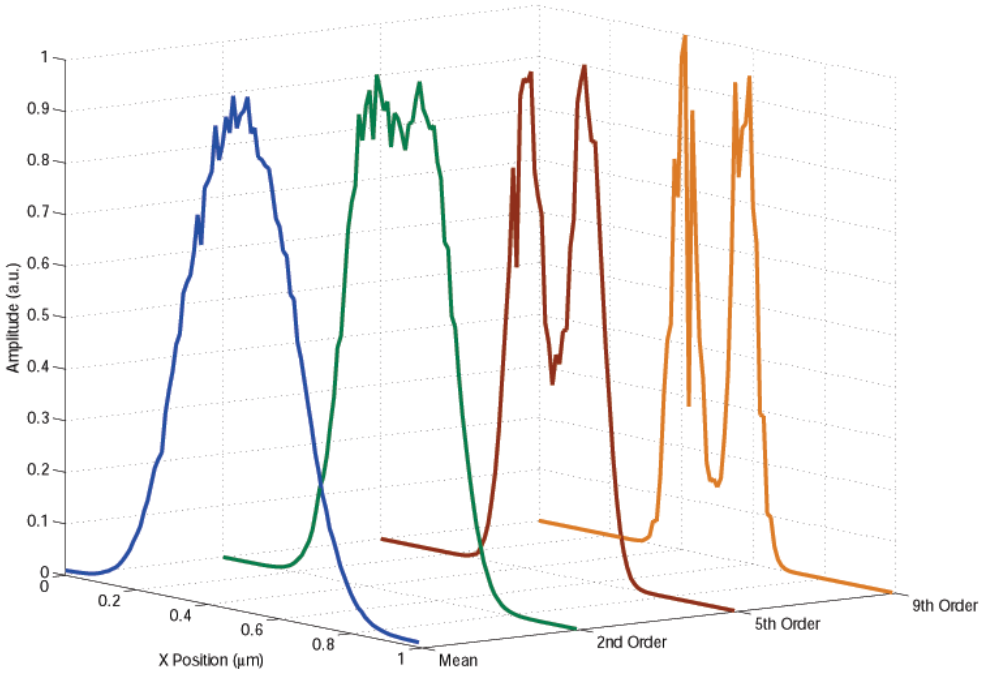

Figure 4.8: Normalized cumulant amplitude for increasing cumulant order for a pair of closely-spaced emitters (separation = PSF width) appearing in figure 4.7. An increase in cumulant order reveals a pair of emitters from below single Gaussian peak and resolves with nearly baseline resolution with highest cumulant order.

with a larger blinking amplitude to dominate an image at higher order and obscure fluorophores with less symmetric blinking statistics.

Amongst simulated emitters with identical blinking statistics it is possible for different emitters to yield different intensities in the cumulant maps. This can be justified by recalling that the cumulants are extensions of lower-order statistics that do not always track between different emitters - that is, it is very possible for two signals to have the same mean but different variances, or the same variance but different skew. In the case of synchronous (CCD-type) data, this has the effect of suppressing whole emitters in a cumulant map. For asynchronous data it is single pixels that are supressed, yielding maps containing emitters that appear like those seen in figure 4.9.

The simulated data demonstrates the capacity of SOFI analysis to resolve closely-spaced, stochastically-blinking emitters imaged serially instead in a parallel, widefield geometry. From these simulations it is also apparent that the timescale of the blinking is not directly tied to the success of the super-resolution imaging as long as the acquisition time step is capable of detecting the blinking process (that is $\tau_{Blinking} \gg \tau_{Acquisition}$). For CCD data acquisition this time step is on the order of milliseconds, corresponding to a 1000 Hz frame rate. As a result the emitters that would work for such an experiment are limited to those that show such long-lived blinking dynamics.

In order to extend this method to utilize molecules with faster blinking dynamics, a sample of DNA:Ag nanoclusters embedded in a PVA film were imaged with a scanning single-point confocal microscope. This geometry allowed for much greater time resolution than the previously-used widefield method and the blinking dynamics of the silver clusters on microsecond timescales could be utilized for SOFI analysis. Autocorrelations of two selected pixels (figure 4.10) from such an experiment illustrate the fluctuation timescale of tens of microsceconds utilized to generate a series SOFI super-resolution images (figure 4.11).

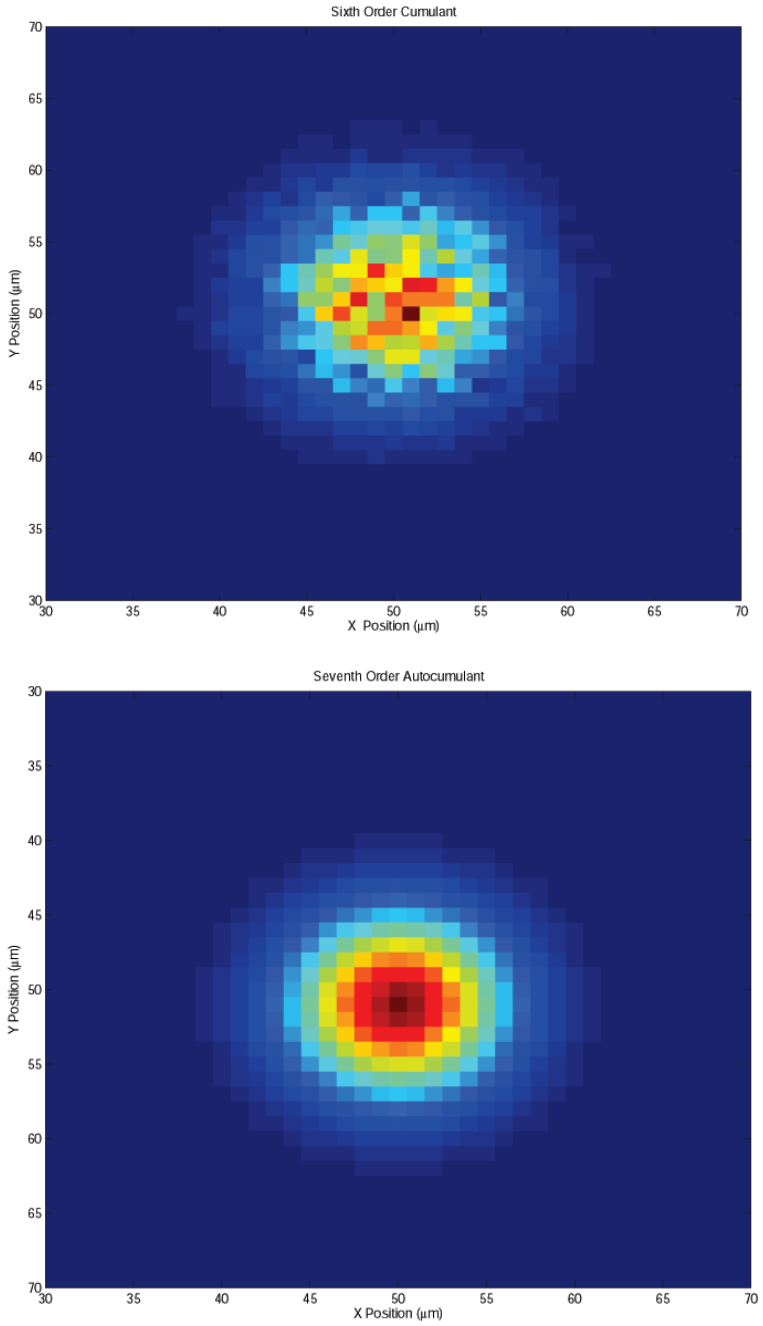

Figure 4.9: Autocumulant map for single emitter showing poor imaging that can occur for some cumulant orders. The sixth order cumulant map 9(a) suffers from this detriment while the seventh order cumulant map 9(b) and the fifth order cumulant map (not shown) do not.

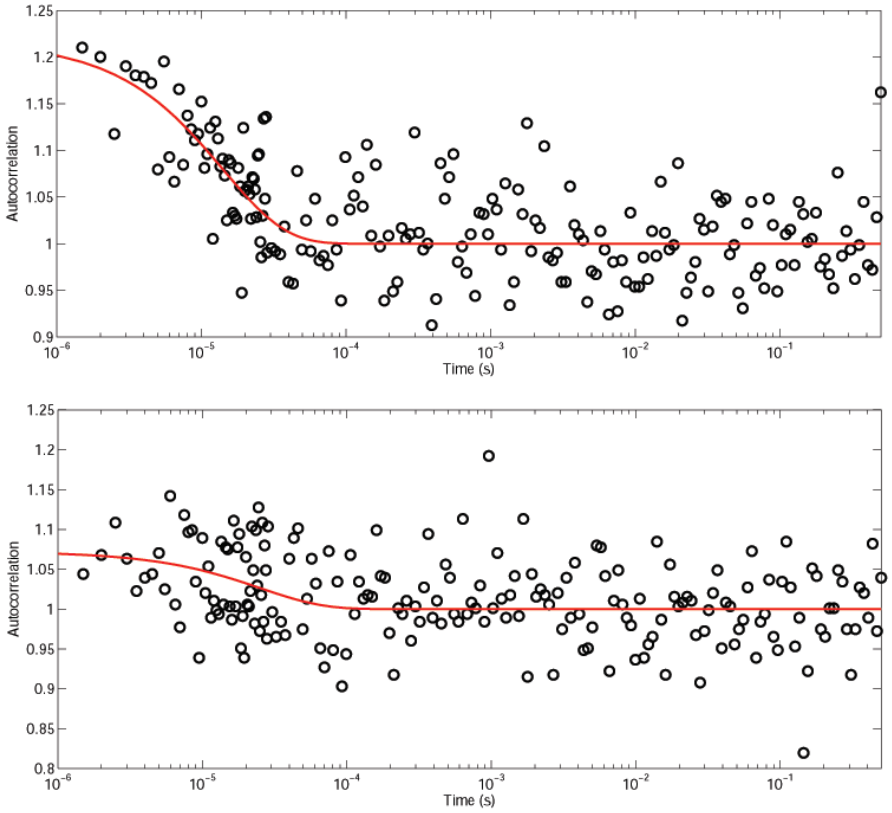

Figure 4.10: Autocorrelations for two pixels in a SOFI experiment. The autocorrelation data can be fit to a single exponential in both cases with a fit of 14.1 μs (10(a)) or 24.9 μs (10(b)). These data were taken at left (10(a)) and right (10(b)) indicated positions in figure 4.11.

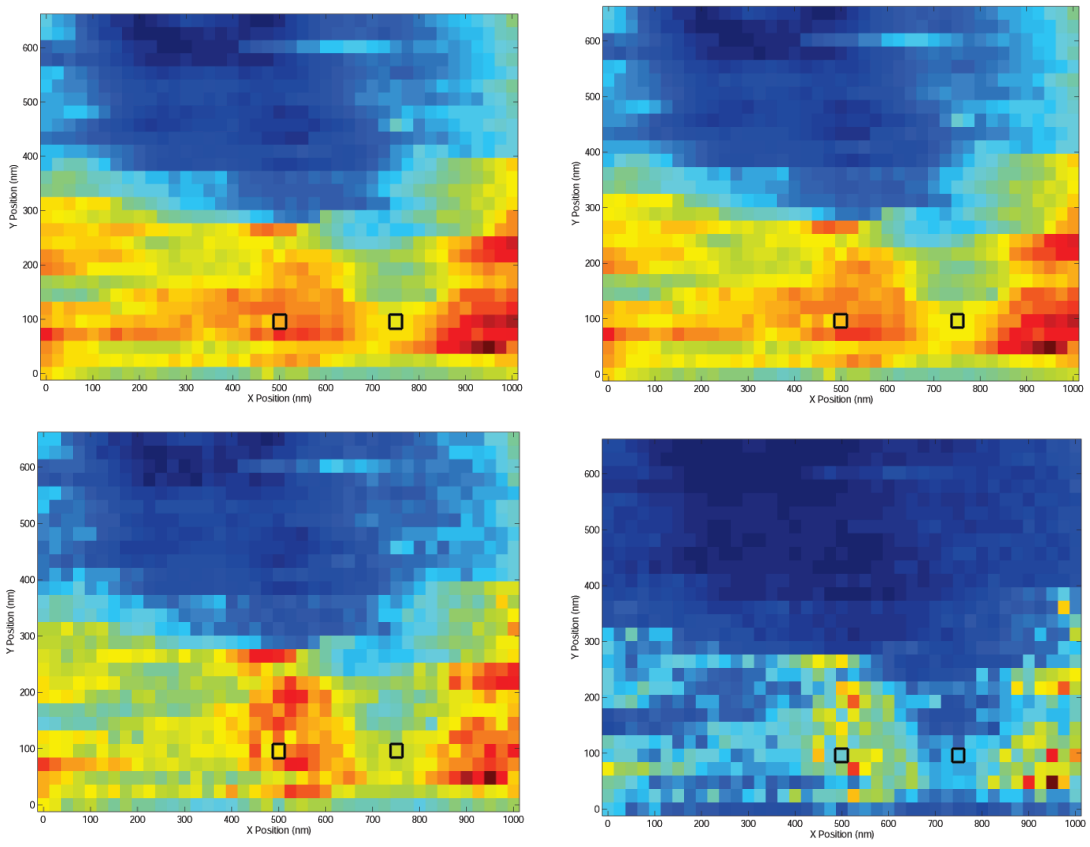

Figure 4.11: Experimental SOFI images of DNA:Ag nanclusters in PVA. Average image pictured in 11(a) with 11(b) - 11(d) corresponding to the second, fourth, and ninth order cumulant maps. Pixels in black correspond to autocorrelation data in figures 10(a) (left) and 10(b) (right). 25 nm per pixel, 250 ms dwell time.

From the resulting cumulant maps it can be seen that the SOFI analysis can result in an increase in the resolution of multiple closely-spaced emitters. Data taken along a single row of these images is shown in figure 4.12. This single row contains data from three emitters at approximately the left edge, center, and right edge of the imaging area. As can be seen by the curve corresponding to data from the mean image, the inclusion of multiple emitters is apparent but they cannot be satisfactorally resolved due to their close proximity. However, with higher order cumulants, up to the 9^{th} as pictured, the three individual emitters can be resolved. Higher cumulant orders than utilized here would presumably continue this resolution improvement such that these three emitters could be totally separated from one another with sufficiently high cumulant order.

An interesting case illustrating the nature of high time resolution in the SOFI analysis was noted in the data appearing in figure 4.13. The emitter at the lower-left of the imaging area shows an atypical fluctuation process of 5.4 milliseconds in addition to an 8.3 microsecond component more comparable to other emitters imaged in these experiments. These two distinct timescales are apparent in the autocorrelation for a signal at this emitter (figure 14(a)), contrasting with the more typical single-timescale fluctuations seen in another emitter imaged by the same experiment (figure 14(b)). This more typical emitter does show a small amount of fluctuation on the millisecond timescale but at a much lower proportion (10.2% versus 45.4%).

By binning the time series data at 250 μsec the fast blinking dynamics are obscured and the difference in the blinking dynamics becomes even more apparent. Histograms of the emission distribution for the two emitters appear in figure 4.15. The histogram for the typical emitter (15(b)) shows a distribution that can be nearly fit by a single Gaussian. There is some non-symmetric Gaussian character but by and large a single peak would do well to fit this data. However, for the non-typical emitter with a long timescale component, there are clearly two or more components in the emission

histogram (15(a)). These multiple components correspond to the average value of the detected photon counts from the distinct emissive states of the molecule. As alluded to previously, this non-Gaussian character in the emisssion distribution is what gives rise to the signal at higher orders.

The manifestation of this difference in statistics due to processes at different timescales can be seen in the two cumulant maps of figure 4.16. These figures are both 9^{th}-order cumulant maps of the same data set. Figure 16(a) was generated by performing the SOFI analysis on photon data binned at 5 μsec, while figure 16(b) was analyzed in the same way, but by binning at 500 μsec. This longer bin time obscures the fast blinking dynamics of the typical emitters and only reveals the signal for the emitters fluctuating at longer timescales. Approached from the other direction, insufficient time resolution in the data acquisition obscures and eliminates the signal from those emitters whose fluctuation dynamics are at more rapid timescales.

The trade-off with using faster timescales for analysis is increased influence of shot noise in measurements. As such, it is difficult to reliably fit the PSF for a data set across all cumulant orders without very high count rates or long bin times. For this reason, the data that best illustrates the decrease in PSF width with increasing cumulant order was that of the atypical long timescale blinking emitter. Shown in figure 4.17 the sharpening of the Gaussian PSF is demonstrated with 2.5 μsecond binning for several cumulant orders, while the remainder of the cumulants show noisy results that are difficult to fit to a Gaussian peak. By binning at 250 μsec, all orders can be fit to Gaussians, demonstrating the square root dependence of the PSF width on cumulant order (figure 4.18). Extrapolating the data to the original PSF width yields a value of 315 nm, which is slightly higher than the expected 250 nm (700 nm, 1.4 NA objective). The alternating odd-even behavior of the PSF width shown in figure 4.18 is most likely due to an external interfering 60 Hz signal in the experimental data. Even with these constraints the PSF width can be reduced to 100 nm for the

10th order cumulant. Increasing the cumulant order utilized should increase this PSF tightening to below 100 nm.

The previously mentioned role of shot noise in the measurements is one that is retained in autocorrelation and autocumulant analysis. Shot noise and other random fluctuations are only correlated at $\tau = 0$ and are not present in measurements at any other delay. In addition random noise is not correlated in space, such that two synchronous signals separated in space will show no correlation due to noise. Weiss and Enderlein utilized this fact to eliminate noise with cross-cumulant of synchronous data obtained with a CCD camera. However, because the serial confocal data is necessarily asynchronous, this method is precluded from being used here.

The previous researchers also avoided the influence of shot noise by utilizing autocumulant results at other delays and integrating to estimate the value at zero delay. The use of the zero delay value, however, is much more convenient computationally than any other value. Cumulant functions decrease monotonically and the SOFI analysis should not depend on which delay value is used as the relative values of the cumulant amplitudes are what is of concern. As such one proposed method to avoid the zero delay noise peak is to take the amplitude at the first delay rather than the zero delay amplitude. Rapid time steps ensure that the value for the first delay will be very close to that of the noise-free zero delay and would avoid the need to calculate the cumulant function over a very large set of delays, which would be computationally expensive. It may be possible, at least for some cumulant orders, to use the same rapid method used here, where the central moment is quickly computed and combined to generate autocumulants, but instead rely on the cross-moment between an original signal and this same signal, but shifted a single time step.

Where before quantum dots proved to be the best choice of fluorophore for their long blinking timescales, here the use of DNA:Ag sliver clusters was of particular benefit. Attempts were made to use quantum dots to repeat the previous work in

a serial manner, but this was made difficult by the tendency of the quantum dot to enter a long-lived dark state during the acquisition. Images that showed only half of a PSF or no signal over a large area where it was expected were common due to this quirk of quantum dot emission. Silver clusters, however, rarely have such long-time blinking and retain the extremely low photobleaching and high count rates of quantum dots.

When adapting this method to work with organic dyes or fluorescent proteins photobleaching is going to be of particular concern. To fit data to a full 2-D Gaussian the molecule must emit over the entire time that it is being imaged. Serial data collection limits the time that a single flurophore is illuminated, but continuous emission over a time of minutes is still necessary for effective imaging. It remains to be seen how difficult it will be to realize the use of organic dyes or fluorescent proteins as labels for confocal SOFI analysis, but as it stands DNA:Ag nanoclusters are particularly well-suited for this technique.

4.3.5 Conclusions

Through the use of autocumulants generated from central moments, it is possible to rapidly generate super-resolution images from asynchronous time series data. This allows for the SOFI technique to exploit stochastic blinking in a much wider range of fluorophores than the quantum dot systems available with CCD-based systems. The vital qualification for using the faster blinking timescales of organic dyes, silver clusters, or any other fluorophore is that the blinking timescale must be longer than the acquisition time step. For CCD-based systems this timestep is, at best, hundreds of microseconds for a very limited area. By allowing asynchronous time data from single-point detectors fluorescence intermittancy timescales as fast as nanoseconds are certainly possible due to the very high timing resolution of TC-SPC systems. For practical purposes microsecond timescales are sufficient for detecting fluorescence

blinking but one can imagine using even the antibunching dynamics on the picosecond timescale to generate super-resolution images. While this would be a great difficulty to experimentally realize the antibunching process would satisfy the qualifications for the SOFI technique.

More importantly, opening higher-order cumulant image processing to faster dynamic processes greatly improves the applicability of this technique. An EMCCD camera capable of single-molecule imaging at hundreds of frames per second and quantum dot labelling is not universally adopted while scanning TC-SPC confocal systems are almost required equipment for modern cell biology. In addition the wide array of organic fluorophores as cell labels, which almost all blink on some accessable timescale, allow the autocumulant approach detailed here to become a broadly useful super-resolution microscopy technique. As has been demonstrated with simulations and experimentally, the microsecond blinking timescale of DNA:Ag nanoclusters can be used in a confocal geometry to obtain super-resolution images with this novel confocal SOFI method.

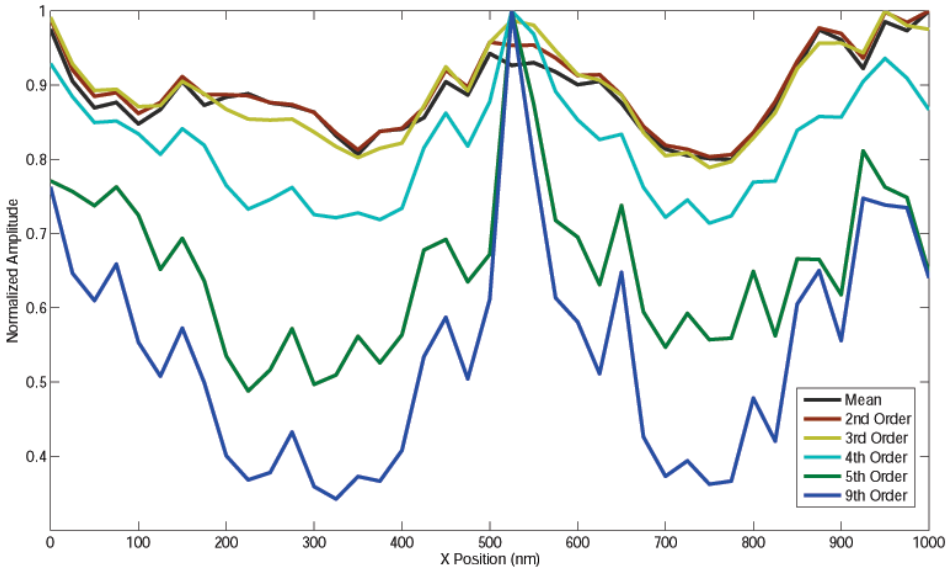

Figure 4.12: Data from the row corresponding to the 75 nm position in figure 4.11. As the cumulant order increases it is apparent that the previously obscured emitters can be increasingly resolved.

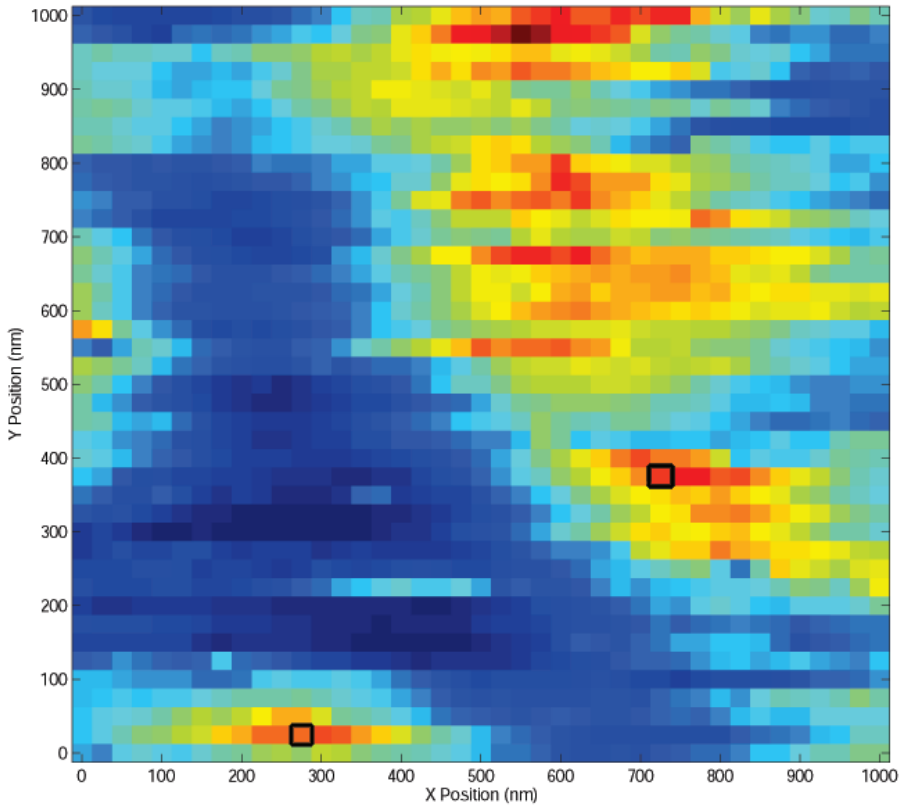

Figure 4.13: Mean confocal image of DNA:Ag nanoclusters. The pixel indicated at the lower-left corresponds to signal from an emitter showing atypical fluctuation timescales. This is contrasted with the emitter at the upper-right indicated pixel in later figures. 25 nm per pixel, 500 ms dwell time.

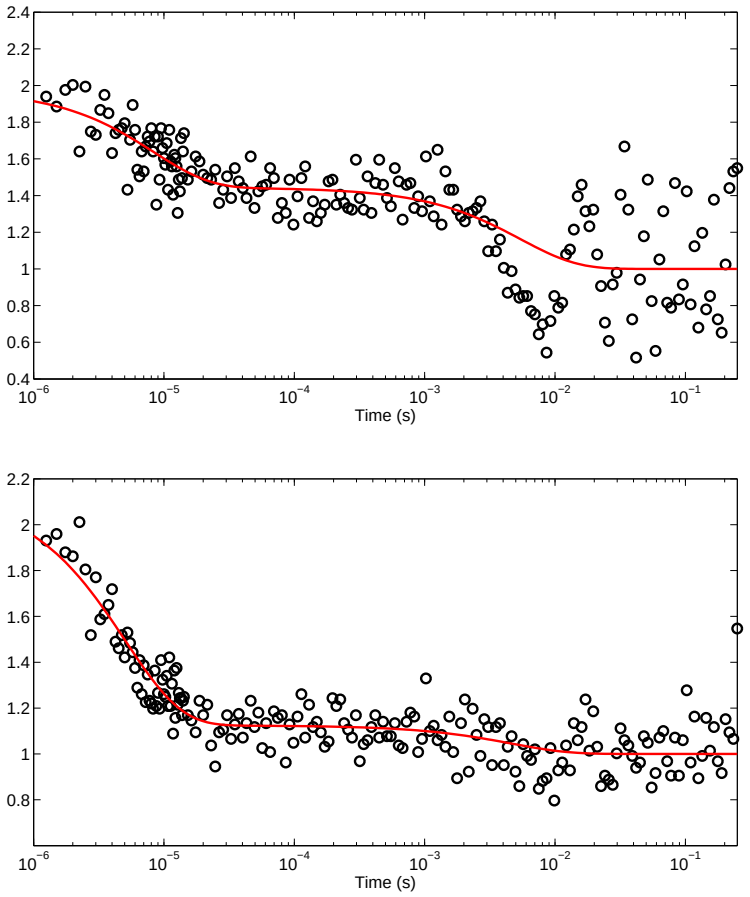

Figure 4.14: Autocorrelations for the left (14(a)) and right (14(b)) pixels indicated in figure 4.13. Each autocorrelation was fit to a biexponental. Fits (weight): 14(a) - 8.3 μsec (.546), 5.4 ms (.454); 14(b) - 5.0 μsec (.898), 4.6 ms (.102).

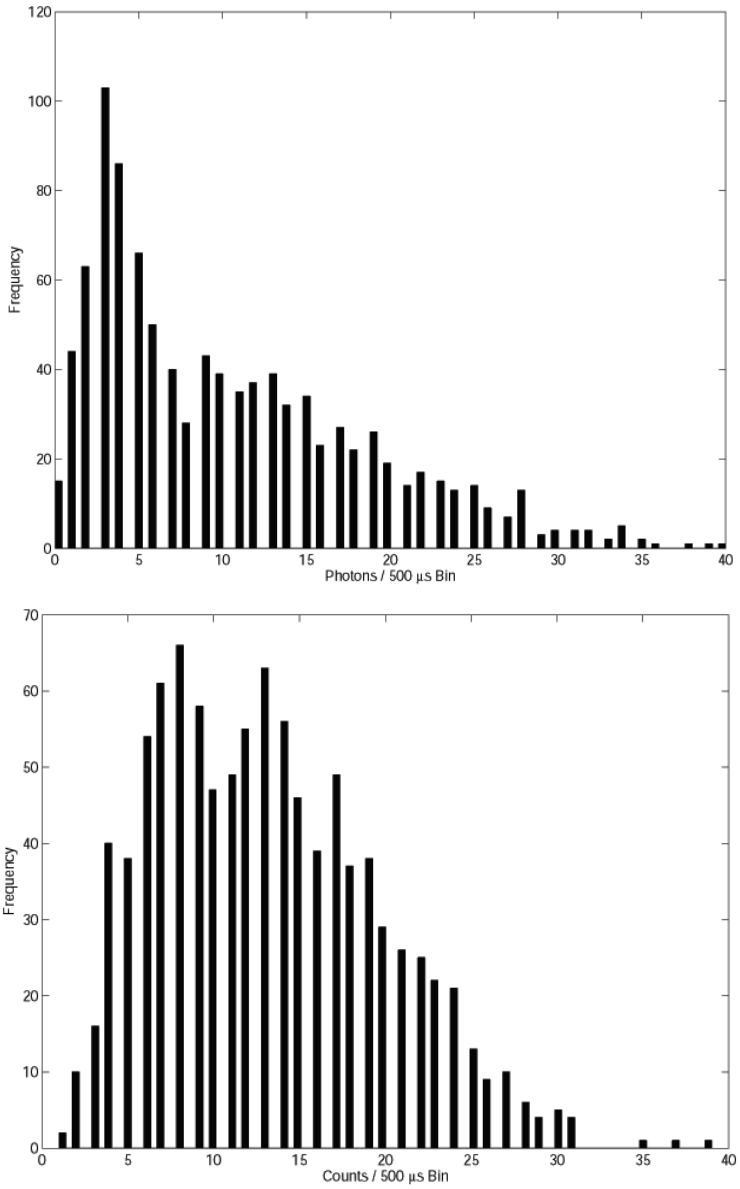

Figure 4.15: Emission distribution histograms of data from the two emitters indicated in figure 4.13 binned at 500 μsec. The atypical timescale fluctuations lead to a multimodal distribution in 15(a) versus the more Gaussian distribution of 15(b).

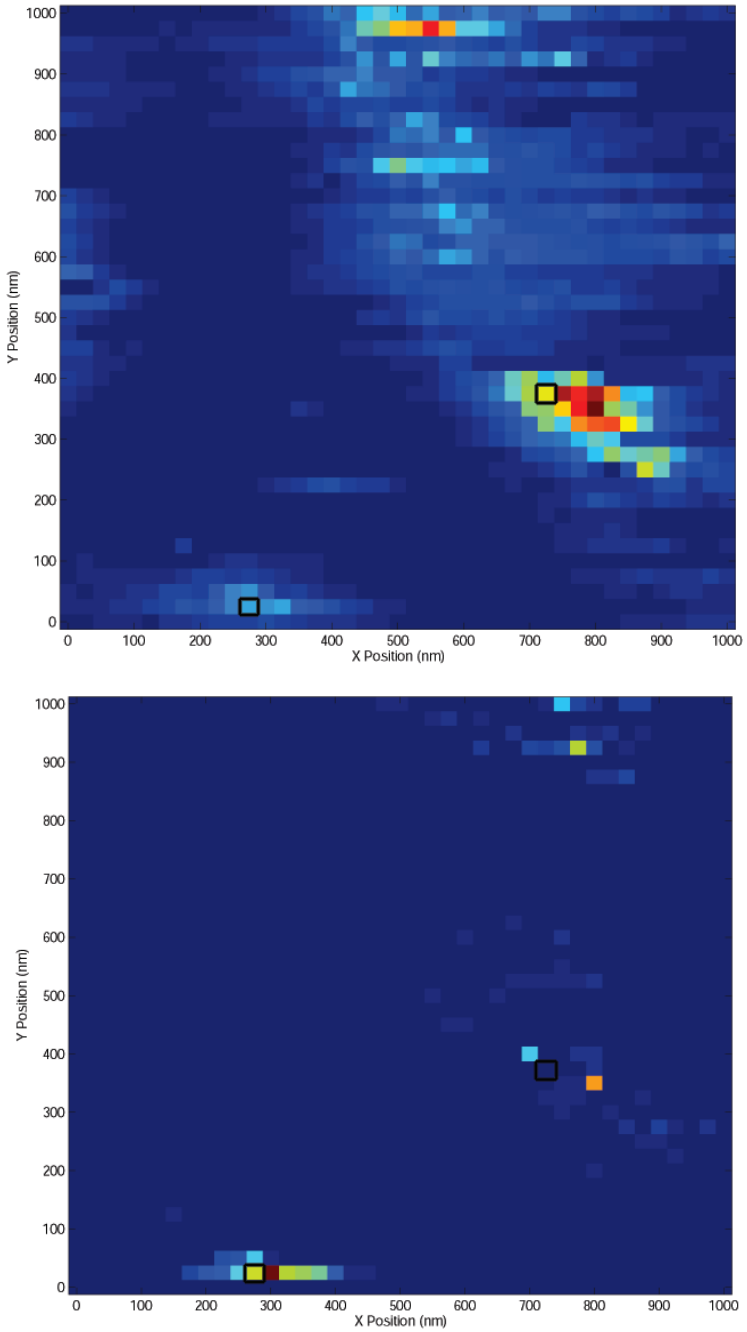

Figure 4.16: Resulting 9th order cumulant maps for the data presented in figure 4.13. The map in 16(a) was generated by SOFI analysis on data binned at 5 μsec, capturing the fast blinking dynamics. The map in 16(b) was generated by SOFI analysis on data binned at 500 μsec, obscuring all but the atypical long timescale blinking dynamics of the emitter in the lower left.

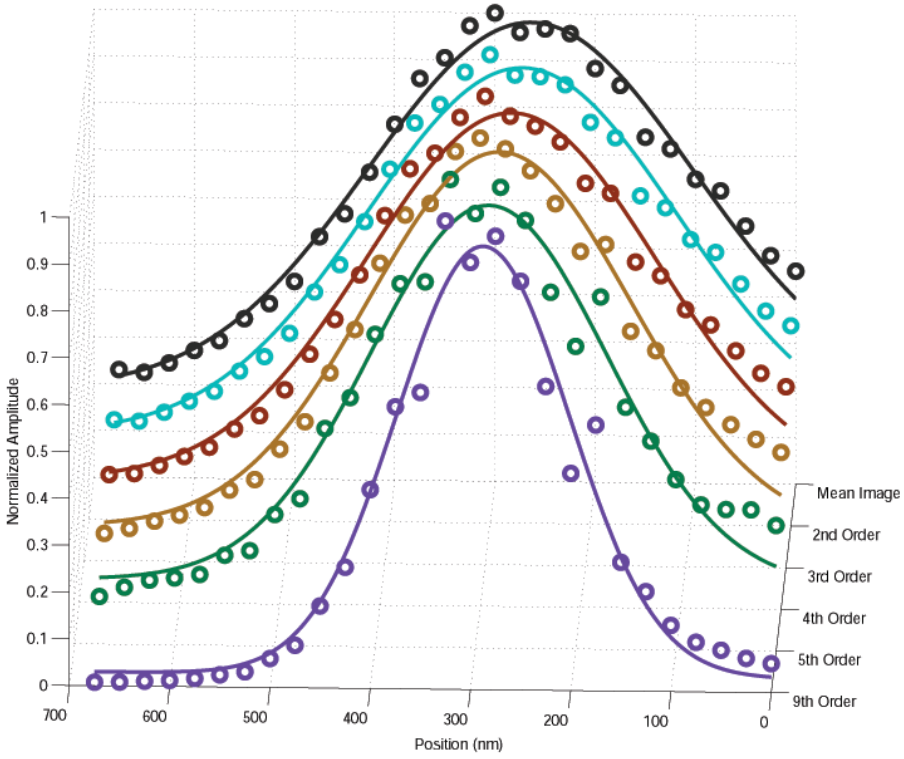

Figure 4.17: Gaussian fits of data with increasing cumulant order. An increase in cumulant order results in a decreased PSF width. The original PSF is fit to a Gaussian of width 324 nm and the 9^{th} order to one of 172 nm.

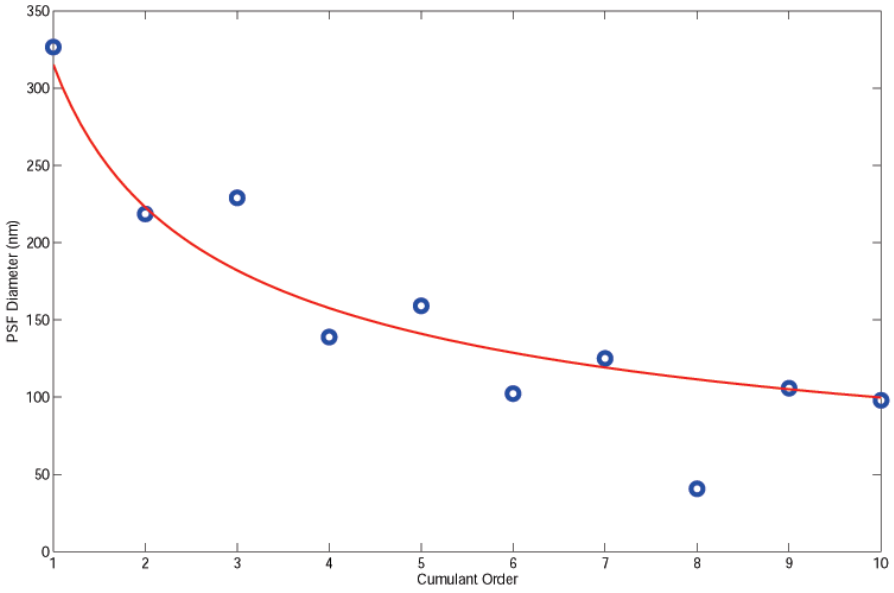

Figure 4.18: Square-root dependence of the width of the Gaussian fit of the PSF with respect to cumulant order. Data fit was binned at 250 μsec. Extrapolation to the original image yields a PSF of 315 nm, which is slightly larger than the expected 250 nm.

CHAPTER V

NOVEL NOBLE METAL FLUOROPHORES: SYNTHESIS AND PHOTOPHYSICAL PROPERTIES

5.1 Introduction

The use of noble metals as fluorophores has increased greatly in recent years [207, 142, 138]. The strong photophysical properties, biocompatability, and unique Raman enhancement all make this class of probes especially intriguing for continued study [208, 209, 154, 153, 210].

Emission from noble metal materials was first observed in the solid state [30, 126, 125]. Efforts to exploit this phenomenon for more widely-applicable fluorescence tags require the compounds are soluble in solution, preferrably water, and several suitable materials to this end have been reported. In each case a scaffold must be employed in order to template and protect the metal clusters from aggregation. Reported scaffolds include extended polymer systems ([31, 154, 211, 152, 212, 213, 214]), nucleic acids ([149, 155, 215, 216]), and peptides ([217, 218]).

Interest in these particles from a fundamental perspective is driven by the extreme influence of size effects on the photophysical properties of the material. These effects are widely known regarding nanoparticles on the tens of nanometeres size scale. Clusters of various sizes have been reported but certain numbers of atoms appear frequently. In the case of dendrimer-encapsulated gold clusters, these "magic number" cluster sizes include Au_5, Au_8, Au_{13}, Au_{23}, and Au_{31} [31]. These cluster sizes can be predicted by the jellium model by treating Au^0 as an analagous atom to Na^0 - both atoms with a single $1s^1$ valence electron. Silver cluster synthesis has produced a range of smaller Ag_N ($N = 2 - 8$) clusters, but without the obvious preferred atom

number seen in gold clusters.

As particles decrease in size below approximately 2 nanometers the continuum of states seen in nanoparticles gives way to the discrete electronic transitions observed in nanoclusters. The broad absorption spectrum seen in nanoparticles yields to well-defined excitation and emission spectra which vary inversely with cluster size. For size-characterized gold clusters this dependence is well-defined, following $E_f/N^{1/3}$, where E_f is the Fermi energy of the material, for small Au_N (N = 3-13) clusters and $E_f/N^{2/3}$ for large (N = 23-38) clusters. The fluorescence quantum yield also scales inversely with cluster size, ranging from 0.7 for Au_5 down to 0.1 for Au_{31}, finally giving way to the very small quantum yield for nanoparticles and bulk metal [207].

The largest amount of synthetic interest has been devoted to glutathione-protected zero-valent gold (Au_nSG_m, SG = glutathione = γ-L-Glutamyl-L-cysteinylglycine) clusters. Following the original work by the Whetten group, many others have used similar techniques to isolate clusters of various sizes, including $Au_{10}SG_{10}$, $Au_{15}SG_{13}$, $Au_{18}SG_{14}$, $Au_{22}SG_{16}$, $Au_{22}SG_{17}$, $Au_{25}SG_{18}$, $Au_{29}SG_{20}$, $Au_{33}SG_{22}$, and $Au_{39}SG_{24}$ [139, 140, 141, 142, 143]. Clusters of similar sizes can also be made by etching from larger clusters and nanoparticles [132, 133, 134, 135, 136, 137, 138]. In both cases, the near-IR emitting $Au_{25}SG_{18}$ was found to be particularly stable. Smaller, water-soluble gold clusters were templated in G4-OH and G2-OH PAMAM (fourth- and second-generation poly(amidoamine) dendrimers) [31, 214]

In a particularly impressive work, the crystal structure of a thiol-protected Au_{25} cluster, $[N(C_8H_{17})_4][Au_{25}(SCH_2CH_2Ph)_{18}]$ was reported [145]. In this cluster a core gold atom is surrounded by 12 more gold atoms forming an icosahedron. This Au_{13} core is protected by a shell of six units of the [-SR-Au-SR-Au-SR-] cyclic polymeric structure (-SR- = SCH_2CH_2Ph) with the gold atoms stellated on the faces of the core icosahedron.

The synthesis and characterization of emissive silver clusters has proven more difficult than the corresponding work with gold. Initial success with dendrimer-protected materials allowed small Ag_n (n = 2-8) clusters that were soluble in aqueous solvents to be synthesized in G4-OH and G2-OH PAMAM. Cluster formation from Ag^+ was initiated with the addition of blue (450-480 nm) light on a microscope slide [154]. Other groups have accomplished similar work with polyacrylate scaffolds and electrons freed by γ-radiation as a reducing agent [152] or UV-radiation upon Ag ions in microgel particles [211].

Future work characterizing and utilizing Ag clusters as novel fluorophores requires a larger amount of sample be prepared than is afforded by these methods. The use of single-stranded DNA as a scaffold for Ag clusters has proven to be effective in producing samples useful for single-molecule biological labels [149, 219, 160, 158]. The specific strand used for templating the DNA controls the nature of the resulting clusters, and therefore the resulting photophysical properties, with high specificity [156, 162]. Unique photophysical properties of these clusters make them particularly suitable as single-molecule labels and are the focus of large amounts of continuing research [155, 164, 165, 159].

An ultimate goal of much of this work is to develop improved fluorophores for single-molecule imaging in live cells. In order to improve the required biocompatability, using peptides as nanocluster scaffolds are an obvious choice. Peptide-templated clusters have been reported by several groups. Strong single-molecule Raman scattering from peptide-templated Ag nanoclusters has been observed, but only on small amounts of photoactivated sample [153]. Extending this to a bulk sample was accomplished by Yu and Dickson [217], where the researchers were able to take inspiration from a long-established technique using $AgNO_3$ as a stain for the nucleolus in fixed cells. They noticed that fluorescence characteristic of silver clusters could be observed in stained cells and were able to use picosecond time-gated imaging to increase the

S/N from sliver clusters over the cell's natural autofluorescence. In addition short peptides were designed, incorporating similar ratios of residues as appear in the nucleolus, allowing bulk fluorescence from silver clusters to be observed with a peptide scaffold. In both of these cases external reducing agents were used to form metallic silver clusters from aqueous ions.

More recently luminescent Au_{25} clusters templated in bovine serum albumin (BSA) were reported [220]. The reduction of Au(III) is accomplished by combining the gold salt and BSA in aqueous solution, then increasing the pH to approximately 12. This reduction at high pH is similar to that used to form large silver nanoparticles from Ag^+ and tyrosine in alkaline solution [221]. At high pH the phenol residue of tyrosine will ionize and subsequently oxidize to a quinone in the presence of a metal ion. It is consistent that the tyrosine residues in BSA would perform as the reducing agent for cluster synthesis at high pH. Further work has identified tyrosine as the most active residue in proteins that template other silver nanomaterials [222].

While many synthesis procedures exist for the creation of noble metal emitters, there still is a large amount of room for improvement. The use of tyrosine as a chemically-switchable reducing agent has been reported; here we report the ability for tyrosine to form emissive silver clusters with the addition of light or heat. In addition, a novel synthesis for an emissive glutathione-protected gold species is reported

5.2 Synthesis

5.2.1 Tyrosine-reduced Silver Clusters

Emissive clusters can be formed in a straightforward manner by simply combining $AgNO_3$ and tyrosine in aqueous solution at 1 mM and illuminating with near UV to green light on a microscope coverslip. Illumination was provided in a widefield manner with a bandpass-filtered mercury lamp with a maximum intensity of approximately 300 W/cm^2. To prevent aggregation, Histidine nonamer (His_9) at the same

concentration was co-dissolved with the silver and tyrosine and photoactivated as above.

Tyrosine-containing peptides were synthesized (Emory University School of Medicine) of several sequences appearing in table 2. Emissive silver particles were created with these peptides in a similar manner as previously mentioned - equal equivalents of Ag^+ and peptide (on a per-tyrosine basis) illuminated on a microscope coverslip. To extend this method to a bulk synthesis, silver ions and peptide (10 mM Ag^+:20 mM Tyrosine) were co-dissolved in deionized water or propionate buffer (50 mM, pH = 4.5) and placed in a quartz cuvette. This solution was placed in front of a bare mercury lamp for several minutes to one hour. The resulting particle solution was used for further analysis.

Fluorophores were synthesized using substituted tyrosines under rapid heating in a microwave reactor. Equal molar amounts of *N*-acetyl tyrosine and silver nitrate were dissolved in a minimum of methanol before drying off the solvent in a microwave reactor tube. The residue was heated to 72 °C in 5 minutes with a 1 minute hold time. The resulting orange crude product was purified with preparatory TLC (90:9:1 CH_2Cl_2:MeOH:Sat.NH_4OH). Final red-emitting product was used for future analysis ($\ll 1\%$ yield). A similar procedure was repeated for *N*-acetyl tyrosine ethyl ester with 50:1 to 80:5 CH_2Cl_2:MeOH for purification of the crude product *via* column chromatography and the desired product yielding green fluorescence under UV excitation.

5.2.2 Glutathione-protected Gold Fluorphores

Water-soluble Au:glutathione fluorophores were created by first co-dissolving a 2:1 ratio of reduced glutathione and $HAuCl_4$ (final concentrations of 2.5 mM and 1.25 mM, respectively, in 50 mL of solution) into an acetate buffer solution (50 mM, pH = 4.7) and stirred in the dark overnight. During this time the yellow solution turns

colorless and subsequently 100 μL of 35% H_2O_2 is added. After several days more of stirring the solution turns yellow once again and is now emits orange under UV excitation. The addition of ethanol will produce a white precipitate that is brightly fluorescent orange under UV excitation. A similar white emissive solid is produced by removing the solvent in the initial reaction mixture. The appearance of a precipitate is common under slightly different synthetic conditions as well and is typically not redissolvable in solution.

5.3 Photophysical Properties

5.3.1 Tyrosine-reduced Silver Clusters

Under constant illumination with UV through green light, the combination of silver ions and tyrosine on a microscope coverslip first yields emissive clusters (see figure 5.1). Continued illumination causes the growth of these clusters into aggregates and then nonemissive nanoparticles. Single-particle Raman is easily observable for particles of this species as one diffuses in and out of a focal spot (figure 5.2).

To prevent the eventual aggregation of the emissive nanoparticles into larger nonemissive structures a stabilizing peptide could be introduced to the solution. The addition of His_9 allows for similar formation of emissive particles as above with delayed aggregation into nonemissive species under continued illumination. The general photophyical properties were unchanged and the single-particle Raman activity is retained. As can be seen in figure 5.3, the characteristics of the Raman spectrum change from particle to particle and even with time on the same particle.

To simplify the synthesis of these protected particles, the tyrosine and protecting peptide were combined into a single peptide. These synthetic peptides were more sucessful in the formation of emissive particles in the bulk. The resulting solutions contained were yellow to brown and turbid, indicating the presence of large particles in solution. These particles could be spun out of solution with gentle centrifigation.

Table 2: Tyrosine-containing peptides for templating the formation of emissive nanoparticles.

Tyrosine-containing peptides			
Name	Sequence	Mass	No. Tyr
Y3Pep3	HDCNKYDYKHDCNKYDYKHDCN	2706.94	4
DHRY3	DHRYDHRYDHRYDHR	2141.21	3
DHY4	DDHHYDHHYDHHYDHHYDD	2573.47	4
Y42XHRP	AHHYAHHYAADYAAHYAAHAAD	2500.59	4
PPPY42XHRE	PPPAHHYAHHYAADYAHHYAHHPPP	2892.13	4
TTTY42XHRE	TTTAHHYAHHYAADYAHHYAHHTTT	2916.06	4
PTY42XHRE	PTPTAHHYAHHYAADYAHHYAHHTPTP	3102.32	4
PTY4HRE	PTPTYAHHYAHHYAADYTPTP	2411.60	4
SGSY42XHRE	SGSAHHYAHHYAADYAHHYAHH	2540.64	4
SGSY4HRE	SGSYAHHYAHHYAADYSGS	2081.12	4

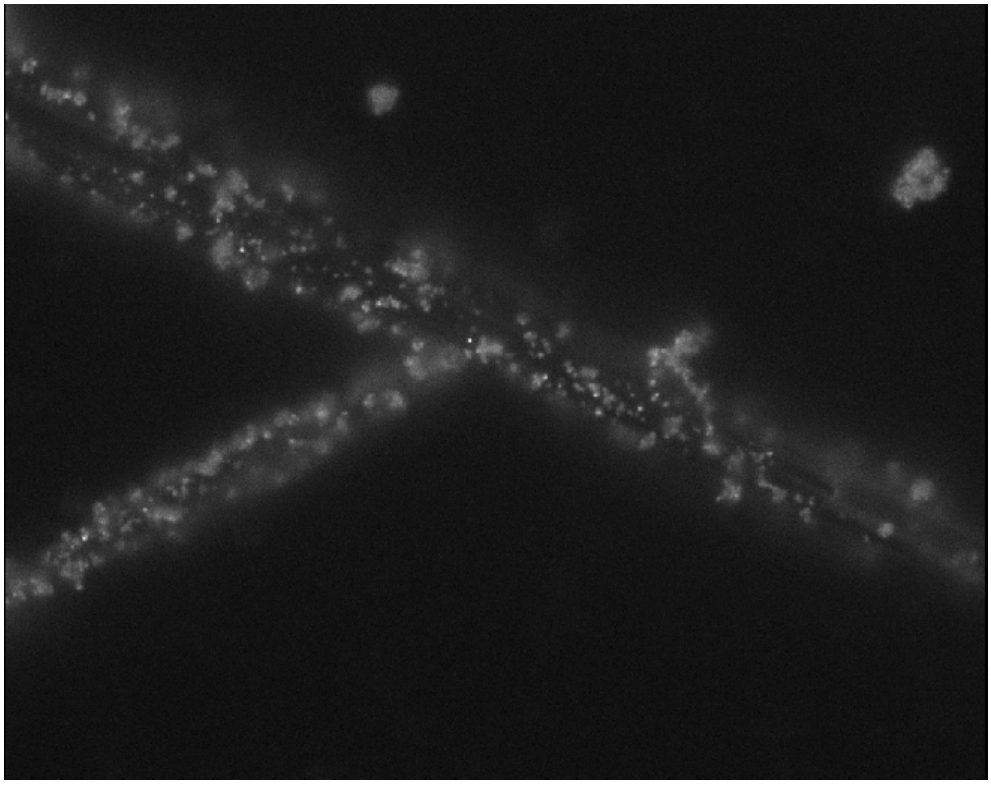

Figure 5.1: Single image of tyrosine-reduced silver fluorescence. Excitation and photoactivation was provided by a green band-passed mercury lamp. The structure observed is an undissolved tyrosine crystal.

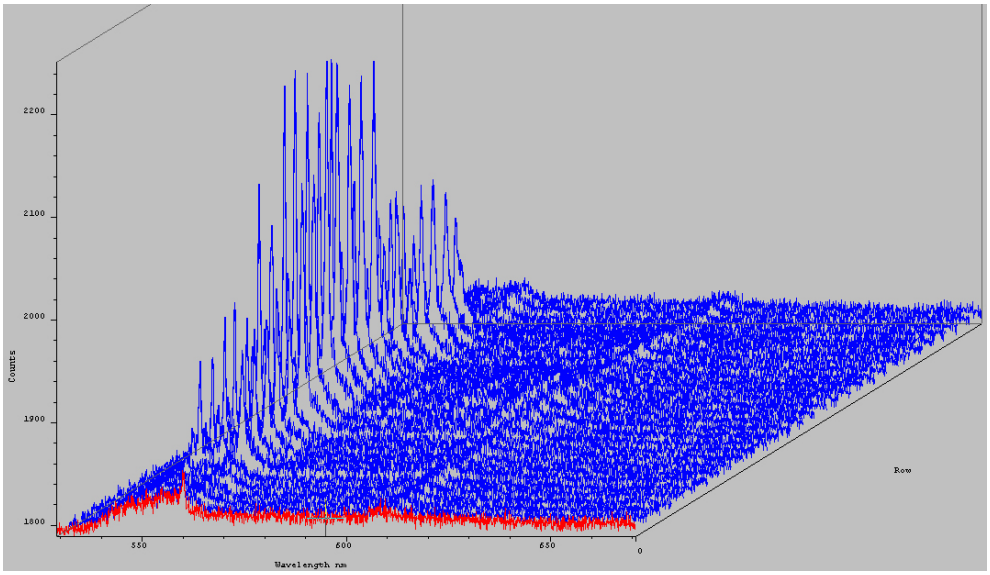

(a)

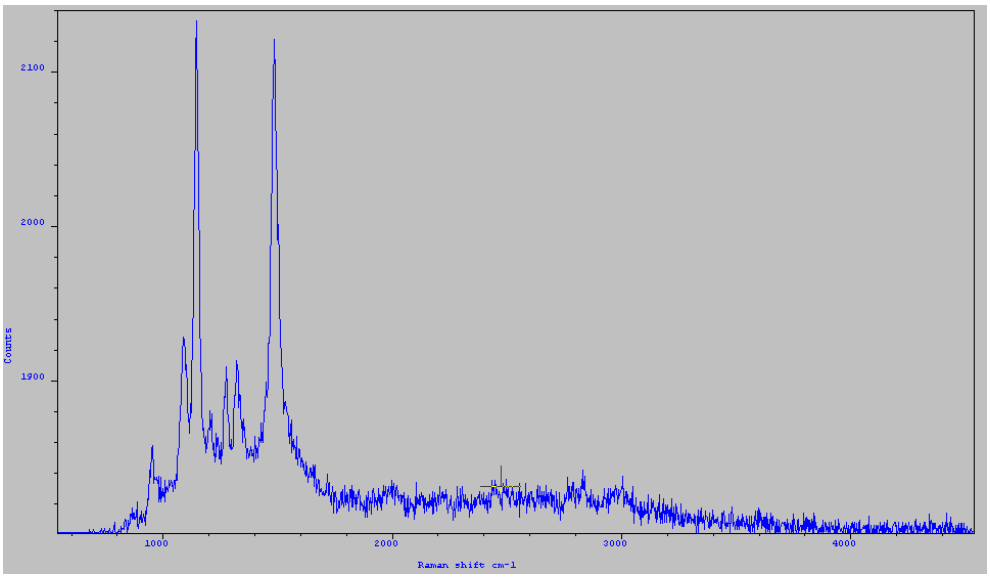

(b)

Figure 5.2: 2(a) A series of Raman spectra of photoactivated tyrosine-silver nanoparticles diffusing through a laser (514.5 nm) focal spot. Spectra were acquired with 100 ms exposure time; 2(b) Single spectrum from 2(a) trace.

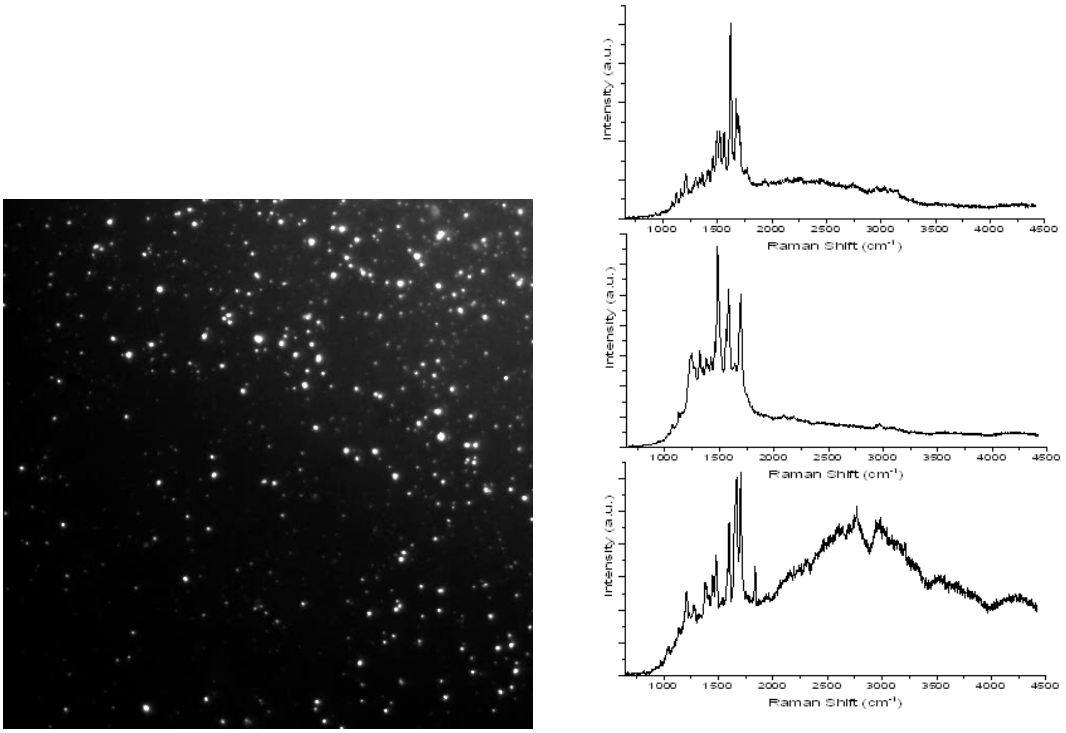

(a) (b)

Figure 5.3: 3(a) Image of emission from His_9-protected silver-tyrosine particles; 3(b) Raman spectra from different particles of same species.

The emissive particles were mostly contained in the centrifuged pellet and very few in the supernatant.

The most productive of the tested peptides was PTY4HRE. Peptide-Ag particles characterized by FCS and DLS indicated an average hydration radius of 10 to 12 nm, but at concentrations of nanomolar or less. Even with these very low concentrations, the particles are sufficiently bright to be easily detectable on the single-particle level. Diffusing particles yielding 1.4 million photons per second were regularly detected in FCS experiments.

Fluorophores synthesized with *N*-acetyl tyrosine showed orange emission with blue excitation when crude. Several fluorescence species could be extracted from this crude product, but the brightest showed sharp emission at 602 nm with excitation of 560 nm (figure 4(a)). A dual-component lifetime of 1.99 ns and 0.73 ns with a fluorescence quantum yield of 2.8% (figure 4(b)). Insufficient product was isolated to continue characterization, but none of the emissive species made in this process would pelletize even when centrifuged at 100,000 x g for one hour.

A similar method with the ethyl ester of *N*-acetyl tyrosine was performed to produce a more organic-soluble mixture of fluorophores. Purification *via* column chromatography was able to separate several different emitters, including the brightest which showed broad green emission (peak = 488 nm) with near-UV (430 nm) excitation. The lifetime with 375 nm excitation was measured as 2.4 ns with an estimated quantum yield of 25% in isopropanol. These quantities are typical of organic fluorophores. This result combined with wet tests cast doubt on the inclusion of silver in the emitter for this and the red-emitting species. Attempts at mass spectroscopy to confirm the presence of silver were inconclusive. While control experiments that omitted the Ag^+ in the synthesis procedure failed to produce similar emissive species, it is quite possible that the silver is simply required for the resulting reaction rather

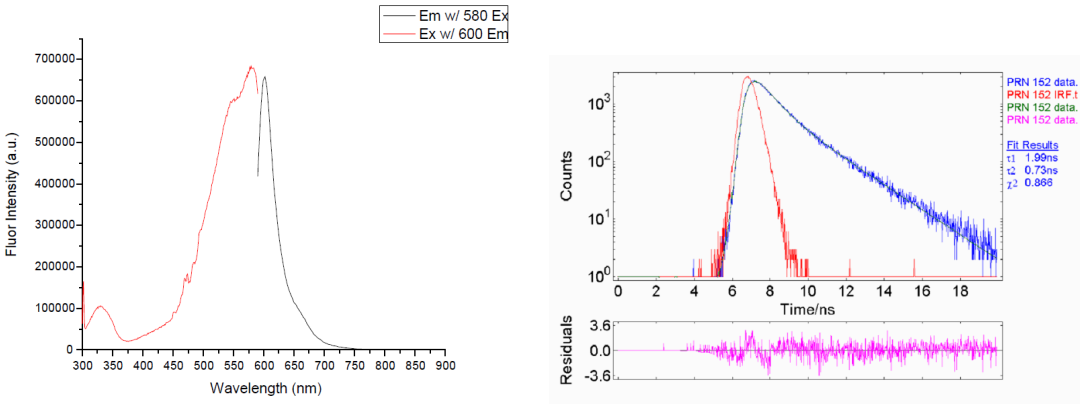

(a) (b)

Figure 5.4: 4(a) Excitation (red) and emission (black) spectra of purified *N*-acetyl tyrosine:Ag fluorophore; 4(b) Lifetime measurement of same species (blue, instrument response red).

than included in the emissive species. While these fluorophores are novel their unremarkable photophysics combined with the difficult and inefficient preparation make them less than ideal for future investigation as single-molecule fluorophores.

5.3.2 Glutathione-protected Gold Fluorophores

The weakly fluorescent gold-glutathione complex showed a maximum emission at approximately 605 nm with peak excitation at 405 nm. This excitation corresponds closely, but not exactly to a shoulder that grows in the absorbance spectrum centered around 375 nm. The emission for this species is largely on the hundreds of nanoseconds timescale, although with some shorter-time contributions. This long-lived excited state, combined with the low (approximately 2%) quantum yield limits the emission rate of this fluorophore.

Addition of a reducing agent, such as sodium borohydride ($NaBH_4$) to an emissive gold-glutathione solution immediately results in a nonemissive black precipitate. The optimum ratio of Au(III) and glutathione starting material was found to be 2 equivalents of glutathione for every gold ion, resulting in the net oxidation state of the gold ions being Au(I). The photophysical properties are too consistent with other

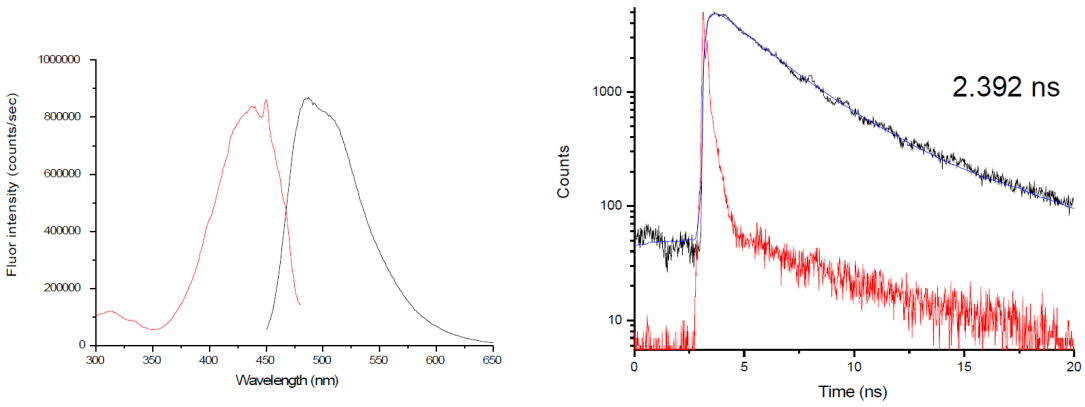

(a) (b)

Figure 5.5: 5(a) Excitation (red) and emission (black) spectra of purified *N*-acetyl tyrosine ethyl ester:Ag fluorophore; 5(b) Lifetime measurement of same species (black, instrument response red).

Au(I) complexes reported in the literature to ignore, implying that the true nature of the fluorophore is a Au(I) complex [223].

Previous work by members of this group have reported the synthesis of these same glutathione-protected gold fluorophores [224]. Attempts to reproduce this work were met with difficulty as the reaction readily forms a precipitate under neutral pH conditions called for. Repeated washings following centrifugation (up to 20 times) to generate a soluble fluorophore proved fruitless. In fact most attempts at redissolution of the white fluorescent solid that readily forms in these reactions were unsuccessful without destruction of the fluorescence. The times that redissolution of the solid was possible it was not possible to reproduce the success. Also reported in the previous work by others in this group was the ability to tune the emission color by way of altering the Au:Glutathione ratio in the synthesis. This was not observed. However, a correlation between the peak emission wavelength and the ratio of oxidized and reduced glutathione used in the synthesis procedure published here was observed.

Later communications have indicated that the use of a 1:1 ratio of Au:Glutathione

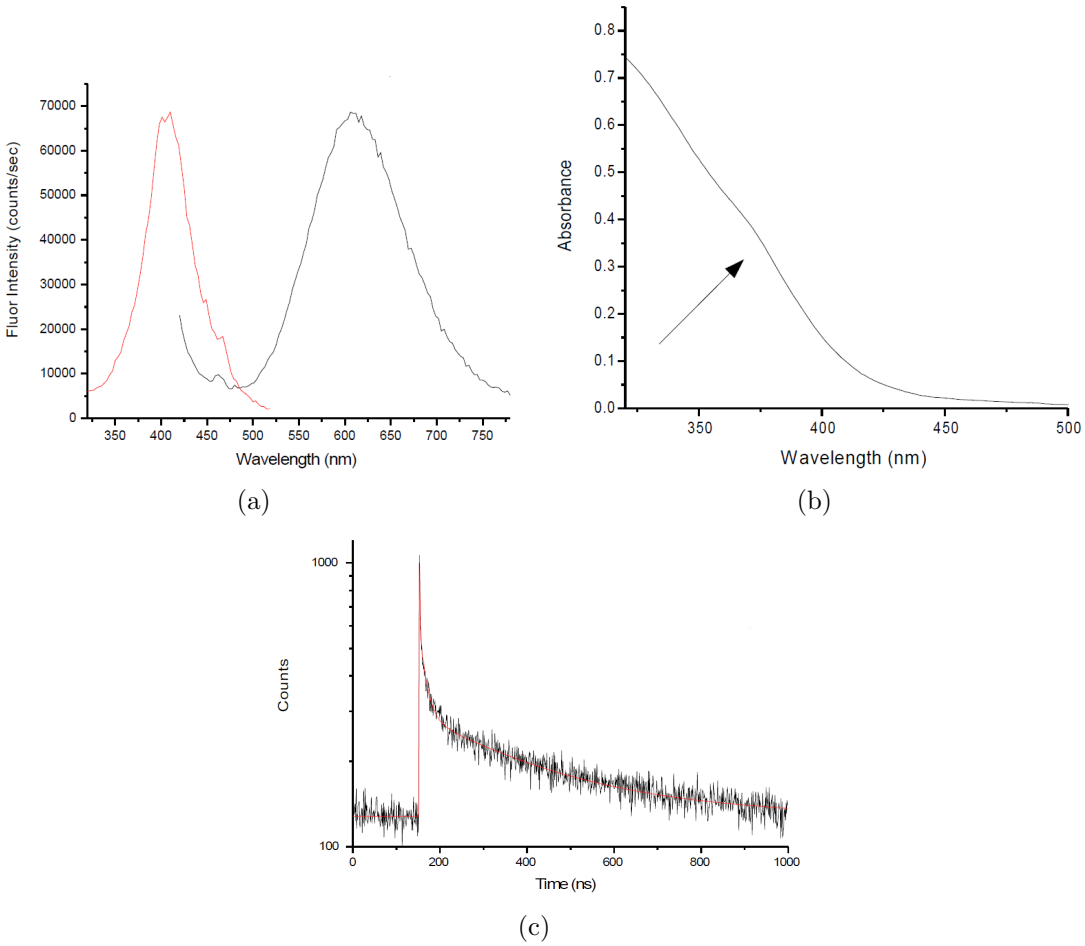

Figure 5.6: 6(a) Excitation (red) and emission (black) spectra of Au-glutathione fluorophore solution; 6(b) Absorbance spectrum of same solution. Arrow indicates shoulder in absorbance spectrum that grows in with emission intensity; 6(c) Lifetime measurement of same species (data black, fit red). Fit is with three exponentials of time (percent contribution) of 290 ns (87%), 18 ns (10%), and 0.6 ns (3%).

in the reaction mixture instead of the 1:2 ratio indicated previously is more successful at preventing the formation of precipitates and subsequently increased fluorescent yield. Emissive solutions synthesized in this manner - 50 μM solution of each $HAuCl_4$ and reduced glutathione stirred for several days in the light - show similar but not identical photophysical characteristics as the solutions prepared through the method above employing hydrogen peroxide. The most striking differences are a significantly increased contribution of the long lifetime component in the peroxide-utilizing emitters as well as an increased quantum yield in these solutions (0.06 as opposed to 0.001 for the alternate synthesis).

Overall, while the synthesis procedure for Au:Glutathione emitters is straightforward, the results are highly variable from reaction to reaction (contrast results in figures 5.6, 5.7, and 5.8). Continuing work to decode the true nature of these emitters and optimization of the synthesis procedure remains to be done.

5.4 Conclusions

This work has presented several novel flourophores dependent on noble metals for their emissive properties. The brightest of these, the peptide-supported silver nanoparticles, shows the most potential promise as a single-particle probe. The heavy atoms present in these and the other fluorophores reported in this work allow for their use as multimodal labels, with applications in X-ray fluorescence, CT, or electron microscopy as well as fluorescence. While the large size of this emitter makes it less than ideal for future single-molecule applications, such as protein tracking in live cells, the extremely bright emission and intense Raman signal hold promise for this species in situations where very small size is not of major importance.

Fluorophores created through the solid-state reaction of silver with tyrosine derivatives are as of yet unresolved with respect to their true chemical nature. While the emission is not bright enough to warrant further inquiry for the application of these

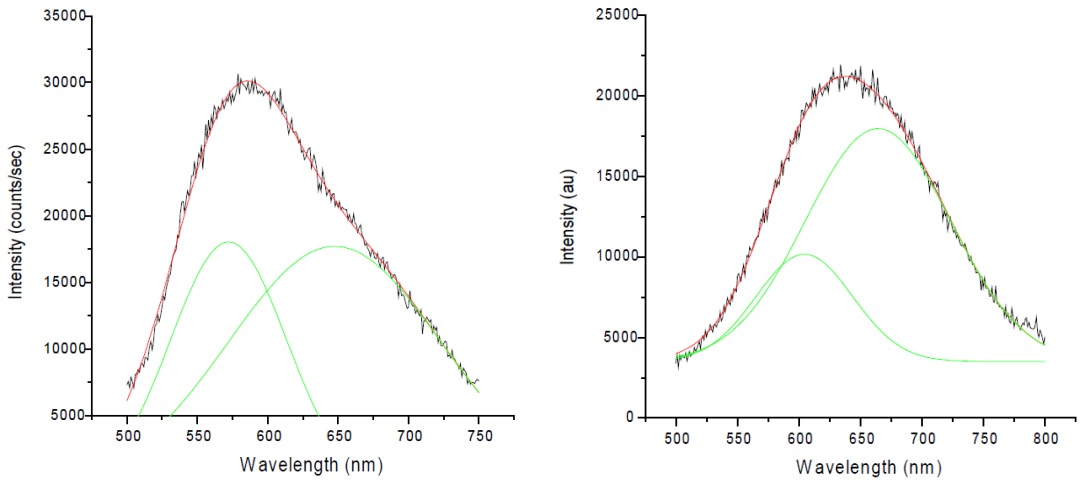

(a) (b)

Figure 5.7: 7(a) Emission spectrum under 410 nm excitation of Au:Glutathione prepared in the absence of hydrogen peroxide by the method recently reported by Jie Zheng. The green lines indcate a 2-component Gaussian fit with (center (nm)/width (nm)/amplitude (counts)) of left - (572/82/2.0 x 10^6) and right - (647/151/3.5 x 10^6).; 7(b) Emission spectrum under 400 nm excitation of Au:Glutathione prepared in the presence of hydrogen peroxide by the method reported here. The green lines indcate a 2-component Gaussian fit with (center (nm)/width (nm)/amplitude (counts)) of left - (604/78/6.5 x 10^5) and right - (664/118/2.1 x 10^6).

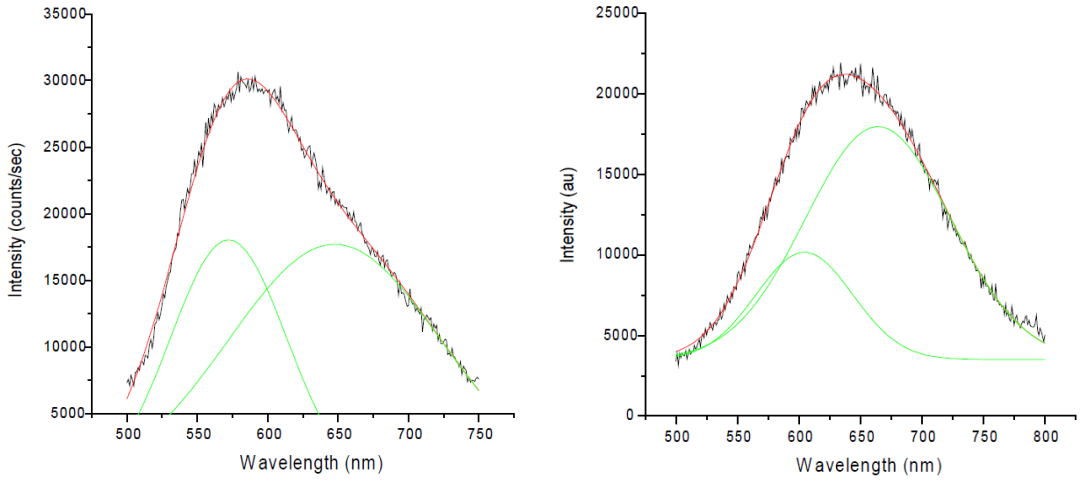

(a) (b)

Figure 5.8: 8(a) Lifetime measurements under 375 nm excitation of Au:Glutathione prepared in the absence of hydrogen peroxide by the method recently reported by Jie Zheng. The deconvoluted data (green) was fit to a 4-component fit with lifetimes (weights) of 11.27 ns (0.74), 68.64 ns (0.20), 302.9 ns (0.049) and 1236.1 ns (0.011); 8(b) Lifetime measurements under 375 nm excitation of Au:Glutathione prepared in the presence of hydrogen peroxide as reported in this work. The deconvoluted data (green) was fit to a 3-component fit with lifetimes (weights) of 23.8 ns (0.49), 189 ns (0.31), and 1204.4 ns (0.20)

species as single-molecule probes, the uncommon method of their preparation does make them interesting from a chemical standpoint.

The brightness of gold-glutathione emitters are largely limited by their long lifetimes and low quantum yields. However, the combination of fluorescence and heavy atoms make these species as possible dual-purpose labels for both fluorescence and x-ray imaging or electron microscopy due to the inclusion of the massive gold atoms in the fluorophore.

CHAPTER VI

CONCLUSIONS AND OUTLOOK

This thesis presents a novel method for utilizing fluorescence fluctuations in a widefield geometry for the purposes of flow vector mapping fully in three dimensions. As well, extensions of this technique for widefield signal extraction of fluorescently modulatable fluorophores and single-point super-resolution microscopy through higher-order statistical analysis have been discussed. The common theme of this work is utilizing the information contained in time series data at unique spatial positions to yield properties regarding a range of experimental systems. These techniques have been demostrated on model systems but are easily adaptable for use in device processing or biophysical applications.

6.1 Widefield Cross-correlation Spectroscopy for Flow Imaging

6.1.1 Major findings

Novel methods for determining flow vectors through pixel-pair cross-correlation analysis have been presented. With the use of a Nipkow Disk Confocal Scanner, flow vectors in both planar and axial directions were determined. This method demonstrated a large tolerance for noise in the input signal, indicating a capacity for small, dim, and fast-moving particles to be used as fluorescent tracers. A S/N value as low as 1.4 for simulated flow will yield an excellent flow map with sufficent number of frames. Flow speeds in excess of 10 mm/sec can be measured with this method under appropriate experimental conditions. Particles as small as single antibodies with hydration radii of 15 nm have been shown to be effective tracer particles.

6.1.2 Outlook

Due to the generality of this flow-mapping method, a very broad range of systems can be analyzed with the method presented here. The only contstraint on the input for the analysis is that it be video data with particle motion producing a fluctuation in the time series. While flow in microfluidic channels was used as a model system for the work presented, motion in biological systems such as vesicle tracking in neurons, blood flow, or diffusion in membranes can be analyzed with trivial modifications to the analysis algorithm. The incorporation of an analysis functionality for axial motion allows for the quantification of motion out of the focal plane which becomes vital in complex three-dimensional systems. Because of these advantages the cross-correlation time series analysis method presented here represents a valuable alternative to popular particle tracking techniques for quantifying microscopic motion.

6.2 Advanced Widefield Confocal Microscopy - Signal Extraction and Super-resolution Imaging

6.2.1 Major findings

The nature of widefield confocal microscopy lends itself to utilization in sophisticated ways in addition to flow mapping. With the incorporation of optically modulatable fluorophores, a novel incorporation with polystyrene beads presented here, the species of interest can be extracted over a high scattering and non-modulatable fluorescent background signal. The subsequent demodulation of a modulated image stack can selectively yield an enhanced signal over an obscuring, constant fluorescent background. In addition, a method for selectively enhancing a modulated fluorescence signal in TC-SPC data has been presented which can allow for selective study of fluorophores of interest with high temporal resolution.

With the use of higher-order statistical analysis on asynchronous time data it has been demonstrated that super-resolution images can be extracted from data collected

in a standard confocal microscope. The use of single-photon counting detectors with high temporal resolution allows the stochastic blinking of single dye molecules to be used as the fluorescence fluctuations fundamental to this technique. As a result, emitters with spacing on the order of the width of the point-spread function can be resolved with sufficiently high cumulant order. These results have been demonstrated with image simulations as well as experimentally, where the microsecond blinking dynamics of DNA:Ag nanoclusters has been used in conjunction with higher-order statistical analysis to generate super-resolution confocal images.

6.2.2 Outlook

As imaging techniques in biological systems continue to become more and more advanced, the techniques presented here will increase in importance. The large amount of constant fluorescent background present in biological samples has long plagued the use of single-molecule techniques in cells. The use of fluorescence modulation to enhance the signal from a fluorophore of interest can largely overcome this obstacle. The utilization of super-resolution microscopy in all of its various forms continues to grow every year. The technique presented here allows for super-resolution images to be obtained without strict constraints on experimental setup or fluorophore selection as many of the other methods demand. As such the work here should be readily extendable to generating super-resolution images in biological samples with only small modifications to existing techniques.

6.3 Novel Noble Metal Fluorophores

6.3.1 Major findings

This work has presented several novel flourophores dependent on noble metals for their emissive properties. The brightest of these, the peptide-supported silver nanoparticles, shows the most potential promise as a single-particle probe. These particles

show very bright emission on the single-particle level with Raman enhancement visible even in diffusing single particles. The family of fluorophores created in the solid-state reaction of silver and several tyrosine derivatives are intrigueing from a chemical standpoint and do offer a range of photophysical properties. The presented scheme for producing water-soluble gold-glutathione fluorophores is novel and offers an alternative to published methods for producing gold-centered fluorescence.

6.3.2 Outlook

While the fluorophores that appear in this work are novel and cover a wide range of photophysical and chemical variety, none have proven to be a perfect single molecule dye. The most promising, the peptide-supported silver clusters, can have potential uses as a Raman tag or genetically-encoded fluorophore for live-cell labelling. However, the large size of the particles synthesized to this point limits their use as probes for dynamic processes. Still there exist a large number of applications where extreme brightness is more essential than small size and these particles would be excellent candidates for such work. In addition, the gold-glutathione particles hold promise as dual-purpose probes for fluorescence and x-ray imaging.

6.4 Widefield Cross-correlation Spectroscopy

As microscopy techniques become more advanced, the subsequent techniques in data analysis must also continue to improve. Here has been presented novel methods for analyzing image stacks as a collection of spatially-distrubuted time series data in conjuction with correlations to yield a wide variety of results. These methods can be easily adapted to operate on a wide range of experimental systems, including live cells or whole organisms. With the increased used of such advanced image analysis techniques it is hoped that long-held secrets in microscopic phenomena can be revealed.

APPENDIX A

DERIVATION OF FLUORESCENCE CORRELATION SPECTROSCOPY EXPRESSIONS

A.1 General Form of the Correlation Function

For a stationary random process, such as a fluorescence signal, $F(t)$, the process can be described as zero-mean fluctuations about a constant average value (equation 53).

$$F(t) = \langle F \rangle + \delta F(t) \tag{53}$$

$$\text{where } \langle \delta F(t) \rangle = 0 \tag{54}$$

The brackets here indicate an ensemble average. The correlation between the fluorescence signal at some time $F(t_1)$ and at another time $F(t_2)$ is given as

$$g(t_1, t_2) = \langle F(t_1)\, F(t_2) \rangle. \tag{55}$$

Because the signal is about a constant mean, the difference between t_1 and t_2 is important, rather than their absolute values. As such, the correlation function can be written as

$$g(\tau) = \langle F(t)\, F(t+\tau) \rangle \tag{56}$$

which, combined with equation 53, yields

$$g(\tau) = \langle F \rangle^2 + \langle \delta F(t+\tau)\, F(t) \rangle. \tag{57}$$

In a system such as seen in fluorescence correlation spectroscopy the ensemble average (the average over all molecules) can be replaced by the time average (average over all

of time). It is convenient to deal with the normalized correlation function, which is defined in equation 58.

$$G(\tau) = \frac{g(\tau)}{\langle F \rangle^2} - 1 = \frac{\langle \delta F(t+\tau)\, F(t) \rangle}{\langle F \rangle^2} \tag{58}$$

The finite and stochastic lifetime of the fluorophores ensures that the fluorescence radiation is incoherent. As a result, fluctuation in the fluorescence signal is proportional to the product of the fluctuation of fluorophore concentration, $\delta C(t, \mathbf{r})$, and the time-independent molecular detection profile, $W(\mathbf{r})$, such that $\delta F(t, \mathbf{r}) \propto \delta C(t, \mathbf{r}) * W(\mathbf{r})$, and the total fluorescence signal can be written as a sum over all emitters. Here the vector $\mathbf{r}$ indicates a position (x, y, z) in space. The molecular detection profile is the product of the intensity profile, $I(\mathbf{r})$, and the detection efficiency parameter, κ ($W(\mathbf{r}) = \kappa\, I(\mathbf{r})$). This parameter κ combines the quantum yield and extinction coefficient of the fluorophore as well as the quantum efficiency of the photodetector and is assumed to be invariant in both space and time. In addition this value is cancelled out in the normalization indicating that the normalized fluorescence correlation function is independent of molecular parameters. The concentration fluctuation can be written in a manner analogous to the fluorescence fluctuation equation, 53, such that

$$C(t, \mathbf{r}) = \langle C \rangle + \delta C(t, \mathbf{r}). \tag{59}$$

The time-dependent fluorescence signal can be written as

$$F(t) = \kappa \int I(\mathbf{r}) \left(\langle C \rangle + \delta C(t, \mathbf{r}) \right) d\mathbf{r} \tag{60}$$

For the cases covered here, it is mathematically and experimentally appropriate to treat the intensity profiles as three-dimensional Gaussians with lateral dimensions $\rho = (x, y)$ and axial dimensions z

$$I(\mathbf{r}) = I_o \, exp\left[\frac{\rho^2}{2\,\omega_{xy}}\right] \, exp\left[\frac{z^2}{2\,\omega_z^2}\right] \tag{61}$$

where ω_{xy} and ω_z are the dimensions of the Gaussian in the lateral and axial directions, respectively [34]. The axial vector is colinear with the light propogation vector from the objective while the planar coordinate plane is perpendicular to the propgation vector.

The fluorescence fluctuations are in now in terms of concentration fluctuations, so it is necessary to define the concentration correlation function, $\Phi(\mathbf{r}, \mathbf{r}', \tau)$, which describes the correlation between the concentration at point $\mathbf{r}$ and some other point $\mathbf{r}'$ separated in time τ.

$$\Phi(\mathbf{r}, \mathbf{r}', \tau) = \langle \delta C(t, \mathbf{r}) \, \delta C(t + \tau, \mathbf{r}') \rangle \tag{62}$$

The normalized correlation function (equation 58) in terms of the molecular detection profile and correlation cross-correlation is given as

$$G(\tau) = \frac{\iint I(\mathbf{r}) \, I(\mathbf{r}') \, \Phi(\mathbf{r}, \mathbf{r}', \tau) \, d\mathbf{r} d\mathbf{r}'}{\langle C \rangle^2 \int I(\mathbf{r}) \, d\mathbf{r} \int I(\mathbf{r}') \, d\mathbf{r}'} \tag{63}$$

.

Equation 63, with knowledge of the expression of the concentration correlation expression as well as the intensity profile, can be used to generate the normalized correlation function for any general system giving rise to fluorescence fluctuations.

A.2 The Concentration Correlation Expression

From the general form of the concentration correlation expression (equation 62) there exist many solutions depending on the experimental parameters giving rise to the concentration fluctuations. For the case of isotropic diffusion, the concentration fluctuations satisfy the diffusion equation

$$\frac{\partial}{\partial t}\delta C(t,\mathbf{r}) = D\nabla^2\delta C(t,\mathbf{r}) \tag{64}$$

where D is the diffusion constant and ∇^2 the Laplace operator [191, 57]. A solution of this partial differential equation can be expressed as

$$\delta C(t,\mathbf{r}) = \int \delta C(0,\mathbf{r}')\,\mathcal{G}\left(t,\mathbf{r}|0,\mathbf{r}'\right)\,d\mathbf{r}' \tag{65}$$

where $\mathcal{G}\left(t,\mathbf{r}|0,\mathbf{r}'\right)$ is the Green's function of equation 64. The Green's function of the diffusion equation yields the form for the concentration correlation equation seen in equation 66

$$\langle \delta C(t,\mathbf{r})\,\delta C(t+\tau,\mathbf{r}')\rangle = \int \langle \delta C(0,\mathbf{r})\,\delta C(0,\mathbf{r}')\rangle\,\mathcal{G}\left(t,\mathbf{r}|0,\mathbf{r}'\right)d\mathbf{r}. \tag{66}$$

For randomly distributed fluorophores, as is seen in experiments here, the concentrations of the particles at two different locations at the same time are uncorrelated, such that equation 67 holds. As well, since the concentration of fluorophores is low, the motion of one particle does not affect the others and the number of particles in a volume is Poissonian, such that equation 68 also holds.

$$\delta C(0,\mathbf{r})\,\delta C(0,\mathbf{r}')\rangle = \rangle \delta C^2\rangle\,\delta(\mathbf{r}-\mathbf{r}') \tag{67}$$

$$\langle \delta C^2\rangle = \langle C\rangle \tag{68}$$

The combination of the previous three equations yields equation 69

$$\langle \delta C(t,\mathbf{r})\,\delta C(t+\tau,\mathbf{r}')\rangle = \langle C\rangle\,\mathcal{G}\left(t,\mathbf{r}|0,\mathbf{r}'\right) \tag{69}$$

As such the correlation function 63 can be expressed in terms of the Green's function (equation 70).

$$G(\tau) = \frac{\iint I(\mathbf{r})\, I(\mathbf{r}')\, \mathcal{G}\left(t, \mathbf{r}|0, \mathbf{r}'\right)\, d\mathbf{r} d\mathbf{r}'}{\langle C \rangle \int I(\mathbf{r})\, d\mathbf{r} \int I(\mathbf{r}')\, d\mathbf{r}'} \tag{70}$$

The exact form of the Green's function with vary depending on the experimental situation and three cases for the diffusion autocorrelation, fluorophore blinking, and flow cross-correlation function appear separately below.

A.3 Derivation of Diffusion Autocorrelation Function

A solution to the Green's equation for homogeneous, uniform diffusion in three dimensions through a small focal volume in a space with infinitely distant boundries appears in equation 71 [57].

$$\mathcal{G}\left(\tau, \mathbf{r}|0, \mathbf{r}'\right) = (4\pi D\tau)^2\, exp\left[-\frac{|\vec{R}|^2}{4D\tau}\right] \tag{71}$$

Here $|\vec{R}|$ signifies the length of the vector $\vec{R}$ that connects the two focal volumes at positions $\mathbf{r}$ and $\mathbf{r}'$ [225]. It can be seen that the solution does not depend on the absolute coordinates but rather only the distance between the two focal volumes. In the case of a single-point FCS experiment $\mathbf{r} = \mathbf{r}'$, and as such the exponential is reduced to 1. Evaluation of the integrals in equation 70 with the remaining portion of the solution for the Green's function in equation 71 yields the form of the diffusion autocorrelation (equation 72).

$$G_{ac}(\tau) = \frac{1}{N} \frac{1}{1 + \frac{\tau}{\tau_D}} \left(1 + \frac{\tau}{\omega_o^2\, \tau_D}\right)^{-\frac{1}{2}} \tag{72}$$

Here τ_D is the diffusion timescale, defined as $\omega_{xy}/4D$, where D is the diffusion constant, and $\omega_o = \omega_{xy}/\omega_z$, or the aspect ratio of the ellipsoidal focal volume, and N is the average number of emissive particles per focal volume over the measurement period. The implementation of this equation appears chapter 2.6.

A.4 Derivation of the Blinking Autocorrelation Function

Fluorophore blinking can be thought of as an extension of a two-state first-order unimolecular chemical reaction between A_{on} and A_{off} as shown in equation 73.

$$A_{on} \underset{k_{off}}{\overset{k_{on}}{\rightleftharpoons}} A_{off} \tag{73}$$

Here the rate coefficient to go from the on to the off state is given a k_{on} and the reverse as k_{off}. It is assumed that only the on state of the molecule is emissive. This reaction typically occurs on a much faster timescale than does molecular diffusion such that it is possible, with a sufficiently fast detector, to observe both processes in an autocorrelation function. Here the concern is only the blinking timescales of the transition in immobilized molecules in a single illumination point. As such a system of differential equations for the concentrations of the on and off molecules, respectively, are given in equations 74 and 75.

$$\frac{\partial}{\partial t} C_{on}(t, \mathbf{r}) = k_{on} C_{off}(t, \mathbf{r}) - k_{off} C_{on}(t, \mathbf{r}) \tag{74}$$

$$\frac{\partial}{\partial t} C_{off}(t, \mathbf{r}) = k_{off} C_{on}(t, \mathbf{r}) - k_{on} C_{off}(t, \mathbf{r}) \tag{75}$$

This expression, through a method analogous to the one above for the diffusion autocorrelation, gives rise to the blinking autocorrelation in equation 76 [58, 225].

$$G(\tau) = \frac{1}{N} \frac{f_{off}}{1 - f_{off}} exp\left(-\frac{\tau}{\tau_{Blink}}\right) + 1 \tag{76}$$

where f_{off} is the fraction of the N molecules in the focal volume that are in the dark state and τ_{Blink} the timescale for the blinking process. The rate coefficients k_{on} and k_{off} can be deduced from the autocorrelation by equations 77 and 78.

$$f_{off} = \frac{k_{off}}{k_{off} + k_{on}} \tag{77}$$

$$\tau_{Blink} = \frac{1}{k_{off} + k_{on}} \tag{78}$$

Implementation of these equations for SOFI imaging occurs on surfaces where molecular overlap is possible. The rate coefficients are of little concern - rather the magnitude and timescale of the autocorrelation function are necessary for analysis. As such, the coefficient for the exponential is collected in a single constant when utilized in chapter 4.3.

A.5 Derivation of 3-D Flow Cross-correlation Function

For flow an additional term is added to the diffusion function, giving rise to the form of the concentration correlation function seen in equation 7 of reference [21] and equation 79 here.

$$\frac{\partial}{\partial t}\delta C(t, \mathbf{r}) = D\nabla^2 \delta C(t, \mathbf{r}) - \vec{V}\nabla\delta C(t, \mathbf{r}) \tag{79}$$

The symbol ∇ signifies the Nabla operator and ∇^2 the Laplace operator. The vector $\vec{V}$ is the flow vector representing the displacement due to flow over the measurement space. Because the cross-correlation in utilized here the flow is assumed to be of constant velocity over the space encompassing the two focal volumes. The two focal volumes are connected by vector $\vec{R}$ with amplitude R and angle α relative to the flow vector. The three-dimensional case of diffusion and flow appears immediately below and the strictly in-plane case following.

The cross-correlation function for a system undergoing diffusion and flow in three dimensions is given by Brinkmeier *et. al.* (equation 8 therein) [21].

$$G_{cc}(\tau) = \left[N\left(1+\frac{\tau}{\tau_D}\right)\sqrt{1+\frac{\omega_{xy}^2\,\tau}{z_o^2\,\tau_D}}\right]^{-1} exp\left[-\frac{1}{\omega_{xy}^2}\frac{\left(\vec{V_\rho}\,\tau-\vec{R_\rho}\right)^2}{1+\frac{\tau}{\tau_D}}-\frac{1}{z_o^2}\frac{\left(\vec{V_z}\,\tau-\vec{R_z}\right)^2}{1+\left(\frac{\omega_{xy}^2\,\tau}{z_o^2\,\tau_D}\right)}\right] \tag{80}$$

Separating this function into planar and axial components requires the following definitions:

$$\rho = \text{planar quantity} \tag{81a}$$

$$z = \text{axial quantity} \tag{81b}$$

$$\gamma = \text{arbitrary quantity} \tag{81c}$$

$$\theta = \text{planar flow angle between } \vec{R_x} \text{ and } \vec{R_y} \tag{81d}$$

$$\phi = \text{axial flow angle between } \vec{R_z} \text{ and } \vec{R_\rho} \tag{81e}$$

$$\tau_{F,\gamma} = \frac{|\vec{R_\gamma}|}{|\vec{V_\gamma}|} \tag{81f}$$

The separated form of equation 80 becomes:

$$G_{cc}(\tau) = \left[N\left(1+\frac{\tau}{\tau_D}\right)\sqrt{1+\frac{\omega_{xy}^2\,\tau}{z_o^2\,\tau_D}}\right]^{-1} exp\left[-\frac{1}{\omega_{xy}^2}\frac{\left(\vec{V_\rho}\,\tau-\vec{R_\rho}\right)^2}{1+\frac{\tau}{\tau_D}}\right] exp\left[-\frac{1}{z_o^2}\frac{\left(\vec{V_z}\,\tau-\vec{R_z}\right)^2}{1+\left(\frac{\omega_{xy}^2\,\tau}{z_o^2\,\tau_D}\right)}\right] \tag{82}$$

This function serves as the basis of the later cross-correlation and autocorrelation functions.

Now in the limit of zero diffusion ($\tau_D \to \infty$) and in terms of $\tau_{F,\gamma}, \vec{R_\gamma}, \theta$, and ϕ

$$G_{cc}(\tau) = \frac{1}{N}\,exp\left[-\frac{|\vec{R_\rho}|}{\omega_{xy}^2}\left(\frac{\tau^2}{\tau_{F,\rho}^2}+1-2\frac{\tau}{\tau_{F,\rho}}\,cos\,\theta\right)\right] exp\left[-\frac{|\vec{R_z}|}{z_o^2}\left(\frac{\tau^2}{\tau_{F,z}^2}+1-2\frac{\tau}{\tau_{F,z}}\,cos\,\phi\right)\right] \tag{83}$$

The derivative of equation 83 with respect to τ yields equation 85

$$G_{cc}(\tau) = \frac{1}{N}\, exp\left[-\frac{|\vec{R_\rho}|}{\omega_{xy}^2}\left(\frac{\tau^2}{\tau_{F,\rho}^2} + 1 + 2\,\tau\,\tau_{F,\rho}\, cos\,\theta\right)\right] * \tag{84}$$
$$exp\left[-\frac{|\vec{R_z}|}{z_o^2}\left(\frac{\tau^2}{\tau_{F,z}^2} + 1 + 2\,\tau\,\tau_{F,z}\, cos\,\phi\right)\right]$$
$$* \left[-\frac{|\vec{R_\rho}|}{\omega_{xy}^2}\left(\frac{2\,\tau}{\tau_{F,\rho}^2} - \frac{2\,cos\,\theta}{\tau_{F,\rho}}\right)\right] * \left[-\frac{|\vec{R_z}|}{z_o^2}\left(\frac{2\,\tau}{\tau_{F,z}^2} - \frac{2\,cos\,\phi}{\tau_{F,z}}\right)\right]$$

The exponental portion of equation 85 cannot be equal to zero, so only the remaining portion will yield a solution when solving for the peak position.

$$0 = \left[-\frac{|\vec{R_\rho}|}{\omega_{xy}^2}\left(\frac{2\,\tau}{\tau_{F,\rho}^2} - \frac{2\,cos\,\theta}{\tau_{F,\rho}}\right)\right] * \left[-\frac{|\vec{R_z}|}{z_o^2}\left(\frac{2\,\tau}{\tau_{F,z}^2} - \frac{2\,cos\,\phi}{\tau_{F,z}}\right)\right] \tag{85}$$

which has solutions at

$$\tau = \tau_{F,\rho}\, cos\,\theta \tag{86}$$

$$\tau = \tau_{F,z}\, cos\,\phi \tag{87}$$

Substituting the solutions into appropriate variables yields the final form of the amplitude dependence of the three-dimensional cross-correlation. Here, $|\vec{R_\rho}|$ and $|\vec{R_z}|$ are replaced with the later-used R_{planar} and R_{axial}. The contribution to N has been split into axial (N_{xy}) and planar (N_z) portions. For consistiency with later nomenclature $z_o = \omega_z$.

$$G(t_{Max}) = \frac{1}{N_{xy}} exp\left[-\frac{R_{planar}^2}{\omega_{xy}}\, sin^2\,\theta\right] * \frac{1}{N_z} exp\left[-\frac{R_{axial}^2}{\omega_z}\, sin^2\,\phi\right] \tag{88}$$

A.6 Dependence of Cross-correlation Peak Position on Angle

For the in-plane flow case, where $\tau_{Flow} \ll \tau_D$ and axial flow is insignificant, the cross-correlation between two points separated by distance $R = |\vec{R}|$ and angle α between the flow vector and spacing vector is equation 89, derived from equation 80.

$$G_{cc}(\tau) = \frac{1}{N} exp\left[-\frac{R^2}{{\omega_o}^2}\left(\frac{\tau^2}{{\tau_{Flow}}^2} + 1 - 2\frac{\tau}{\tau_{Flow}}\right) cos\,\alpha\right] \tag{89}$$

and taking the derivative with respect to time τ in order to find the position of the peak maximum

$$\frac{d\,G_{cc}(\tau)}{d\,\tau} = \frac{1}{N}\left[-\frac{R^2}{\omega_o^2}\left(\frac{2\,\tau}{\tau_{Flow}^2} - \frac{2\,cos\,\alpha}{\tau_{Flow}}\right)\right] * exp\left[-\frac{R^2}{{\omega_0}^2}\left(\frac{\tau^2}{{\tau_{Flow}}^2} + 1 - 2\frac{\tau}{\tau_{Flow}}\right) cos\,\alpha\right] \tag{90}$$

The preexponential portion can be set to zero

$$0 = \left[-\frac{R^2}{\omega_o^2}\left(\frac{2\,\tau}{\tau_{Flow}^2} - \frac{2\,cos\,\alpha}{\tau_{Flow}}\right)\right] \tag{91}$$

and solving for τ yields

$$\frac{2\,cos\,\alpha}{\tau_{Flow}} = \frac{2\,\tau}{\tau_{Flow}^2} \tag{92a}$$

$$\tau = \tau_{Flow}\,cos\,\alpha \tag{92b}$$

This indicates that the position of the peak at time τ has a maximum value τ_{Flow} and a cosine dependence on the angle between the spacing vector and the flow vector.

A.7 Dependence of Cross-correlation Peak Amplitude on Angle

Again beginning with the simplified flow cross-correlation function (equation 19) and solving for the maximum value of G_{cc} (at $\tau = \tau_{Flow}\,cos\,\alpha$)

$$G_{cc}(\tau) = \frac{1}{N} exp\left[-\frac{R^2}{{\omega_o}^2}\left(\frac{\tau_{Flow}\,cos\,\alpha}{{\tau_{Flow}}^2} + 1 - 2\frac{\tau_{Flow}\,cos\,\alpha}{\tau_{Flow}}\right) cos\,\alpha\right] \tag{93}$$

which reduces to

$$G_{cc}(\tau) = \frac{1}{N} exp\left[-\frac{R^2}{{\omega_o}^2}\left(cos^2\,\alpha + 1 - 2\,cos^2\,\alpha\right)\right] \tag{94}$$

Through the identity $sin^2\, x + cos^2\, x = 1$, this yields the final form of the cross-correlation amplitude function.

$$G_{cc}(\tau) = \frac{1}{N} exp\left[-\frac{R^2}{{\omega_o}^2}\left(sin^2\,\alpha\right)\right] \tag{95}$$

The extension of this to three dimensions has been previous given in equation 95.

REFERENCES

[1] D Pristinski, V Kozlovskaya, and SA Sukhishvili. Fluorescence correlation spectroscopy studies of diffusion of a weak polyelectrolyte in aqueous solutions. *Journal of Chemical Physics*, 122(1), January 2005.

[2] Howard Gest. The discovery of microorganisms by robert hooke and antoni van leeuwenhoek, fellows of the royal society. *Notes and Records of the Royal Society of London*, 58(2):187 – 201, 2004.

[3] J. A. Helmuth, C. J. Burckhardt, U. F. Greber, and I. F. Sbalzarini. Shape reconstruction of subcellular structures from live cell fluorescence microscopy images. *Journal of Structural Biology*, 167:1 – 10, 2009.

[4] S. Bolte and F. P. Cordieleres. A guided tour into subcellular colocalization analysis in light microscopy. *Journal of Microscopy*, 224:213 – 232, 2009.

[5] BNG Giepmans, SR Adams, MH Ellisman, and RY Tsien. Review - The fluorescent toolbox for assessing protein location and function. *Science*, 312(5771):217–224, April 2006.

[6] JA Conchello and JW Lichtman. Optical sectioning microscopy. *Nature Methods*, 2(12):920–931, December 2005.

[7] B Ballou, BC Lagerholm, LA Ernst, MP Bruchez, and AS Waggoner. Noninvasive imaging of quantum dots in mice. *Bioconjugate Chemistry*, 15(1):79–86, January 2004.

[8] J. R. Lakowicz. *Principles of Fluorescence Microscopy.* Kluwer Academic/Plenum Publishers, New York, 2nd edition edition, 1999.

[9] SM Nie and RN Zare. Optical detection of single molecules. *Annual Review of Biophysics and Biomolecular Structure*, 26:567–596, 1997.

[10] RM Dickson, AB Cubitt, RY Tsien, and WE Moerner. On/off blinking and switching behaviour of single molecules of green fluorescent protein. *Nature*, 388(6640):355–358, July 1997.

[11] WE Moerner and M Orrit. Illuminating single molecules in condensed matter. *Science*, 283(5408):1670+, March 1999.

[12] S Weiss. Fluorescence spectroscopy of single biomolecules. *Science*, 283(5408):1676–1683, March 1999.

[13] XS Xie and JK Trautman. Optical studies of single molecules at room temperature. *Annual Review of Physical Chemistry*, 49:441–480, 1998.

[14] M Dahan, S Levi, C Luccardini, P Rostaing, B Riveau, and A Triller. Diffusion dynamics of glycine receptors revealed by single-quantum dot tracking. *Science*, 302(5644):442–445, October 2003.

[15] J Lippincott-Schwartz, E Snapp, and A Kenworthy. Studying protein dynamics in living cells. *Nature Reviews: Molecular Cell Biology*, 2(6):444–456, June 2001.

[16] XW Zhuang, LE Bartley, HP Babcock, R Russell, TJ Ha, D Herschlag, and S Chu. A single-molecule study of RNA catalysis and folding. *Science*, 288(5473):2048+, June 2000.

[17] MJ Saxton and K Jacobson. Single-particle tracking: Applications to membrane dynamics. *Annual Review of Biophysics and Biomolecular Structure*, 26:373–399, 1997.

[18] JC Crocker and DG Grier. Methods of digital video microscopy for colloidal studies. *Journal of Colloid and Interface Science*, 179(1):298–310, April 1996.

[19] Comert Kural, Hwajin Kim, Sheyum Syed, Gohta Goshima, Vladimir I. Gelfand, and Paul R. Selvin. Kinesin and dynein move a peroxisome in vivo: A tug-of-war or coordinated movement? *Science*, 308(5727):1469 – 1472, 2005.

[20] Yasushi Sako, Shigeru Minoguchi, and Toshio Yanagida. Single-molecule imaging of egfr signalling on the surface of living cells. *Nature Cell Biology*, 2:168 – 172, 2000.

[21] Michael Brinkmeier, Klaus Drre, Jens Stephan, and Manfred Eigen. Two beam cross correlation: A method to characterize transport phenomena in micrometer-sized structures. *Analytical Chemistry*, 71(3):609–616, 1999.

[22] Petra S. Dittrich and Petra Schwille. Spatial two-photon fluorescence cross-correlation spectroscopy for controlling molecular transport in microfluidic structures. *Analytical Chemistry*, 74(17):4472–4479, 2002.

[23] Paul C. Brister, Kalyan K. Kuricheti, Volker Buschmann, and Kenneth D. Weston. Fluorescence correlation spectroscopy for flow rate imaging and monitoring - optimization, limitations and artifacts. *Lab on a Chip*, 5(7):785–791, 2005.

[24] Xiaotao Pan, Hanry Yu, Xianke Shi, Vladimir Korzh, and Thorsten Wohland. Characterization of flow direction in microchannels and zebrafish blood vessels by scanning fluorescence correlation spectroscopy. *Journal of Biomedical Optics*, 12(1), 2007.

[25] Michael Golsch, Hans Blom, Johan Holm, Toni Heino, and Rudolf Rigler. Hydrodynamic flow profiling in microchannel structures by single molecule fluorescence correlation spectroscopy. *Analytical Chemistry*, 72(14):3260–3265, 2000.

[26] Xiaotao Pan, Xianke Shi, Vladimir Korzh, Hanry Yu, and Thorsten Wohland. Line scan fluorescence correlation spectroscopy for three-dimensional microfluidic flow velocity measurements. *Journal of Biomedical Optics*, 14(2), 2009.

[27] Kalyan K. Kuricheti, Volker Buschmann, , and Kenneth D. Weston. Application of fluorescence correlation spectroscopy for velocity imaging in microfluidic devices. *Applied Spectroscopy*, 58(10):1180–1186, 2004.

[28] Ratnakar B. Mujumdar, Lauren A. Ernst, Swati R. Mujumdar, Christopher J. Lewis, and Alan S. Waggoner. Cyanine dye labeling reagents: Sulfoindocyanine succinimidyl esters. *Bioconjugate Chemistry*, 4(2):455 – 462, 1993.

[29] R. F. Kubin and A. N. Fletcher. Fluorescence quantum yields of some rhodamine dyes. *Journal of Luminescence*, 27:455 – 462, 1982.

[30] LA Peyser, AE Vinson, AP Bartko, and RM Dickson. Photoactivated fluorescence from individual silver nanoclusters. *Science*, 291(5501):103–106, January 2001.

[31] J Zheng, JT Petty, and RM Dickson. High quantum yield blue emission from water-soluble Au_8 nanodots. *Journal of the American Chemical Society*, 125(26):7780–7781, July 2003.

[32] M Bruchez, M Moronne, P Gin, S Weiss, and AP Alivisatos. Semiconductor nanocrystals as fluorescent biological labels. *Science*, 281(5385):2013–2016, September 1998.

[33] RY Tsien. The green fluorescent protein. *Annual Review of Biochemistry*, 67:509–544, 1998.

[34] H Qian and EL Elson. Analysis of Confocal Laser-Microscope Optics for 3-D Fluorescence Correlation Spectroscopy. *Applied Optics*, 30(10):1185–1195, April 1991.

[35] PM Goodwin, WP Ambrose, and RA Keller. Single-molecule detection in liquids by laser-induced fluorescence. *Accounts of Chemical Research*, 29(12):607–613, December 1996.

[36] U Haupts, S Maiti, P Schwille, and WW Webb. Dynamics of fluorescence fluctuations in green fluorescent protein observed by fluorescence correlation spectroscopy. *Proceedings of the National Academy of Sciences of the United States of America*, 95(23):13573–13578, November 1998.

[37] KT Shimizu, RG Neuhauser, CA Leatherdale, SA Empedocles, WK Woo, and MG Bawendi. Blinking statistics in single semiconductor nanocrystal quantum dots. *Physical Review B*, 63(20), May 2001.

[38] Lloyd M. Davis and Guoqing Shen. Accounting for triplet and saturation effects in FCS measurements. *Current Pharmaceutical Biotechnology*, 7(4):287–301, August 2006.

[39] R Zondervan, F Kulzer, SB Orlinskii, and M Orrit. Photoblinking of rhodamine 6G in poly(vinyl alcohol): Radical dark state formed through the triplet. *Journal of Physical Chemistry A*, 107(35):6770–6776, September 2003.

[40] WT Yip, DH Hu, J Yu, DA van den Bout, and PF Barbara. Classifying the photophysical dynamics of single- and multiple-chromophoric molecules by single molecule spectroscopy. *Journal of Physical Chemistry A*, 102(39):7564–7575, September 1998.

[41] FD Stefani, W Knoll, M Kreiter, X Zhong, and MY Han. Quantification of photoinduced and spontaneous quantum-dot luminescence blinking. *Physical Review B*, 72(12), September 2005.

[42] R Verberk, AM van Oijen, and M Orrit. Simple model for the power-law blinking of single semiconductor nanocrystals. *Physical Review B*, 66(23), December 2002.

[43] M Sugisaki, HW Ren, K Nishi, and Y Masumoto. Fluorescence intermittency in self-assembled InP quantum dots. *Physical Review Letters*, 86(21):4883–4886, May 2001.

[44] Christian Ringemann, Andreas Schoenle, Arnold Giske, Claas von Middendorff, Stefan W. Hell, and Christian Eggeling. Enhancing fluorescence brightness: Effect of reverse intersystem crossing studied by fluorescence fluctuation spectroscopy. *Chemphyschem*, 9(4):612–624, March 2008.

[45] T. Dertinger, R. Colyera, G. Iyer, S. Weiss, and J. Enderlein. Fast, background-free, 3D super-resolution optical fluctuation imaging (SOFI). *Proceedings of the National Academy of Sciences of the United States of America*, 106(52):2228722292, 2009.

[46] H Giloh and JW Sedat. Fluorescence Microscopy - Reduced Photobleaching of Rhodamine and Fluorescence Protein Conjugates by Normal-Propyl Gallate. *Science*, 217(4566):1252–1255, 1982.

[47] L Marcu, WS Grundfest, and JMI Maarek. Photobleaching of arterial fluorescent compounds: Characterization of elastin, collagen and cholesterol time-resolved spectra during prolonged ultraviolet irradiation. *Photochemistry and Photobiology*, 69(6):713–721, June 1999.

[48] L Galassi. Wavelength dependence of the time course of fluorescence enhancement and photobleaching during irradiation of ethidium bromide-stained nuclei. *European Journal of Histochemistry*, 44(4):419–432, 2000.

[49] Wang Lei, Gu Ying, Li Xiao-song, Liu Fan-guang, and Yu Chang-qing. Fluorescence Spectroscopy study on photobleaching properties of photosensitizers in photodynamic therapy. *Spectroscopy and Spectral Analysis*, 27(10):2073–2078, October 2007.

[50] N Miyoshi, T Arai, K Tokumaru, and M Fukuda. Photobleaching of fluorescent probe in microfluorometry and detection of active oxygen species. *Acta Histochemica et Cytochemica*, 30(2):189–191, 1997.

[51] J Hofkens, M Maus, T Gensch, T Vosch, M Cotlet, F Kohn, A Herrmann, K Mullen, and F De Schryver. Probing photophysical processes in individual multichromophoric dendrimers by single-molecule spectroscopy. *Journal of the American Chemical Society*, 122(38):9278–9288, September 2000.

[52] PS Dittrich and P Schwille. Photobleaching and stabilization of fluorophores used for single-molecule analysis with one- and two-photon excitation. *Applied Physics B - Lasers and Optics*, 73(8):829–837, December 2001.

[53] RE Thompson, DR Larson, and WW Webb. Precise nanometer localization analysis for individual fluorescent probes. *Biophysical Journal*, 82(5):2775–2783, May 2002.

[54] G Molema, G Mesander, BJ Kroesen, W Helfrich, DKF Meijer, and LFMH de Leij. Analysis of in vitro lymphocyte adhesion and transendothelial migration by fluorescent-beads-based flow cytometric cell counting. *Cytometry*, 32(1):37–43, May 1998.

[55] Manfred Eigen and Rudolph Rigler. Sorting single molecules - application to diagnostics and evolutionary biotechnology. *Proceedings of the National Academy of Sciences of the United States of America*, 91(13):5740–5747, 1994.

[56] Douglas Magde, Elliot L. Elson, and Watt W. Webb. Fluorescence correlation spectroscopy ii. an experimental realization. *Biopolymers*, 13(1):29–61, 1974.

[57] Elliot L. Elson and Douglas Magde. Fluorescence correlation spectroscopy i. conceptual basis and theory. *Biopolymers*, 13(1):1–27, 1974.

[58] Douglas Magde, Watt W. Webb, and Elliot L. Elson. Thermodynamic fluctuations in a reacting system - measurement by fluorescence correlation spectroscopy. *Physical Review Letters*, 29(11):705–708, 1972.

[59] Petra Schwille, Franz-Josef Meyer-Almes, and Rudolph Rigler. Dual-color fluorescence cross-correlation spectroscopy for multicomponent diffusional analysis in solution. *Biophysical Journal*, 72(4):1878–1886, 1997.

[60] You Korlann, Thomas Dertinger, Xavier Michalet, Shimon Weiss, and Joerg Enderlein. Measuring diffusion with polarization-modulation dual-focus fluorescence correlation spectroscopy. *Optics Express*, 16(19):14609–14616, September 2008.

[61] Michelle A. Digman, Paul W. Wiseman, Alan R. Horwitz, and Enrico Gratton. Detecting Protein Complexes in Living Cells from Laser Scanning Confocal Image Sequences by the Cross Correlation Raster Image Spectroscopy Method. *Biophysical Journal*, 96(2):707–716, January 2009.

[62] MA Digman, CM Brown, P Sengupta, PW Wiseman, AR Horwitz, and E Gratton. Measuring fast dynamics in solutions and cells with a laser scanning microscope. *Biophysical Journal*, 89(2):1317–1327, August 2005.

[63] QQ Ruan, MA Cheng, M Levi, E Gratton, and WW Mantulin. Spatial-temporal studies of membrane dynamics: Scanning fluorescence correlation spectroscopy (SFCS). *Biophysical Journal*, 87(2):1260–1267, August 2004.

[64] Markus Burkhardt and Petra Schwille. Electron multiplying ccd based detection for spatially resolved fluorescence correlation spectroscopy. *Optics Express*, 14(12):5013–5020, 2006.

[65] Balakrishnan Kannan, Jia Yi Har, Ping Liu, Ichiro Maruyama, Jeak Ling Ding, and Thorsten Wohland. Electron multiplying charge-coupled device camera based fluorescence correlation spectroscopy. *Analytical Chemistry*, 78:3444–3451, 2006.

[66] Daniel J. Needleman, Yangqing Xu, and Timothy J. Mitchison. Pin-Hole Array Correlation Imaging: Highly Parallel Fluorescence Correlation Spectroscopy. *Biophysical Journal*, 96(12):5050–5059, June 2009.

[67] Daniel R. Sisan, Richard Arevalo, Catherine Graves, Ryan McAllister, and Jeffrey S. Urbach. Spatially resolved fluorescence correlation spectroscopy using a spinning disk confocal microscope. *Biophysical Journal*, 91(11):4241–4252, 2006.

[68] JG White, WB Amos, and M Fordham. An Evaluation of Confocal Versus Conventional Imaging of Biological Structures by Fluorescence Light-Microscopy. *Journal of Cell Biology*, 105(1):41–48, July 1987.

[69] John M. Murray, Paul L. Appleton, Jason R. Swedlow, and Jennifer C. Waters. Evaluating performance in three-dimensional fluorescence microscopy. *Journal of Microscopy - Oxford*, 228(3):390–405, December 2007.

[70] E Wang, CM Babbey, and KW Dunn. Performance comparison between the high-speed Yokogawa spinning disc confocal system and single-point scanning confocal systems. *Journal of Microscopy - Oxford*, 218(Part 2):148–159, May 2005.

[71] PS Maddox, B Moree, JC Canman, and ED Salmon. Spinning disk confocal microscope system for rapid high-resolution, multimode, fluorescence speckle microscopy and green fluorescent protein imaging in living cells. In *Biophotonics, Pt A*, volume 360 of *Methods in Enzymology*, pages 597–617. 2003.

[72] GY Fan, H Fujisaki, A Miyawaki, RK Tsay, RY Tsien, and MH Ellisman. Video-rate scanning two-photon excitation fluorescence microscopy and ratio imaging with cameleons. *Biophysical Journal*, 76(5):2412–2420, May 1999.

[73] T Tanaami, S Otsuki, N Tomosada, Y Kosugi, M Shimizu, and H Ishida. High-speed 1-frame/ms scanning confocal microscope with a microlens and Nipkow disks. *Applied Optics*, 41(22):4704–4708, August 2002.

[74] A Nakano. Spinning-disk confocal microscopy - A cutting-edge tool for imaging of membrane traffic. *Cell Structure and Function*, 27(5):349–355, October 2002.

[75] MC Adams, WC Salmon, SL Gupton, CS Cohan, T Wittmann, N Prigozhina, and CM Waterman-Storer. A high-speed multispectral spinning-disk confocal microscope system for fluorescent speckle microscopy of living cells. *Methods*, 29(1):29–41, January 2003.

[76] J. G. Santiago, S. T. Wereley, C. D. Meinhart, D. J. Beebe, and R. J. Adrian. A particle image velocimetry system for microfluidics. *Experiments in Fluids*, 25(3):316–319, 1998.

[77] RJ Adrian. Particle-Imaging Techniques for Experimental Fluid-Mechanics. *Annual Review of Fluid Mechanics*, 23:261–304, 1991.

[78] CE Willert and M Gharib. Digital Particle Image Velocimetry. *Experiments in Fluids*, 10(4):181–193, 1991.

[79] J Westerweel. Fundamentals of digital particle image velocimetry. *Measurement Science & Technology*, 8(12):1379–1392, December 1997.

[80] A Melling. Tracer particles and seeding for particle image velocimetry. *Measurement Science & Technology*, 8(12):1406–1416, December 1997.

[81] EA Cowen and SG Monismith. A hybrid digital particle tracking velocimetry technique. *Experiments in Fluids*, 22(3):199–211, January 1997.

[82] HG Maas, A Gruen, and D Papantoniou. Particle Tracking Velocimetry in 3-Dimensional Flows 1. Photogrammetric Determination of Particle Coordinates. *Experiments in Fluids*, 15(2):133–146, July 1993.

[83] MGL Gustafsson. Extended resolution fluorescence microscopy. *Current Opinion in Structural Biology*, 9(5):627–634, October 1999.

[84] Lue Zhi-Jian, Lu Jing-Ze, Wu Ya-Qiong, and Chen Liang-Yi. Introduction to Theories of Several Super-resolution Fluorescence Microscopy Methods and Recent Advance in The Field. *Progress in Biochemistry and Biophysics*, 36(12):1626–1634, December 2009.

[85] Bo Huang, Mark Bates, and Xiaowei Zhuang. Super-Resolution Fluorescence Microscopy. *Annual Review of Biochemistry*, 78:993–1016, 2009.

[86] Stefan W. Hell. Far-field optical nanoscopy. *Science*, 316(5828):1153–1158, May 2007.

[87] Marta Fernandez-Suarez and Alice Y. Ting. Fluorescent probes for super-resolution imaging in living cells. *Nature Reviews Molecular Cell Biology*, 9(12):929–943, December 2008.

[88] E Betzig, JK Trautman, TD Harris, JS Weiner, and RL Kostelak. Breaking the Diffraction Barrier - Optical Microscopy on a Nanometric Scale. *Science*, 251(5000):1468–1470, March 1991.

[89] Barbel I. de Bakker, Andrea Bodnar, Erik M. H. P. van Dijk, Gyorgy Vamosi, Sandor Damjanovich, Thomas A. Waldmann, Niek F. van Hulst, Attila Jenei, and Maria F. Garcia-Parajo. Nanometer-scale organization of the alpha subunits of the receptors for IL2 and IL15 in human T lymphoma cells. *Journal of Cell Science*, 121(5):627–633, March 2008.

[90] F de Lange, A Cambi, R Huijbens, B de Bakker, W Rensen, M Garcia-Parajo, N van Hulst, and CG Figdor. Cell biology beyond the diffraction limit: near-field scanning optical microscopy. *Journal of Cell Science*, 114(23):4153–4160, December 2001.

[91] MGL Gustafsson, DA Agard, and JW Sedat. (IM)-M-5: 3D widefield light microscopy with better than 100 nm axial resolution. *Journal of Microscopy - Oxford*, 195(Part 1):10–16, July 1999.

[92] SW Hell, S Lindek, and EHK Stelzer. Enhancing the Axial Resolution in Far-Field Light-Microscopy - 2-Photon 4Pi Confocal Fluorescence Micrscopy. *Journal of Modern Optics*, 41(4):675–681, April 1994.

[93] S Hell and EHK Stelzer. Fundamental Improvement of Resolution with a 4Pi-Confocal Fluorescence Microscope Using 2-Photon Excitation. *Optics Communications*, 93(5-6):277–282, October 1992.

[94] B Bailey, DL Farkas, DL Taylor, and F Lanni. Enhancement of Axial Resolution in Fluorescence Microscopy by Standing-Wave Excitation. *Nature*, 366(6450):44–48, November 1993.

[95] B Bailey, F Lanni, DL Farkas, and DL Taylor. High-Resolution Direct 3-D Fluorescence Microscpy of Cells and Organelles by Standing-Wave Excitation-Based Optical Sectioning. *Biophysical Journal*, 66(2, Part 2):A275, February 1994.

[96] VC Abraham, V Krishnamurthi, B Bailey, DL Taylor, and F Lanni. The three-dimensional structure and dynamics of the actin cytoskeleton in lamellipodia using Standing Wave Fluorescence Microscopy. *Molecular Biology of the Cell*, 7(Suppl. S):2215, December 1996.

[97] VC Abraham, V Krishnamurthi, DL Taylor, and F Lanni. The actin-based nanomachine at the leading edge of migrating cells. *Biophysical Journal*, 77(3):1721–1732, September 1999.

[98] MGL Gustafsson. Surpassing the lateral resolution limit by a factor of two using structured illumination microscopy. *Journal of Microscopy - Oxford*, 198(Part 2):82–87, May 2000.

[99] Peter Kner, Bryant B. Chhun, Eric R. Griffis, Lukman Winoto, and Mats G. L. Gustafsson. Super-resolution video microscopy of live cells by structured illumination. *Nature Methods*, 6(5):339–U36, May 2009.

[100] Mats G. L. Gustafsson, Lin Shao, Peter M. Carlton, C. J. Rachel Wang, Inna N. Golubovskaya, W. Zacheus Cande, David A. Agard, and John W. Sedat. Three-dimensional resolution doubling in wide-field fluorescence microscopy by structured illumination. *Biophysical Journal*, 94(12):4957–4970, June 2008.

[101] Lothar Schermelleh, Peter M. Carlton, Sebastian Haase, Lin Shao, Lukman Winoto, Peter Kner, Brian Burke, M. Cristina Cardoso, David A. Agard, Mats G. L. Gustafsson, Heinrich Leonhardt, and John W. Sedat. Subdiffraction multicolor imaging of the nuclear periphery with 3D structured illumination microscopy. *Science*, 320(5881):1332–1336, June 2008.

[102] MGL Gustafsson. Nonlinear structured-illumination microscopy: Wide-field fluorescence imaging with theoretically unlimited resolution. *Proceedings of the National Academy of Sciences of the United States of America*, 102(37):13081–13086, September 2005.

[103] A Yildiz and PR Selvin. Fluorescence imaging with one nanometer accuracy: Application to molecular motors. *Accounts of Chemical Research*, 38(7):574–582, July 2005.

[104] XH Qu, D Wu, L Mets, and NF Scherer. Nanometer-localized multiple single-molecule fluorescence microscopy. *Proceedings of the National Academy of Sciences of the United States of America*, 101(31):11298–11303, August 2004.

[105] A Yildiz, JN Forkey, SA McKinney, T Ha, YE Goldman, and PR Selvin. Myosin V walks hand-over-hand: Single fluorophore imaging with 1.5-nm localization. *Science*, 300(5628):2061–2065, June 2003.

[106] MP Gordon, T Ha, and PR Selvin. Single-molecule high-resolution imaging with photobleaching. *Proceedings of the National Academy of Sciences of the United States of America*, 101(17):6462–6465, April 2004.

[107] LS Churchman, Z Okten, RS Rock, JF Dawson, and JA Spudich. Single molecule high-resolution colocalization of Cy3 and Cy5 attached to macromolecules measures intramolecular distances through time. *Proceedings of the National Academy of Sciences of the United States of America*, 102(5):1419–1423, February 2005.

[108] KA Lidke, B Rieger, TM Jovin, and R Heintzmann. Superresolution by localization of quantum dots using blinking statistics. *Optics Express*, 13(18):7052–7062, September 2005.

[109] Bo Huang, Wenqin Wang, Mark Bates, and Xiaowei Zhuang. Three-dimensional super-resolution imaging by stochastic optical reconstruction microscopy. *Science*, 319(5864):810–813, February 2008.

[110] Mark Bates, Bo Huang, Graham T. Dempsey, and Xiaowei Zhuang. Multicolor super-resolution imaging with photo-switchable fluorescent probes. *Science*, 317(5845):1749–1753, September 2007.

[111] P Drude. On the electron theory of metals. *Annalen der Physik*, 1(3):566–613, March 1900.

[112] U Kreibig and M Vollmer. *Optical Properties of Metal Clusters*. Springer, Berlin, 1995.

[113] R Kubo. Electronic Properties of Metallic Fine Particles 1. *Journal of the Physical Society of Japan*, 17(6):975–&, 1962.

[114] WD Knight, K Clemenger, WA de Heer, WA Saunders, MY Chou, and ML Cohen. Electronic Shell Structure and Abundances of Sodium Clusters. *Physical Review Letters*, 52(24):2141–2143, 1984.

[115] WA de Heer. The Physics of Simple Metal-Clusters - Experimental Aspects and Simple-Models. *Reviews of Modern Physics*, 65(3, Part 1):611–676, July 1993.

[116] Roy Louigi Johnston. *Atomic and Molecular Clusters*. CRC Press, New York, 2002.

[117] Helmut Haberland. *Clusters of Atoms and Molecules*. Springer-Verlag, New York, 1994.

[118] H Uchtmann, K Rademann, and F Hensel. Metal-Nonmetal Transition and Homogeneous Nucleation of Mercury Vapor. *Annalen der Physik*, 48(1-3):207–214, 1991.

[119] L Skala. Interpolation Formulas for Describing Size Dependence of Properties of Finite Systems and their use for Clusters and Biologically Important Molecules. *Theochem - Journal of Molecular Structure*, 73:103–109, March 1991.

[120] WA Saunders, K Clemenger, WA de Heer, and WD Knight. Photoionization and Shell Structure of Potassium Clusters. *Physical Review B*, 32(2):1366–1368, 1985.

[121] M Schmidt and H Haberland. Optical spectra and their moments for sodium clusters, Na_n^+, with $3 \leq n \leq 64$. *European Physical Journal D*, 6(1):109–118, April 1999.

[122] U Kreibig. Electronic Properties of Small Silver Particles - Optical Constants and their Temperature Dependence. *Journal of Physics F - Metal Physics*, 4(7):999–1014, 1974.

[123] U Kreibig and L Genzel. Optical Absorption of Small Metallic Particles. *Surface Science*, 156(JUN):678–700, 1985.

[124] GA Ozin and H Huber. Cryo-photo-clustering Techniques for Synthesizing very small, naked Silver clusters (Ag_N) of known size (where N = 2 - 5) - Moleculelar Metal Cluster Bulk Metal-Particle Interface. *Inorganic Chemistry*, 17(1):155–163, 1978.

[125] S. Fedrigo, W. Harbich, and J. Buttet. Optical response of ag_2, ag_3, au_2, and au_3 in argon matrices. *Journal of Chemical Physics*, 99:5712 – 5717, 1993.

[126] W Harbich, S Fedrigo, F Meyer, DM Lindsay, J Lignieres, JC Rivoal, and D Kreisle. Deposition of Mass Selected Silver Clusters in Rare-Gas Matrices. *Journal of Chemical Physics*, 93(12):8535–8543, December 1990.

[127] C Felix, C Sieber, W Harbich, J Buttet, I Rabin, W Schulze, and G Ertl. Ag-8 fluorescence in argon. *Physical Review Letters*, 86(14):2992–2995, April 2001.

[128] S. Lecoultre, A. Rydlo, C. Felix, and W. Harbich. Gold dimer in neon: an absorption and fluorescence study. *European Physical Journal D*, 52(1-3):187–190, April 2009.

[129] W Harbich, S Fedrigo, J Buttet, and DM Lindsay. Deposition of Mass Selected Gold Clusters in Solid Krypton. *Journal of Chemical Physics*, 96(11):8104–8108, June 1992.

[130] W Harbich, S Fedrigo, J Buttet, and DM Lindsay. Optical Spectroscopy on Size-Selected Gold Clusters Deposited in Rare-Gas Matrices. *Zeitschrift fur Physik D - Atoms Molecules and Clusters*, 19(1-4):157–159, 1991.

[131] M Brust, M Walker, D Bethell, DJ Schiffrin, and R Whyman. Synthesis of Thiol-Derivatized Gold Nanoparticles in a 2-phase Liquid-Liquid System. *Journal of the Chemical Society - Chemical Communications*, (7):801–802, April 1994.

[132] MC Daniel and D Astruc. Gold nanoparticles: Assembly, supramolecular chemistry, quantum-size-related properties, and applications toward biology, catalysis, and nanotechnology. *Chemical Reviews*, 104(1):293–346, January 2004.

[133] PV Kamat. Photophysical, photochemical and photocatalytic aspects of metal nanoparticles. *Journal of Physical Chemistry B*, 106(32):7729–7744, August 2002.

[134] CB Murray, CR Kagan, and MG Bawendi. Synthesis and characterization of monodisperse nanocrystals and close-packed nanocrystal assemblies. *Annual Review of Materials Science*, 30:545–610, 2000.

[135] LO Brown and JE Hutchison. Controlled growth of gold nanoparticles during ligand exchange. *Journal of the American Chemical Society*, 121(4):882–883, February 1999.

[136] MJ Hostetler, JE Wingate, CJ Zhong, JE Harris, RW Vachet, MR Clark, JD Londono, SJ Green, JJ Stokes, GD Wignall, GL Glish, MD Porter, ND Evans, and RW Murray. Alkanethiolate gold cluster molecules with core diameters from 1.5 to 5.2 nm: Core and monolayer properties as a function of core size. *Langmuir*, 14(1):17–30, January 1998.

[137] LO Brown and JE Hutchison. Convenient preparation of stable, narrow-dispersity, gold nanocrystals by ligand exchange reactions. *Journal of the American Chemical Society*, 119(50):12384–12385, December 1997.

[138] MM Alvarez, JT Khoury, TG Schaaff, MN Shafigullin, I Vezmar, and RL Whetten. Optical absorption spectra of nanocrystal gold molecules. *Journal of the Physical Chemistry B*, 101(19):3706–3712, May 1997.

[139] G Schmid, R Pfeil, R Boese, F Bandermann, S Meyer, GHM Calis, and WA van der Velden. Au $_{55}$ [P(C $_{6}$ H $_{5}$) $_{3}$] $_{12}$Cl $_{6}$ - A Gold Cluster of Exceptional Size. *Chemische Berichte-Recueil*, 114(11):3634–3642, 1981.

[140] D Lee, RL Donkers, GL Wang, AS Harper, and RW Murray. Electrochemistry and optical absorbance and luminescence of molecule-like Au-38 nanoparticles. *Journal of the American Chemical Society*, 126(19):6193–6199, May 2004.

[141] PA Bartlett, B Bauer, and SJ Singer. Synthesis of Water-Soluble Undecagold Cluster Compounds of Potential Importance in Electron-microscopic and other studies of Biological Systems. *Journal of the American Chemical Society*, 100(16):5085–5089, 1978.

[142] S Link, A Beeby, S FitzGerald, MA El-Sayed, TG Schaaff, and RL Whetten. Visible to infrared luminescence from a 28-atom gold cluster. *Journal of Physical Chemistry B*, 106(13):3410–3415, April 2002.

[143] RC Jin, S Egusa, and NF Scherer. Thermally-induced formation of atomic Au clusters and conversion into nanocubes. *Journal of the American Chemical Society*, 126(32):9900–9901, August 2004.

[144] K Clemenger. Ellipsoidal Shell Structure in Free-Electron Metal Clusters. *Physical Review B*, 32(2):1359–1362, 1985.

[145] Michael W. Heaven, Amala Dass, Peter S. White, Kennedy M. Holt, and Royce W. Murray. Crystal structure of the gold nanoparticle [N(C $_{8}$ H $_{17}$)$_{4}$)][Au $_{25}$ (SCH $_{2}$ CH $_{2}$ Ph) $_{18}$]. *Journal of the American Chemical Society*, 130(12):3754+, March 2008.

[146] A Henglein. Small-Particle Research - Physiochemical Properties of Extremely Small Colloidal Metal and Semiconductor Particles. *Chemical Reviews*, 89(8):1861–1873, December 1989.

[147] T Linnert, P Mulvaney, A Henglein, and H Weller. Long-Lived Nonmetalic Silver Clusters in Aqueous-Solution - Preparation and Photolysis. *Journal of the American Chemical Society*, 112(12):4657–4664, June 1990.

[148] E Janata, A Henglein, and BG Ershov. First Clusters of Ag^+ Ion Reduction in Aqueous-Solution. *Journal of Physical Chemistry*, 98(42):10888–10890, October 1994.

[149] JT Petty, J Zheng, NV Hud, and RM Dickson. DNA-templated Ag nanocluster formation. *Journal of the American Chemical Society*, 126(16):5207–5212, April 2004.

[150] Li Shang and Shaojun Dong. Facile preparation of water-soluble fluorescent silver nanoclusters using a polyelectrolyte template. *Chemical Communications*, (9):1088–1090, 2008.

[151] A Henglein, T Linnert, and P Mulvaney. Reduction of Ag^+ Polyanion Solution - Some Properties and Reactions of Long-lived Oligomeric Silver Clusters and Metallic Silver Particles. *Physical Chemistry Chemical Physics*, 94(12):1449–1457, December 1990.

[152] BG Ershov and A Henglein. Reduction of Ag+ on polyacrylate chains in aqueous solution. *Journal of Physical Chemistry B*, 102(52):10663–10666, December 1998.

[153] L Peyser-Capadona, J Zheng, JI Gonzalez, TH Lee, SA Patel, and RM Dickson. Nanoparticle-free single molecule anti-stokes Raman spectroscopy. *Physical Review Letters*, 94(5), February 2005.

[154] J Zheng and RM Dickson. Individual water-soluble dendrimer-encapsulated silver nanodot fluorescence. *Journal of the American Chemical Society*, 124(47):13982–13983, November 2002.

[155] Tom Vosch, Yasuko Antoku, Jung-Cheng Hsiang, Chris I. Richards, Jose I. Gonzalez, and Robert M. Dickson. Strongly emissive individual DNA-encapsulated Ag nanoclusters as single-molecule fluorophores. *Proceedings of the National Academy of Sciences of the United States of America*, 104(31):12616–12621, July 2007.

[156] Chris I. Richards, Sungmoon Choi, Jung-Cheng Hsiang, Yasuko Antoku, Tom Vosch, Angelo Bongiorno, Yih-Ling Tzeng, and Robert M. Dickson. Oligonucleotide-stabilized Ag nanocluster fluorophores. *Journal of the American Chemical Society*, 130(15):5038+, April 2008.

[157] Li Shang and Shaojun Dong. Silver nanocluster-based fluorescent sensors for sensitive detection of Cu(II). *Journal of Materials Chemistry*, 18(39):4636–4640, 2008.

[158] Junhua Yu, Sungmoon Choi, Chris I. Richards, Yasuko Antoku, and Robert M. Dickson. Live Cell Surface Labeling with Fluorescent Ag Nanocluster Conjugates. *Photochemistry and Photobiology*, 84(6):1435–1439, November 2008.

[159] Sandeep A. Patel, Chris I. Richards, Jung-Cheng Hsiang, and Robert M. Dickson. Water-soluble Ag nanoclusters exhibit strong two-photon-induced fluorescence. *Journal of the American Chemical Society*, 130(35):11602+, September 2008.

[160] Junhua Yu, Sungmoon Choi, and Robert M. Dickson. Shuttle-Based Fluorogenic Silver-Cluster Biolabels. *Angewandte Chemie-International Edition*, 48(2):318–320, 2009.

[161] Li Shang and Shaojun Dong. Sensitive detection of cysteine based on fluorescent silver clusters. *Biosensors & Bioelectronics*, 24(6):1569–1573, February 2009.

[162] Patrick R. O'Neill, Lourdes R. Velazquez, Donald G. Dunn, Elisabeth G. Gwinn, and D. Kuchnir Fygenson. Hairpins with Poly-C Loops Stabilize Four Types of Fluorescent Ag-n:DNA. *Journal of Physical Chemistry C*, 113(11):4229–4233, March 2009.

[163] Bidisha Sengupta, Caroline M. Ritchie, Jenna G. Buckman, Kenneth R. Johnsen, Peter M. Goodwin, and Jeffrey T. Petty. Base-Directed Formation of Fluorescent Silver Clusters. *Journal of Physical Chemistry C*, 112(48):18776–18782, December 2008.

[164] Sandeep A. Patel, Matteo Cozzuol, Joel M. Hales, Chris I. Richards, Matthew Sartin, Jung-Cheng Hsiang, Tom Vosch, Joseph W. Perry, and Robert M. Dickson. Electron Transfer-Induced Blinking in Ag Nanodot Fluorescence. *Journal of Physical Chemistry C*, 113(47):20264–20270, November 2009.

[165] Chris I. Richards, Jung-Cheng Hsiang, Dulal Senapati, Sandeep Patel, Junhua Yu, Tom Vosch, and Robert M. Dickson. Optically Modulated Fluorophores for Selective Fluorescence Signal Recovery. *Journal of the American Chemical Society*, 131(13):4619–4621, April 2009.

[166] GN Lewis and M Kasha. Phosphorescence and the triplet state. *Journal of the American Chemical Society*, 66:2100–2116, July 1944.

[167] C Eggeling, J Widengren, R Rigler, and CAM Seidel. Photobleaching of fluorescent dyes under conditions used for single-molecule detection: Evidence of two-step photolysis. *Analytical Chemistry*, 70(13):2651–2659, July 1998.

[168] J Widengren and CAM Seidel. Manipulation and characterization of photo-induced transient states of Merocyanine 540 by fluorescence correlation spectroscopy. *Physical Chemistry Chemical Physics*, 2(15):3435–3441, 2000.

[169] Y Kimura, JC Alfano, PK Walhout, and PF Barbara. Ultrafast Transient Absorption Spectroscopy of the Solvated Electron in Water. *Journal of Physical Chemistry*, 98(13):3450–3458, March 1994.

[170] RJ Sension, CM Phillips, AZ Szarka, WJ Romanow, AR McGhie, JP McCauley, AB Smith, and RM Hochstrasser. Transient Absorption Studies of C_{60} in Solution. *Journal of Physical Chemistry*, 95(16):6075–6078, August 1991.

[171] Y Kajii, T Kakagawa, S Suzuki, Y Achiba, K Obi, and K Shibuya. Transient absorption, lifetime, and relaxation of C_{60} in the Triplet State. *Chemical Physics Letters*, 181(2-3):100–104, June 1991.

[172] DB Geohegan and DN Mashburn. Characterization of Ground State Neutral and Ion-transport During Laser Ablation of Y_1Ba_2 $Cu_3O_7{}^{-X}$ Using Transient Optical Abosrption Spectroscopy. *Applied Physics Letters*, 55(22):2345–2347, November 1989.

[173] S Reindl and A Penzkofer. Higher excited-state triplet-singlet intersystem crossing of some organic dyes. *Chemical Physics*, 211(1-3):431–439, November 1996.

[174] RW Redmond, IE Kochevar, M Krieg, G Smith, and WG McGimpsey. Excited state relaxation in cyanine dyes: A remarkably efficient reverse intersystem crossing from upper triplet levels. *Journal of Physical Chemistry A*, 101(15):2773–2777, April 1997.

[175] I Ruckmann, A Zeug, R Herter, and B Roder. On the influence of higher excited states on the ISC quantum yield of octa-alpha-alkyloxy-substituted Zn-phthalocyanine molecules studied by nonlinear absorption. *Photochemistry and Photobiology*, 66(5):576–584, November 1997.

[176] T Sakata, YL Yan, and G Marriott. Optical switching of dipolar interactions on proteins. *Proceedings of the National Academy of Sciences of the United States of America*, 102(13):4759–4764, March 2005.

[177] Eric Betzig, George H. Patterson, Rachid Sougrat, O. Wolf Lindwasser, Scott Olenych, Juan S. Bonifacino, Michael W. Davidson, Jennifer Lippincott-Schwartz, and Harald F. Hess. Imaging intracellular fluorescent proteins at nanometer resolution. *Science*, 313(5793):1642–1645, September 2006.

[178] Gerard Marriott, Shu Mao, Tomoyo Sakata, Jing Ran, David K. Jackson, Chutima Petchprayoon, Timothy J. Gomez, Erica Warp, Orapim Tulyathan, Holly L. Aaron, Ehud Y. Isacoff, and Yuling Yan. Optical lock-in detection imaging microscopy for contrast-enhanced imaging in living cells. *Proceedings of the National Academy of Sciences of the United States of America*, 105(46):17789–17794, November 2008.

[179] Graham T. Dempsey, Mark Bates, Walter E. Kowtoniuk, David R. Liu, Roger Y. Tsien, and Xiaowei Zhuang. Photoswitching Mechanism of Cyanine Dyes. *Journal of the American Chemical Society*, 131(51):18192+, December 2009.

[180] Shu Mao, Richard K. P. Benninger, Yuling Yan, Chutima Petchprayoon, David Jackson, Christopher J. Easley, David W. Piston, and Gerard Marriott. Optical lock-in detection of FRET using synthetic and genetically encoded optical switches. *Biophysical Journal*, 94(11):4515–4524, June 2008.

[181] Samuel T. Hess, Thanu P. K. Girirajan, and Michael D. Mason. Nanoscale visualization of fluorescent protein distributions in cells by fluorescence photoactivation localization microscopy (FPALM). *Biophysical Journal*, (Suppl. S):419A, January 2007.

[182] Cristina Flors, Jun-ichi Hotta, Hiroshi Uji-i, Peter Dedecker, Ryoko Ando, Hideaki Mizuno, Atsushi Miyawaki, and Johan Hofkens. A stroboscopic approach for fast photoactivation-localization microscopy with Dronpa mutants. *Journal of the American Chemical Society*, 129(45):13970–13977, November 2007.

[183] Dehong Hu, Zhiyuan Tian, Wuwei Wu, Wei Wan, and Alexander D. Q. Li. Photoswitchable Nanoparticles Enable High-Resolution Cell Imaging: PULSAR Microscopy. *Journal of the American Chemical Society*, 130(46):15279+, November 2008.

[184] Chris I. Richards, Jung-Cheng Hsiang, and Robert M. Dickson. Synchronously Amplified Fluorescence Image Recovery (SAFIRe). *Journal of Physical Chemistry B*, 114(1):660–665, January 2010.

[185] W. Becker. *Advanced Time-Correlated Single Photon Counting Techniques*. Springer, Berlin, 1999.

[186] J. Cooper McDonald, David C. Duffy, Janelle R. Anderson, Daniel T. Chiu, Hongkai Wu, Olivier J. A. Schueller, and George M. Whitesides. Fabrication of microfluidic systems in poly(dimethylsiloxane). *Electrophoresis*, 21(1):27–40, 1999.

[187] H. A. Stone, A. D. Stroock, , and A. Ajdari. Engineering flows in small devices: Microfluidics toward a lab-on-a-chip. *Annual Review of Fluid Mechanics*, 36:381–411, 2004.

[188] Petra S. Dittrich and Andreas Manz. Lab-on-a-chip: microfluidics in drug discovery. *Nature Drug Discovery*, 5:210–218, 2006.

[189] Jan C. T. Eijkel and Albert van den Berg. Nanofluidics: what is it and what can we expect from it? *Microfluidics and Nanofluidics*, 1:249–267, 2005.

[190] Michael K. Cheezum, William F. Walker, , and William H. Guilford. Quantitative comparison of algorithms for tracking single fluorescent particles. *Biophysical Journal*, 81(4):2378–2388, 2001.

[191] Douglas Magde, Watt W. Webb, and Elliot L. Elson. Fluorescence correlation spectroscopy iii. uniform translation and laminar-flow. *Biopolymers*, 17(2):361–376, 1978.

[192] Elke Haustein and Petra Schwille. Fluorescence correlation spectroscopy: novel variations of an established technique. *Annual Reviews of Biophysics and Biomolecular Structure*, 36:151–169, 2007.

[193] Oleg Krichevsky and Gregoire Bonnet. Fluorescence correlation spectroscopy: the techniqe and its applications. *Reports on Progress in Physics*, 65:251–297, 2002.

[194] Anastasia Loman, Thomas Dertinger, Felix Koberling, and Jrg Enderlein. Comparison of optical saturation effects in conventional and dual-focus fluorescence correlation spectroscopy. *Chemical Physics Letters*, 459:18–21, 2008.

[195] Thomas Dertinger, Anastasia Loman, Benjamin Ewers, Claus B. Mller, Benedikt Krmer, and Jrg Enderlein. The optics and performance of dual-focus fluorescence correlation spectroscopy. *Optics Express*, 16(19):14353–14368, 2008.

[196] Lin Guo, Jia Yi Har, Jagadish Sankaran, Yimian Hong, Balakrishnan Kannan, and Thorsten Wohland. Molecular diffusion measurement in lipid bilayers over wide concentraton ranges: a comparative study. *Chemphyschem*, 9:721–728, 2008.

[197] Sara M. Hashmi, Michael Loewenberg, and Eric R. Dufresne. Spatially extended fcs for visualizing and quantifying high-speed multiphase flows in microchannels. *Optics Express*, 15(10):6528–6533, 2007.

[198] P Gonzaleztello, F Camacho, and G Blazquez. Density and Viscosity of Concentrated Aqueous-Solutions of Polyethylene-Glycol. *Journal of Chemical and Engineering Data*, 39(3):611–614, July 1994.

[199] Christopher I. Richards. *Dynamic Dark State Depletion: A Path to High Sensitivity Imaging*. PhD thesis, Georgia Institute of Technology, October 2009.

[200] BM Sutherland, M Randesi, K Wang, K Conlon, and GA Epling. Promoter-Specific Synthetic Photoendonuclease - Rose Bengal-Labeled T7 RNA-Polymerase. *Biochemistry*, 32(7):1788–1794, February 1993.

[201] Kimberly A. Conlon and Miguel Berrios. Light-induced proteolysis of myosin heavy chain by rose bengal-conjugated antibody complexes. *Journal of Photochemistry and Photobiology B: Biology*, 65(1):22 – 28, 2001.

[202] RS Molday, WJ Dreyer, A Rembaum, and SPS Yen. New Immunolatex Spheres - Visual Markers of Antigens on Lymphocytes for Scanning Electron-Microscopy. *Journal of Cell Biology*, 64(1):75–88, 1975.

[203] James M. Tsay, Michael Trzoss, Lixin Shi, Xiangxu Kong, Matthias Selke, Michael E. Jung, and Shimon Weiss. Singlet oxygen production by peptide-coated quantum dot-photosensitizer conjugates. *Journal of the American Chemical Society*, 129(21):6865–6871, May 2007.

[204] Ju Lu, Wei Min, Jose-Angel Conchello, Xiaoliang Sunney Xie, and Jeff W. Lichtman. Super-Resolution Laser Scanning Microscopy through Spatiotemporal Modulation. *Nano Letters*, 9(11):3883–3889, November 2009.

[205] Giuseppe Perinetti, Tobias Mueller, Alexander Spaar, Roman Polishchuk, Alberto Luini, and Alexander Egner. Correlation of 4Pi and Electron Microscopy to Study Transport Through Single Golgi Stacks in Living Cells with Super Resolution. *Traffic*, 10(4):379–391, April 2009.

[206] M Schrader, SW Hell, and HTM van der Voort. Three-dimensional super-resolution with a 4Pi-confocal microscope using image restoration. *Journal of Applied Physics*, 84(8):4033–4042, October 1998.

[207] Jie Zheng, Philip R. Nicovich, and Robert M. Dickson. Highly fluorescent noble-metal quantum dots. *Annual Review of Physical Chemistry*, 58:409–431, 2007.

[208] SM Nie and SR Emery. Probing single molecules and single nanoparticles by surface-enhanced Raman scattering. *Science*, 275(5303):1102–1106, February 1997.

[209] K Kneipp, Y Wang, H Kneipp, LT Perelman, I Itzkan, R Dasari, and MS Feld. Single molecule detection using surface-enhanced Raman scattering (SERS). *Physical Review Letters*, 78(9):1667–1670, March 1997.

[210] W Lesniak, AU Bielinska, K Sun, KW Janczak, XY Shi, JR Baker, and LP Balogh. Silver/dendrimer nanocomposites as biomarkers: Fabrication, characterization, in vitro toxicity, and intracellular detection. *Nano Letters*, 5(11):2123–2130, November 2005.

[211] JG Zhang, SQ Xu, and E Kumacheva. Photogeneration of fluorescent silver nanoclusters in polymer microgels. *Advanced Materials*, 17(19):2336+, October 2005.

[212] BG Ershov and A Henglein. Time-resolved investigation of early processes in the reduction of Ag+ on polyacrylate in aqueous solution. *Journal of Physical Chemistry B*, 102(52):10667–10671, December 1998.

[213] Zhong Shen, Hongwei Duan, and Holger Frey. Water-soluble fluorescent Ag nanoclusters obtained from multiarm star poly(acrylic acid) as "molecular hydrogel" templates. *Advanced Materials*, 19(3):349+, February 2007.

[214] Yuping Bao, Chang Zhong, Dung M. Vu, Jamshid P. Temirov, R. Brian Dyer, and Jennifer S. Martinez. Nanoparticle-free synthesis of fluorescent gold nanoclusters at physiological temperature. *Journal of Physical Chemsitry C*, 111(33):12194–12198, August 2007.

[215] Caroline M. Ritchie, Kenneth R. Johnsen, John R. Kiser, Yasuko Antoku, Robert M. Dickson, and Jeffrey T. Petty. Ag nanocluster formation using a cytosine oligonucleotide template. *Journal of Physical Chemsitry C*, 111(1):175–181, January 2007.

[216] Nan Ma, Chad J. Dooley, and Shana O. Kelley. RNA-templated semiconductor nanocrystals. *Journal of the American Chemical Society*, 128(39):12598–12599, October 2006.

[217] Junhua Yu, Sandeep A. Patel, and Robert M. Dickson. In vitro and intracellular production of peptide-encapsulated fluorescent silver nanoclusters. *Angewandte Chemie - International Edition*, 46(12):2028–2030, 2007.

[218] Li Liu, Hu-Zhi Zheng, Zhu-Jun Zhang, Yu-Ming Huang, Su-Ming Chen, and Yu-Fei Hu. Photoluminescence from water-soluble BSA-protected gold nanoparticles. *Spectrochimica Acta Part A - Molecular and Biomolecular Spectroscopy*, 69(3):701–705, March 2008.

[219] Bidisha Sengupta, Kerianne Springer, Jenna G. Buckman, Sandra P. Story, Oluwamuyiwa Henry Abe, Zahiyah W. Hasan, Zachary D. Prudowsky, Sheldon E. Rudisill, Natalya N. Degtyareva, and Jeffrey T. Petty. DNA Templates for Fluorescent Silver Clusters and I-Motif Folding. *Journal of Physical Chemistry C*, 113(45):1ovember, 2009.

[220] Jianping Xie, Yuangang Zheng, and Jackie Y. Ying. Protein-Directed Synthesis of Highly Fluorescent Gold Nanoclusters. *Journal of the American Chemical Society*, 131(3):888+, January 2009.

[221] PR Selvakannan, A Swami, D Srisathiyanarayanan, PS Shirude, R Pasricha, AB Mandale, and M Sastry. Synthesis of aqueous Au core-Ag shell nanoparticles using tyrosine as a pH-dependent reducing agent and assembling phase-transferred silver nanoparticles at the air-water interface. *Langmuir*, 20(18):7825–7836, August 2004.

[222] Jianping Xie, Jim Yang Lee, Daniel I. C. Wang, and Yen Peng Ting. Silver nanoplates: From biological to biomimetic synthesis. *ACS Nano*, 1(5):429–439, December 2007.

[223] VWW Yam and KKW Lo. Luminescent polynuclear d^{10} metal complexes. *Chemical Society Reviews*, 28(5):323–334, September 1999.

[224] Jie Zheng. *Fluorescent Noble Metal Nanoclusters*. PhD thesis, Georgia Institute of Technology, April 2005.

[225] A. D. Polyanin. *Handbook of Linear Partial Differential Equations for Engineers and Scientists*. Chapman and Hall / CRC, Boca Raton, 2001.

VITA

Philip R. (Rusty) Nicovich was born in Georgia, where he has continued to reside. Through a carefully calibrated combination of minimal effort and an excellent memory he graduated with honors from Parkview High School in 2001. Despite efforts to the contrary he then proceeded to Berry College in Mount Berry, Georgia, graduating *magna cum laude* with a B.S. in Chemistry in 2004. His academic carreer has proceeded to its current point following his joining the lab of Dr. Robert Dickson in the School of Chemistry and Biochemistry at the Georgia Institute of Technology.